Modelling and Demonstration of a Bifacial PV Curtain for Building Applications

S. Prabhudesai

Technische Universiteit Delft

TU Delft

Modelling and Demonstration of a Bifacial PV Curtain for Building Applications

by

Sukanya Prabhudesai

to obtain the degree of Master of Science

at the Delft University of Technology,

to be defended publicly on Tuesday August 27, 2019 at 1:30 PM.

Student number:	4735161	
Project duration:	December 1, 2018 – August 27, 2019	
Thesis committee:	Prof. dr. ir. O. Isabella,	TU Delft, supervisor
	Ir. J. C. Ortiz Lizcano,	TU Delft, daily supervisor
	Prof. dr. ir. M. Zeman,	TU Delft
	Dr. A. v. Dobbelstein,	TU Delft

Cover image courtesy : Store | Raamdecoratie

Keywords : Bifacial, BIPV, Photovoltaic, Curtain

This thesis is confidential and cannot be made public until December 31, 2019.

TU Delft

Summary

Global energy demand is on the rise. According to the International Energy Agency (IEA), in 2018, the building sector alone constituted 28 % of all energy-related CO_2 emissions. In an effort to reduce the carbon footprint of the building sector, the European Union has decreed that every new building from 2021 must be a nearly zero energy building where the low energy for such buildings must come from renewable sources. While this policy works well for new buildings, there needs to be also a solution developed for existing buildings or monumental buildings to be able to easily harness renewable energy, without the need for any major and costly renovation. The concept of a flexible cloth-based solar curtain as a plug and play solution for existing buildings has been explored in the current research, with particular focus on a bifacial (two-sided) design, to assess the significance of the indoor reflected daylight and artificial lights on the rear side power output of such a semi-transparent solar curtain.

An optical model representing a basic semi-transparent curtain comprising 70 % cloth of roughly 62 % transparency (based on availability), and 30 % of bifacial solar photovoltaic (PV) minimodules, is prepared as a base case. To validate the optical model, it is replicated on a smaller scale and tested using an identical experimental setup in a controlled environment using a solar simulator. Four cases are prepared for this: the curtain in an empty white-walled room, the curtain in the same room but with some furniture, the curtain in a shorter room with a white rear wall and the curtain in a shorter room with a black rear wall. An analysis of simulation and experimental results shows near likeness between the two with an error margin of 3.3 % for the base case to 10.6 % for the black rear wall case. Slight non uniformity of optical property inputs used in the simulation model and an overestimation of experimentally measured power due to a relatively lower irradiance seen by the reference cell are attributed to this difference.

After successful validation of the optical layout, the model is made to scale in simulations to form a PV curtain module of 538.44 Wp DC installed capacity. Using a north-east facing room as reference, an annual simulation is found to give a total DC energy yield of 188.45 kWh or 323 kWh/kWp with a bifacial gain of 8.64 %. 10 hours daily of artificial lighting inside the office is seen to increase the annual DC energy yield by 1.33 %. With an assumption that the curtain remains closed throughout sunshine hours (since it allows diffuse light to enter through its porous cloth), the power output of the curtain is seen to meet modest DC annual load profiles of 57.76 kWh in an office room for 95 % of the year with a 145 Wh lithium ion battery bank and of 48.86 kWh in a residential room for 92 % of the year, but with a much higher 290 Wh battery capacity, due to a greater mismatch between generation and demand. A sensitivity analysis for room orientation shows that for a more optimal azimuth of 202.5° (180° being south), the same curtain gives 82 % more annual DC yield compared to its current orientation, but at a much lower bifacial gain of 7.8 %. When analyzed for performance in different locations across the world, the curtain intuitively gives the best yield for locations in the southern hemisphere due to its orientation towards the north east. Bifacial gain is nevertheless, most significant for temperate locations where low average annual insolation makes the gain due to bifacial more significant. In cases where the room depth is reduced by half, yield is seen to improve by 2.1 %. Halving the amount of PV in the curtain, improves the bifacial gain by nearly 0.6 % but reduces the annual yield by 49 %. Conversely, doubling the PV in the curtain, results in a dip in bifacial gain by about 3.6 %, but an increase in annual DC power by 87 %. Although this is attractive, such a case must be treated with caution since the likelihood of leaving this curtain (that is now more opaque than semi-transparent) open during sunshine hours is higher. This can result in a lower power output than the base case as well as worse aesthetics.

Finally, it is concluded that a bifacial curtain is a beneficial for 'solarizing' existing buildings with minimal renovation. The bifacial aspect is best exploited for rooms with sub-optimal azimuths. Nevertheless, to make the most of the PV curtain, it is advised that it must be placed in shorter rooms with large windows and ideally facing the most optimal direction.

Acknowledgement

My goal of changing the status quo in society by actively contributing to the transition to clean energy, led me to pursue a Master in Sustainable Energy Technology. Completion of this thesis marks the culmination of my Master. Achieving this would not have been possible without the help and support of several people.

First and foremost, I would like to thank my supervisor Olindo Isabella for his constructive feedback, warm encouragement and for providing me opportunities to develop my skills outside the thesis. Big thanks to my first daily supervisor, Juan Camilo for his critical remarks on my work, support with experimentation and encouragement throughout the most stressful phases of the thesis. I am also very grateful to my second daily supervisor- Zoheir Haghighi for offering me this topic without which this thesis would not have existed. His feedback on my work in the early stages and connections to several people in TU Delft's Faculty of Architecture were most useful in my research. I am also thankful to Miro Zeman for his constant belief in me and Andy van Dobbelstein for agreeing to be part of my thesis committee.

I would also like to put on record my deep sense of gratitude to all the PhDs and Post-docs in the PVMD research group for their invaluable insights on my work. In particular, I would like to thank Rudi Santbergen, for entertaining my countless requests for brainstorming on matters related to ray-tracing that were difficult for me to comprehend in the early stages of my thesis. Also, special thanks to Andres Calcabrini for sharing enlightening pointers for the representation of my results and for all the technical discussions related to troubleshooting obstacles in my work. Maarten Verkou's sharing of his experience with raytracing also helped in giving me an early headstart. Besides this, Arno Smet's illuminating remarks on energy payback for niche products were instrumental in making me think critically of my work. I am also very grateful to Stefaan, for his practical suggestions on system design and spectrometer corrections, Martijn for expediting the repair of the laminator and Bart from DEMO in helping out with the experimental facade.

A number of people from Architecture also deserve special mention in this report. I can't thank Truus Hordijk enough for lending me her mock up of a scaled down room for use in my experimental validation which led to an immense saving of time. I would like to thank Michela Turrin and Pirouz Nourian for sharing tips about tools used for optical modelling and also Prethvi Raj and Premith Satish for their help with simulation software and architectural concepts respectively.

The last two months of my thesis involved many sleepless nights due to trouble in achieving accurate characterization of my cells. I am indebted to Simona Villa for getting me connected with the right people at the eleventh hour. Big thanks to Klaas Bakker for his last minute help with characterization of my mini modules at Solliance and Arthur Weeber for his quick analysis of my bifacial cells at ECN Petten. Also, I am grateful to Elias Garcia and Tijmen Slikker from Eternal Sun for their time and efforts in helping me with my measurements. Being a part of the Energy Club during my studies has been one of the most enriching experiences of my time here. I would sincerely like to thank the Delft Energy Initiative for their constant support, especially Eveline Zeegers for being like a mother to me, away from home.

Finally, surviving the thesis would have been incredibly tough without my ever-supportive friends here in Delft. I would like to thank my thesis office buddies- Anjali, Zidaan, Leo, Eliora, Nacho, and Emilio for lightening up the days with their liveliness. I would particularly like to thank Carlotta for always being there for me throughout the highs and lows of my thesis. Also, big thanks to my co-TAs Arturo and Yilong for always being available for brainstorming. I feel very privileged to have Mihir and Neel as my pillars of support here in Delft. Their help and encouragement throughout my time here has been unparalleled. Also thanks to Husain, Nilay and Yash for being part of this Indian family for me away from home. Finally I would like to thank my family abroad- Anushka and Sachin for their unrelenting positivity and encouragement throughout the most stressful phases of my thesis. No words are sufficient to express my gratitude to them as well as my parents who sponsored me and always believed in my capabilities. Your faith in me is my most prized asset.

S. Prabhudesai
Delft, August 2019

Contents

Abbreviations

IEA	International Energy Agency
EU	European Union
EPBD	Energy Performance of Buildings Directive
NZEB	Nearly Zero Energy Buildings
PV	Photovoltaics
BAPV	Building Applied Photovoltaics
BIPV	Building Integrated Photovoltaics
RF	Radio Frequency
MPPT	Maximum Power Point Tracking
IBC	Interdigitated Back Contact
LED	Light Emitting Diode
CdTe	Cadmium Telluride
CIGS	Copper Indium Gallium di-Selenide/Sulphide
GaAs	Gallium Arsenide
DSSC	Dye Sensitized Solar Cells
OPV	Organic Photovoltaics
c-Si	crystalline Silicon
a-Si	amorphous Silicon
DC	Direct Current
POA	Plane Of Array
DNI	Direct Normal Irradiance
AOI	Angle Of Incidence
DHI	Diffuse Horizontal Irradiance
3D	3 Dimensional
EEMCS	Electrical Engineering, Mathematics and Computer Science
TU Delft	Delft University of Technology
STC	Standard Test Conditions
DOD	Depth Of Discharge
Li ion	Lithium ion
LOLP	Loss Of Load Probability
AM	Air Mass
PERC	Passivated Emitter and Rear Contacted
EVA	Ethylene Vinyl Acetate

EL Electroluminescence

LASS Large Area Steady State Solar Simulator

PVGIS Photovoltaic Geographical Information System

EPBT Energy Pay Back Time

Nomenclature

Symbols

α	Absorption coefficient	[/m]
γ	Angle of incidence	[°]
λ	wavelength	[m]
θ_i	Angle of incidence	[°]
θ_r	Angle of reflection	[°]
θ_r	Angle of transmission	[°]
A	Absorptance	[−]
E_b	POA beam component of irradiance	[W/m^2]
E_d	POA sky-diffuse component of irradiance	[W/m^2]
E_g	POA ground reflected component of irradiance	[W/m^2]
E_{POA}	Total POA irradiance	[W/m^2]
I	Current	[A]
I_{MPP}	Maximum power point current	[A]
k	Extinction coefficient	[−]
n	Refractive index	[−]
R	Reflectance	[−]
r_p	P-polarized component the coefficient of reflection	[−]
r_s	S-polarized component the coefficient of reflection	[−]
T	Transmittance	[−]
t_p	P-polarized component the coefficient of transmission	[−]
t_s	S-polarized component the coefficient of transmission	[−]
V	Voltage	[V]
Wp	Wattpeak	[W]
x	Path length of ray	[m]

1 Introduction

1.1. Overview

Global energy demand is on the rise. Driven by a robust global economy and an increasing need for greater heating and cooling in several countries across the world, the global energy demand saw a steep growth of 2.3 % last year - its fastest pace in the past decade [1]. To achieve the Paris Agreement goals of restricting global temperature rise to 1.5°C above pre-industrial levels, a rapid shift to renewable sources is imperative, not only in power generation but also in buildings, industry and transport. In 2018, the building sector alone was responsible for 28 % of energy-related CO_2 emissions, two-thirds of which is attributed to electricity generation for use in buildings [2]. Increased access to electricity, rise in use of energy intensive appliances like air-conditioners and increase in floor area are considered responsible for these numbers. Figure 1.1 by International Energy Agency (IEA) shows the share of buildings in final electricity demand and the also the energy mix for electricity generation which is predominantly fossil-fuel based.

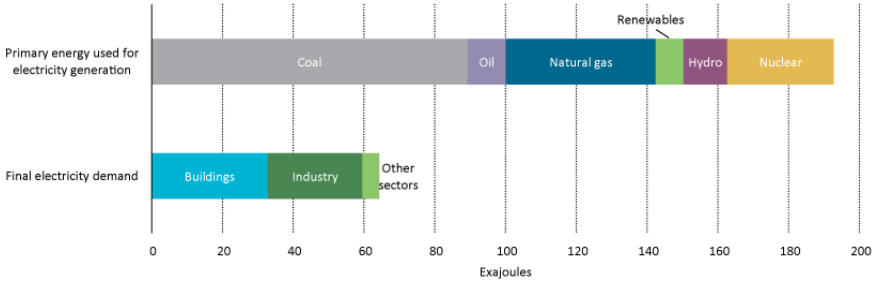

Figure 1.1: Energy Use for power generation and total electricity demand (by sector), 2010 [3]

To improve the energy performance of buildings, the European Union (EU) established a legislative framework comprising the Energy Performance of Buildings Directive (EPBD) and Energy Efficiency Directive. One of the key features of the EPBD is its Article 9, which states that all new buildings from 2021 must be Nearly Zero Energy Buildings (NZEB) and the low energy for such buildings must come mostly from renewable sources [4]. Ease of deployment in a distributed manner have made solar Photovoltaics (PV) attractive for accelerating to zero energy buildings by allowing for local energy generation. In particular, concepts such as Building Applied Photovoltaics (BAPV) and Building Integrated Photovoltaics (BIPV) have gained popularity due to their potential in transforming buildings from energy consumers into energy prosumers (producers and consumers).

In BAPV, the PV modules are externally attached to the rooftops or facades of buildings with the help of mounting equipment and moving rails [5]. The PV modules do not have any direct effect on the building structures and the way they function [6]. The tilt and azimuth of the modules may be optimized before

mounting, depending on local climate conditions, shade profiles and orientation of existing building or roof space. In BIPV, PV is integrated in the building structure, primarily in facades and roofs by way of BIPV products like PV-rooftiles, PV-facades or PV-glass. In such systems, the BIPV building structures replace the traditional building structures, thus affecting the way in which they function. BIPV is installed as per local climate conditions and architectural considerations [7]. Aesthetics are a major focus for BIPV in contrast to BAPV which serves more to optimize efficiency even if sometimes at the cost of aesthetics.

Despite the promise it offers in making a major contribution towards achieving nearly zero energy buildings, without compromising with its aesthetics, BIPV still remains a niche market amounting to just ~1 % of the global photovoltaics market [8]. Europe enjoys the highest share in this global BIPV market (42 %) due to attractive incentives in countries like Germany, Italy and France. In their research, Osseweijer et al. [8] developed a methodology to analyze key challenges for large-scale adoption of BIPV, especially in the Dutch context. Although political strategies and legal structures figure highest in their influence on BIPV implementation among the different European countries studied, other significant factors include influence of economic conditions such as ownership versus renting of houses, amount of solar radiation received in the area, and public awareness. Also, harmonization of building codes is seen as a major obstruction for BIPV development. BIPV is often not allowed on existing buildings as they are perceived not to comply with the necessary architectural features. Special sanctions are required to alter existing buildings (in the Netherlands, these are issued by the Dutch municipality's Design Review Committee). Therefore, today nearly two-thirds of BIPV implementations are on new buildings and only one-third are cases of renovation of existing buildings [9]. For quick decarbonising of the building sector, simply targeting new buildings is not going to be sufficient. Transforming existing buildings offers a much larger potential in significantly reducing the grid power consumed by these structures. To add to the complexity, Netherlands has nearly 62,000 Rijksmonuments (listed national heritage sites) of which half are residential homes. Any modification to these structures is subject to strict laws and regulations making it nearly impossible for these structures to opt for BIPV or even BAPV applications.

Another major challenge for BIPV is its cost. Economic feasibility of implementing BIPV, especially in case of existing buildings, is always under question since large initial investments need to be made by building owners to renovate their existing windows/ facades/ rooftiles to integrate them with PV technologies. Thus, as far as the market of existing buildings is concerned, there is an increasing need for a sort of cost-effective, plug and play product that helps in tapping significant amounts of free solar energy for electricity generation without the expenses of structural renovations. This thesis focuses on one such example in the form of solar curtains (sun-shade).

1.2. State-of-the-art solar curtains

The greatest advantage of using curtains as energy harvesting devices is that they can easily be incorporated in existing buildings without having to replace any window glass or facades or roof tiles. One of the earliest combinations of solar PV in sun shades was proposed by Hiraki [10] in 1990. In his patent, he described motorized roller shades along with a single solar strip-like panel in the lower portion, both enclosed within a double-glazed sliding glass door unit. A cylindrical Fresnel lens was used to concentrate the incoming solar radiation onto the PV cell that was used to power the motors of the shades. Shortly after, Corazzini [11] developed a model of solar powered venetian window blinds that involved attaching a head channel in the top jamb of the window frame with one slot facing outwards for mounting a small PV panel. The channel also housed an electric motor that automatically opens the venetian slats during the day and closes them at night, a control unit for this motor and a second slot facing the inside of the room with a lamp that lights up at night as a security provision, to give the illusion that the house is occupied, even if not (as seen in Figure 1.2. A further modification with a more optimum central location for the solar cell by mounting it on a flexible member stretched across the front of the venetian was suggested by Popat [12]. Liu [13] sophisticated the system of solar cell coupled with sunshades by adding a Radio Frequency (RF) control unit to enable remote operation of the blind's functionalities. A system of press switches was used to make the setup appear wireless. In 2007, Reid [14] proposed multi-panel vertical blinds to be used at any unobstructed internal to external recess and suggested rotating this plurality of solar panel slats for optimum power and visual conditioning, depending on application. Building up on this, in 2014, Moslehi [15] presented the design having Maximum Power Point Tracking (MPPT) optimizer components on each slat connected in series and

also solar cells mounted on at least two sides of the slats to capture light from external as well as internal light sources, as seen in Figure 1.3.

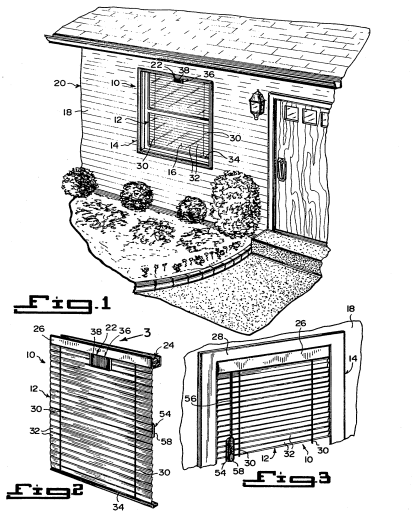

Figure 1.2: Basic solar powered venetian [11]

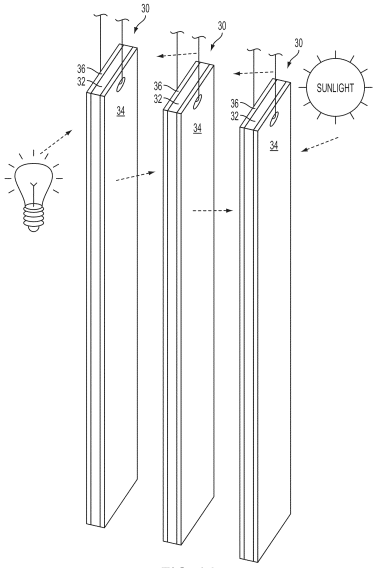

Figure 1.3: Double sided solar vertical blinds [15]

Setting an example for solar photovoltaics in blind systems, Technische Universität Darmstadt received much appreciation for their real scale demonstrator of the concept in the Solar Decathlon at USA in 2007. This can be seen in Figure 1.4. The first few companies to commercialize this space include San Francisco based Solar Gaps and Istanbul based Yalcin Renewable Energy Systems (now called Solar Curtain). While Solar Gaps products fall in the category of venetian blinds as seen in Figure 1.5, the Solar Curtain product belongs to the roman shades domain in Figure 1.6. Both use crystalline silicon Interdigitated Back Contact (IBC) solar cells with Solar Gaps using cut IBCs.

Figure 1.4: PV integrated blinds by Technische Universität Darmstadt at Solar Decathlon 2007 in USA [3]

Figure 1.5: Solar Gaps venetian blinds [16]

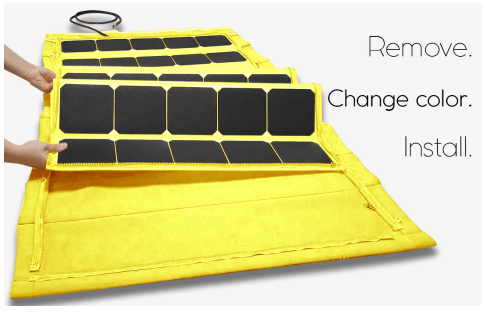

Figure 1.6: Solar Curtain roman shades [17]

While the solar-integrated blinds market has been extensively explored in the last two decades, the traditional cloth based curtain market has seen fewer instances of solar-integration. Independent attempts at flexible solar textiles were made by the *Inside Outside* design team at Textiel Labs [18] in the Netherlands, who partnered with the company Solar Fiber to come up with the design presented in Figure 1.7. Solar Fiber uses a type of polymer based photovoltaic technology which can be knitted along with the regular cloth. The product is now a part of the Textiel Museum's collection although data on its performance is unavailable. Another example of a knit solar curtain was shown by Taieb [19] who developed a ecodesign-centred prototype of an illuminating flexible solar curtain, using linen printed with dye sensitized solar cells to ensure minimum usage of water and material and low power LEDs for the illumination. A completely new design of Suntiles solar curtain, in collaboration with Astrid Krogh Design, using polymer solar cells to create a hanging power-producing sun-shading structure, was exhibited as seen in Figure 1.8 at the Danish Design Center in Copenhagen in May 2009 as cited in [20].

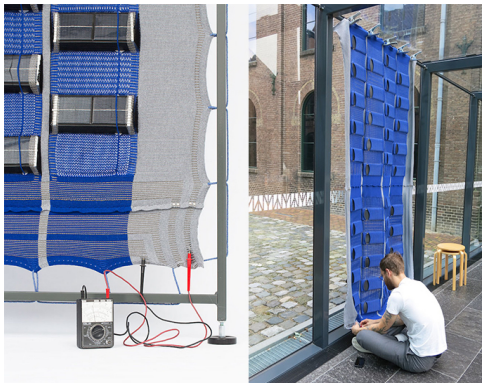

Figure 1.7: Solar curtain developed by Inside Outside design team at Textiel Lab [18]

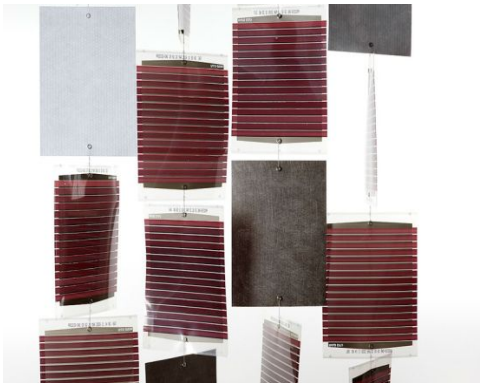

Figure 1.8: 'Suntiles' hanging sun-shade structure by Astrid Krogh [21]

Another demonstrator was attempted by Professor of the Practice at MIT's Department of Architecture and Principal in the *IBA SoftHouse* Design Team at KVA Matx, Sheila Kennedy. The initial idea was to use organic flexible solar photovoltaics to transform traditional curtains to translucent flexible energy harvesters. However it is seen that the final design instead comprised flexible facade elements using solar photovoltaics nano materials supplemented by a number of indoor curtains having Light Emitting Diode (LED) lamps for visual appeal as can be seen in Figure 1.9 and 1.10.

Figure 1.9: SoftHouse by Kennedy and Violich Architecture (KVA Matx), Hamburg [22]

Figure 1.10: Indoor curtains with integrated LEDs at the SoftHouse [22]

As is seen from the examples above, several options have been explored in the domain of solar integrated blinds and shades. Cloth based solar curtains remain relatively unexplored. The few cases of demonstrators attempted so far have unfortunately not seen commercialization. This could be linked to aesthetics but could also be linked to the power output of the specific solar technology employed in the various options shown. Nevertheless, it is clear that when it comes to buying sun-shading for homes, the first thought in homeowners' minds is curtains. Interior designers are also said to prefer curtains since the variety of colors

and materials available allow curtains to suit a wide range of interiors [23]. Thus, this thesis is targeted at developing technologically-optimized, cloth-based, solar curtains.

1.3. Suitable photovoltaic technologies

The recently published 54th version of solar cell efficiency tables [24] listed highest one-sun illumination solar cell and module efficiencies for the different types of solar photovoltaic technologies existing today. Though all the types of PV technologies listed may not be suitable for integration with flexible cloth curtains, these technologies are used as reference for the following subsections. The concept of PV technology generation was introduced by professor Martin Green (co-author of the bi-annual solar efficiency tables mentioned above) of University of New South Wales [25]. These are depicted in Figure 1.11. The following subsections explain each briefly and concludes with the choice of technology most suitable for this case.

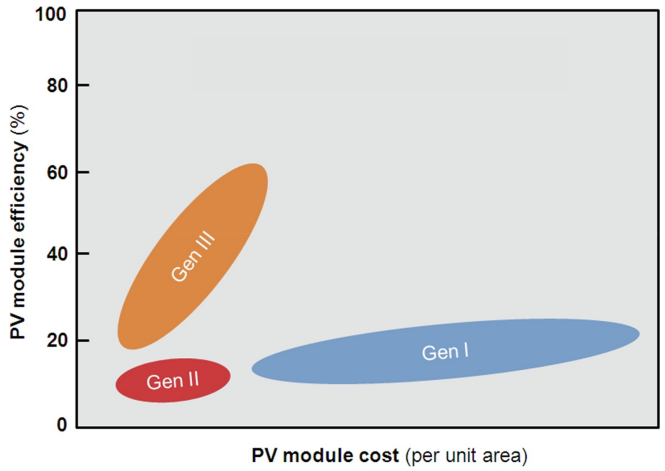

Figure 1.11: PV technology generations [26]

1.3.1. First generation PV

First generation PV refers to wafer-based technologies, generally crystalline silicon. At the cell level, Kaneka holds the record for highest efficiency with their n-type rear IBC crystalline silicon cell, of 26.7 ± 0.5 %. In multi-crystalline solar cells, efficiencies as high as 22.3 ± 0.4 % have been reported by Fraunhofer ISE [27]. It must be noted that commercial module efficiencies are lower than lab-scale efficiencies mentioned above. Highest crystalline silicon module efficiency achieved so far, again by Kaneka, is 24.4 ± 0.5 % for its 108 cell module. Nearly all the blinds mentioned in section 1.2 made use of crystalline silicon PV technologies. Long life, relatively high efficiency and drop in prices due to mass manufacturing in countries like China, have been the major drivers for this technology selection. As regards integration with cloth, crystalline silicon does not emerge a popular choice, flexibility being the main roadblock.

1.3.2. Second generation PV

Conventional thin film PV such as Cadmium Telluride (CdTe), Copper Indium Gallium di-Selenide/Sulphide (CIGS) and amorphous or microcystalline silicon are referred to as second generation PV technologies. Highest cell efficiency measured for CdTe is 21.0 ± 0.4 % [28], for CIGS 23.35 ± 0.5 % [29] and 10.2 ± 0.3 % for amorphous silicon [30]. Although initially thought to be cheaper than first generation as is seen from Figure 1.11, and expected over time to replace first generation technologies, in 2017, the market share of all thin film technologies amounted to only 5 % of the total annual production. The strong position of wafer based technologies have made it increasingly difficult for thin-film to compete in the mainstream market that is driven primarily by cost. Despite their lower cost of material usage and better thermal performance compared to first generation PV, economies of scale and low overall commercial efficiencies hinder their large scale deployment. Currently a number of companies are exploring the utility of thin-film technologies in specialized domains such as BIPV (roof-tiles and curved facades) and sails of boats. For use in a curtain, it is essential to

observe the performance of thin-films in indoor and outdoor environments. Gemmer [31] studied that CIGS was only competitive with crystalline Silicon (c-Si) in the outdoor environment since it suffered low-light deterioration of efficiency in indoor conditions. In indoor, low-light conditions, amorphous Silicon (a-Si) was most suitable. CdTe has not been much explored in integrated applications. Since records do not show much on thin-film mini-modules, the scope of customizing them for a curtain is still unknown.

1.3.3. Third generation PV

Third generation PV is used to describe technologies that have the potential of overcoming the Shockley-Queisser efficiency limit lying between 31 - 41 % for single bandgap solar cells (like first and second generation) [32]. Common third generation PV include multi-layer tandem cells using the high efficiency III-V technologies like Gallium Arsenide (GaAs) or amorphous silicon, Dye Sensitized Solar Cells (DSSC), Organic Photovoltaics (OPV) and quantum dots. Even as single junction, GaAs thin films have touched high efficiencies of 29.1 ± 0.6 % [33]. Multi-junction highest efficiencies recorded are as high as 38.8 ± 1.2 % for II-V 5 junction tandem cell [34]. Despite low cell efficiencies for most other third generation technologies for nearly a decade including a maximum achieved cell efficiency of 11.9 ± 0.4 % for DSSC, very recent results published show remarkable improvements in performance of some other third generation thin film cells such as 24.2 ± 0.8 % for Perovskites [35] and 16.4 ± 0.2 % for organic thin films [36] (results treated with some skepticism since cell areas for measurement were too small to declare a new record efficiency [24]).

Most of the options explored in cloth based solar curtain demonstrators in section 1.2 use organic PV or dye printing PV technologies. Although attractive due to their ease of integration by printing, flexibility and low impact on environment, most of these third generation technologies suffer heavily from moisture and temperature induced performance degradation, shortening their effective lifetime. With highest recorded lab-scale module efficiency for OPV being close to 8.7 % [37], commercially available flexible OPV such as those provided by InfinityPV (refer to Figure 1.12) provide a commercial maximum efficiency of only 4 %. The bankruptcy of one of the biggest early players in OPV, Konarka, show that the technology is still far from maturity. Figure 1.13 shows an example of dye based solar cell printed on fabric achieved by a team comprising assistant professor at University of Massachusetts-Amherst, Trisha Andrew and textile designer Marianne Fairbanks. Despite superior aesthetics, the low efficiency and stability is believed to be the reason why this technology is not commercialized yet. Most other third generation PV technologies too are still in a niche phase of research and not ready for commercialization but offer great promise in the near future.

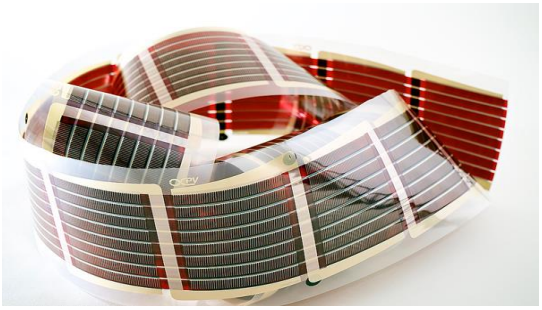

Figure 1.12: InfinityPV foil using OPV technology [38]

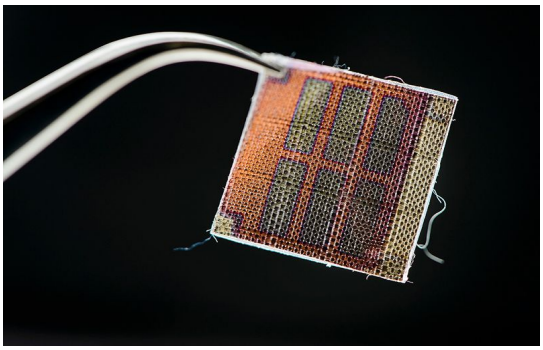

Figure 1.13: Textile coated in conductive polymer showing six solar cells (Photo by Jeff Miller/UW-Madison) [39]

1.3.4. Conclusion

As of today, third generation technologies rank highest in terms of potential efficiency. In case of III-V tandem cells, these figures are already achieved. However, GaAs, most commonly used in ultra-high efficiency tandem cells, is prohibitively expensive. This is because Gallium is a rare material (rarer than gold) and produced as a by-product during smelting of other metals. Arsenic, although abundant, is highly toxic. This makes GaAs PV expensive and difficult to manufacture, making it more suitable for niche markets like space applications and not the best choice for a household curtain. Organic PV and dye-based solar are attractive options in

terms of aesthetics as seen in subsection 1.3.3 but still quite futuristic due to their low scales of commercial efficiency and thermal instability. Even with second generation technologies, several flexible options exist that might come across as suitable for a PV curtain. However, these too suffer from an in-general, lower operational life compared to crystalline silicon, low commercial efficiency (a-Si), low light degradation (CIGS) or toxicity (CdTe) and as of today, seem to be not mature enough for customization and an economically feasible integration in a PV curtain. Lastly, with crystalline silicon dominating the PV market today, it is interesting to assess the possibility of using this technology in a flexible cloth curtain. Wafer-based c-Si PV is most popular today due to its high commercial efficiency, long lifetime, cost-effectiveness and reliability. Additionally, the growing popularity of bifacial technologies, mainly in the domain of c-Si PV, is another factor that makes this technology all the more interesting for a solar curtain. This is because, it provides the opportunity to explore how the performance of the solar curtain would be affected by indoor reflected daylight and artificial lights in addition to outdoor solar light when using state-of-the-art bifacial crystalline silicon PV technologies. Thus this thesis will focus on crystalline silicon as the preferred technology for designing a technologically optimized PV curtain. A novel method of foil-foil encapsulation that imparts a limited degree of flexibility for c-Si wafer cells that may help in integration with flexible cloth, will be demonstrated in further chapters.

1.4. Aim and scope of thesis

In view of the conclusions drawn from sections 1.2 and 1.3, it is clear that this thesis will concentrate on developing a cloth-based PV curtain with a special focus on the possibility of introducing bifacial aspects in the said curtain. The aim of this thesis can be summarized as: *'To model and fabricate a crystalline silicon, cloth-based, bifacial PV curtain for use in buildings and homes, and assess the impact of the bifaciality on the annual power output of such a curtain'*

1.5. Tasks and Objectives

To achieve the goals of this thesis, the following set of tasks and objectives have been laid down:

1. To prepare a three-dimensional model of the proposed PV curtain for a target room and model a ray-tracing simulation to assess annual system performance.
2. To fabricate the bifacial c-Si PV curtain and validate the simulation model with an identical experimental set-up.
3. To simulate the PV curtain in a real room and assess the sensitivity of the said PV curtain to location, room orientation, room depth and percentage of PV integration.
4. To perform a preliminary estimate of the loads that could be potentially satisfied by power from the curtain and design a basic balance-of-system for commercial and residential scenarios.

1.6. Report Outline

The report starts with a brief overview of solar energy in the urban landscape, elaborating on concepts of BIPV and BAPV and highlights the dearth of economically feasible options in BIPV that work for existing buildings without necessitating structural changes or renovation. The idea of 'solar curtains' is proposed as an option to overcome these hurdles. State-of-the-art solar curtains and blinds are consequently explored and finally the suitability of various PV technologies for these options is discussed.

Chapter 2 discusses the methodology employed in modelling the ray-tracing simulation of the PV curtain and the MATLAB post-processing applied to these results to obtain annual energy yield. It also touches upon the system sizing approaches employed in later chapters.

Chapter 3 describes the set-up created in the simulation model as well as in reality, for validation of simulation results.

Chapter 4 explains the full scale PV curtain model for the target room with the typical balance of system.

Various different sensitivities of the model are discussed and a very basic life cycle assessment is conducted.

Chapter 5 lists the key findings of this report and discusses the prospects of future work to enhance research in this topic.

2

System Modelling

Predicting the annual yield of a PV system is very critical in deciding its feasibility. In case of a BIPV system, annual yield not only helps in understanding the kind of loads supplied by the product but also in justifying the higher initial cost of the BIPV product in comparison to the traditional non-integrated product. For simplicity, this thesis will assume the PV curtain to only supply Direct Current (DC) loads, thus negating the need for any grid connection inverters. Figure 2.1 shows the schematic of the PV system proposed for the PV curtain. This chapter will elaborate on the methodology employed in each of the individual models- namely the irradiance model (section 2.1) and the electrical model (section 2.2) that combine together to form the complete PV system design as seen in the figure.

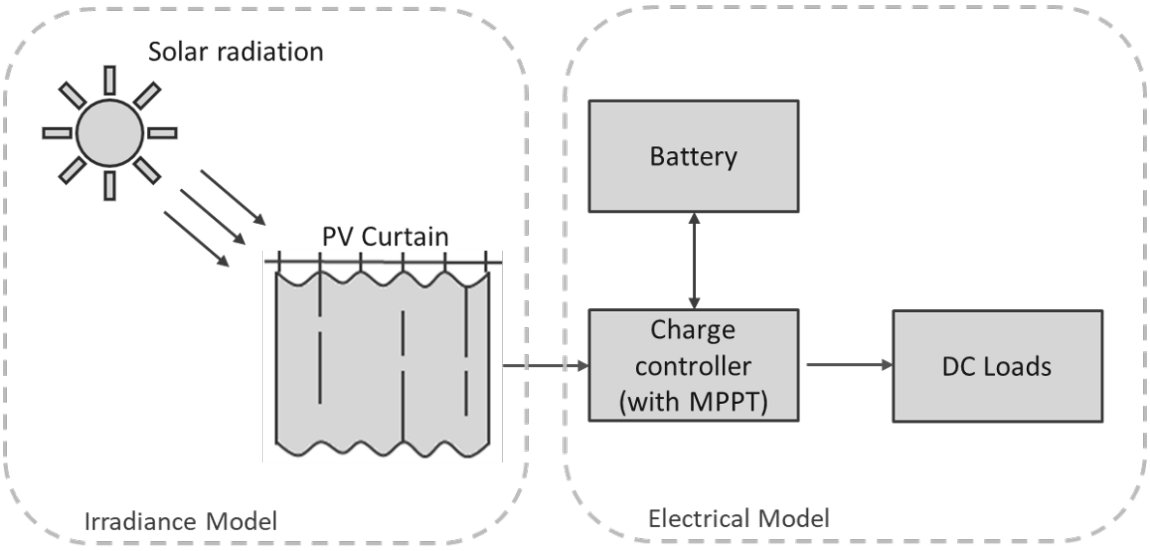

Figure 2.1: Stand-alone photovoltaic system design for PV curtain

2.1. Irradiance modelling

Irradiance is the radiant power incident per unit area, expressed in $W\,m^{-2}$. For modelling the performance of the PV system, it is crucial to calculate the irradiance incident on the Plane Of Array (POA) of the PV system as a function of time, since it is most directly related to the power output of the PV system. The POA irradiance is dependent on several factors such as the sun position, array orientation, irradiance components (direct and diffuse), ground surface reflectivity (albedo) and shading (near and far obstructions) [40].

Mathematically, POA irradiance E_{POA} is given by Equation 2.1 [40]:

$$E_{POA} = E_b + E_g + E_d \tag{2.1}$$

where E_b indicates the POA beam component, E_g indicates the POA ground reflected component and E_d is the POA sky-diffuse component. These can be visualised better in Figure 2.2
Since the thesis focuses on curtains inside buildings or houses, the effect of the ground-reflected irradiance component on the PV system performance is assumed negligible. Additionally, for the sake of simplicity, the effect of shade is not considered in this initial estimation of PV system performance. The POA beam component and POA sky-diffuse components are elaborated below:

POA beam component

POA beam component of irradiance is obtained from the Direct Normal Irradiance (DNI) using the following equation:

$$E_b = DNI \times cos(\gamma) \tag{2.2}$$

where γ is the angle between the PV array surface normal and the direction of the incident sunlight, or in other words, Angle Of Incidence (AOI). γ is dependent on altitude and azimuth of the sun as well as the tilt and azimuth of the PV surfaces.

POA sky-diffuse component

POA sky-diffuse component of irradiance is obtained from the Diffuse Horizontal Irradiance (DHI) and represents all irradiance from the sky dome incident on the PV surface, except the direct component of irradiance. Several models exist for converting the DHI, measured in the horizontal plane, into the corresponding POA sky-diffuse component. The Perez model is one of the most popular models used for diffuse component estimations. Other models can be found in [41].

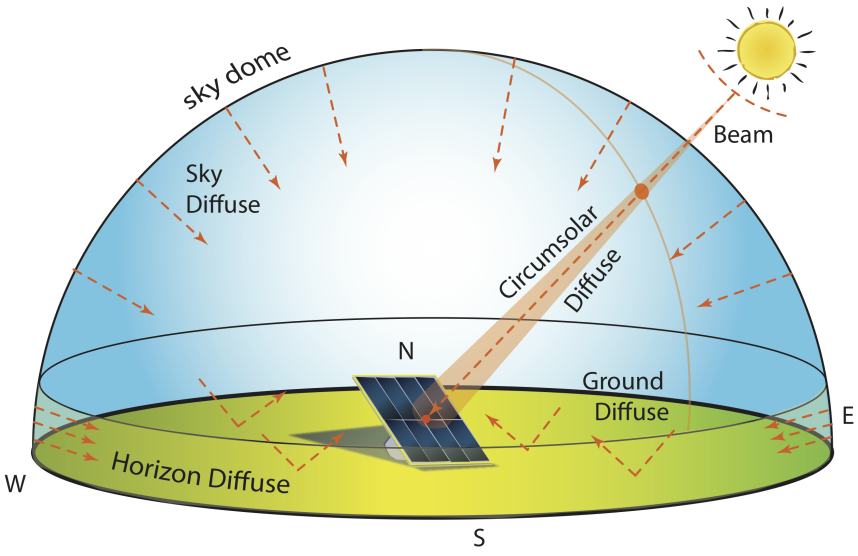

Figure 2.2: Various components of irradiance in a clear sky [42]

The method of determining POA irradiance described in this section is applied in several commercial software packages like PVsyst and Helioscope that were developed to assist in the design of technically and commercially optimized PV systems. Although the calculations can be applied quite easily for standard geometries of PV module arrays mounted on surfaces like rooftops or sloping grounds at a specific tilt angle and azimuth, it is not so straightforward for non-standard BIPV products. As is intuitive, the tilt and azimuth of these products cannot be specified in numbers and need complex geometries to be input which complicates

POA irradiance calculations. In addition, for a bifacial curved PV curtain, the effect of indoor daylight due to optical reflections from indoor surrounding surfaces and the effect of artificial lights is crucial, but currently not provided by commercial software packages. A possible alternate approach is found in ray-tracing, a technique popularly employed in daylighting simulations by architects and building engineers. Ray tracing is a technique used to study the optical performance of a system by determining the path of the rays as they travel through different media of varying refractive indices and absorption characteristics. It is primarily of two types: one that traces the ray in the conventional manner, starting from the light source and up to the target object and a second method, which traces the rays backwards, starting from the target object and up to the light source. The former is called forward ray tracing and the latter, backward ray tracing and can be understood from Figure 2.3. A software tool commonly used by architects for energy modelling using ray-tracing is Radiance. Developed in Lawrence Berkeley Laboratory, Radiance is a radiosity-based lighting simulation program that uses backward ray tracing process for simulation. However, according to Radiance documentation [43], despite attempts to adequately account for all significant sources of illumination, a few cases such as reflection of intense light from curved geometries are yet not adequately covered by the capabilities offered by backward ray tracing in Radiance. In such cases, it is recommended to use a forward ray trace approach as it is generally much more accurate although often computationally heavier and inefficient than backward ray trace models [44].

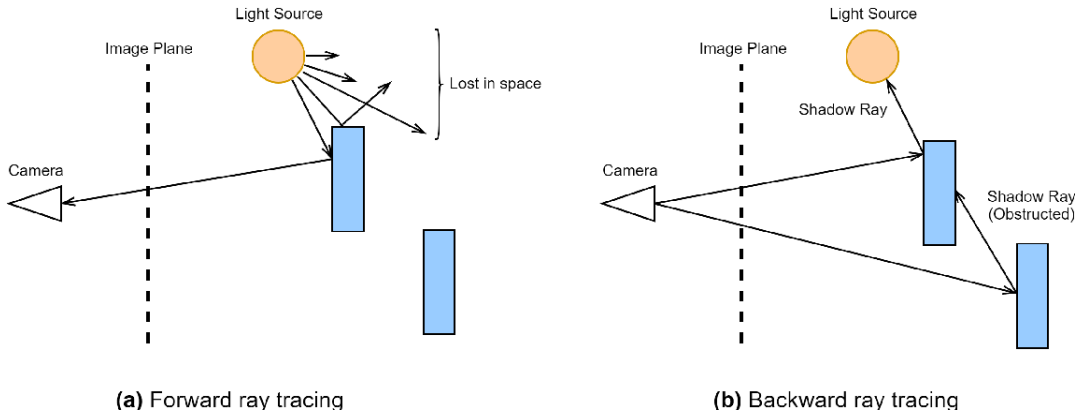

(a) Forward ray tracing **(b)** Backward ray tracing

Figure 2.3: Comparison between forward and backward ray tracing based on [45]

LightTools by Synopsys offers the possibility of using forward ray tracing and is hence chosen for simulations in this thesis. Ray tracing in LightTools assumes particle nature of light rays and hence wave phenomena like interference and diffraction are ignored. LightTools employs the Montecarlo simulation technique, emitting light rays in all directions to ensure a homogeneous spread of rays over the entire aim area. The tool also allows for a macro-based rotation of the light source to different locations. Additionally, it provides a ready user interface (unlike Radiance) and has a vast database of material properties and coating libraries from which users can select the required optical profiles for surfaces or even define their own custom optical properties.

In his thesis, Muthukumar [46], developed a methodology for irradiance modelling of complicated BIPV geometries using ray tracing (shown in Figure 2.4). The method involves determining the sensitivity of the model to different positions of the sun in the sky (sensitivity block) using LightTools and coupling it with actual sun position, at that location, throughout the year (sky block) to determine the annual irradiance incident on the PV surfaces. The same approach is adopted in this thesis and the following subsections will elaborate on each of the blocks in the figure in the context of the PV curtain.

2.1.1. Geometry preparation

The first step in the irradiance modelling is preparation of the curtain geometry. LightTools provides options for developing solid geometries, but of relatively low geometric complexity. To have greater design freedom, Rhinoceros 5.0 (Rhino) Educational software package is chosen instead for geometric modelling. A room having the curtain, will be developed and then be imported as STEP file for use in LightTools. By trial and error, it has been observed that LightTools is computationally heavy and time consuming for accurate simulations

when solid semi/ fully transmitting geometries are involved. This can be best visualized for geometries involving solid glass (such as in case of glass in the model), which allow for multiple internal reflections and refractions that need to be computed every time a ray of intensity above the minimum threshold set, strikes the surface. To counter this, all objects in the 3 Dimensional (3D) model are made of two-dimensional surfaces instead, with their optical properties adjusted to represent the three dimensional object so as to minimize computational time.

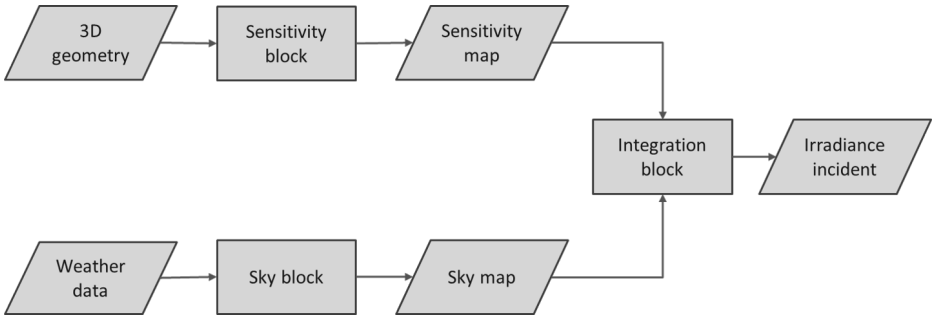

Figure 2.4: Approach for Irradiance Modelling based on [46]

Two geometries will be analyzed in this report:

- Target room: Master thesis office room LB02.490 in the Electrical Engineering, Mathematics and Computer Science (EEMCS) faculty of Delft University of Technology (TU Delft) is chosen for placing the solar curtain in and will be henceforth referred to as office room. The office model is discussed in more detail in chapter 4.1.
- Validation model: A scaled down model (approximately 1:6) of the office room will be tested for validating the simulation with real results. The aim is to test if the software model can be validated with the exact experimental set-up before being applied to the office room for annual simulations. This model will hereafter be referred to as validation model and be explained in more detail in chapter 3.

As a base case, the **percentage of PV in the total curtain area is taken as 30 %** for both models. These are incorporated as vertical strips of PV interleaved with semi-transparent cloth in the 3D curtain models. 30 % PV is chosen as the base case to ensure a fair level of PV in the curtain, without compromising with its overall semi-transparency. The model's sensitivity to the percentage of PV considered here will be explored in chapter 4.1. A **linen based textile sourced from the local market in Delft, having roughly 62 % transparency in the visible range of wavelengths**, is used as the curtain cloth for the base case throughout the thesis. Optical properties of the cloth will be discussed in chapter 3.

2.1.2. Sensitivity block and sensitivity map

The sensitivity block of the irradiance model takes the 3D geometry from Rhino as an input and generates a sensitivity map as output. The internal break-down of the sensitivity block as per Muthukumar's [46] approach is seen in Figure 2.5. The intermediate steps are listed as follows:

- Once the 3D geometry is imported, optical properties for each object in the model must be set. These may be set by the user according to real measurements or from literature or picked from the LightTools optical library.
- Next, a light source needs to be modelled to simulate the sun. The light source created must be such that it results in an irradiance of 1000 W/m^2 on the target PV surface. The spectrum must also be set to Air Mass (AM) 1.5 to match Standard Test Conditions (STC) [47]. The source must be placed very far from the object of interest so as to generate a parallel beam on the PV surface. Artificial lights if necessary, may be user defined or imported directly from the LightTools source library.
- To begin the simulation, a macro is run to circulate the sun-source to every point in the discretized sky dome and the intensities of rays on the PV surfaces, in each case, are recorded. In this manner, all

self-shading effects as well as the effect of optical reflections within the structure itself are taken into account.

- Using MATLAB scripts developed in TU Delft by Dr. Rudi Santbergen as cited in [46], the intensities of rays impinging on the PV curtain for different locations of the light source are processed to obtain the sensitivity of the PV surfaces (in their plane of array) to every angle of incidence and thus, a sensitivity map is generated.

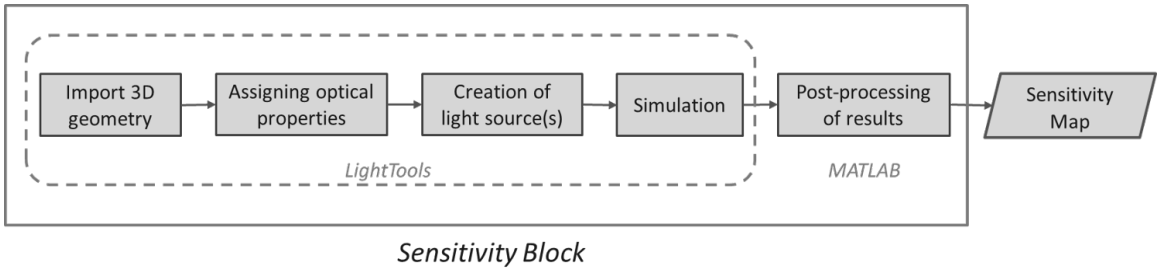

Figure 2.5: Sensitivity Block break-down

2.1.3. Weather data

Meteorological data, mainly regarding the sun position and irradiance profiles at the location of interest are imported from reliable sources such as Meteonorm [48]. Depending on the level of accuracy desired, hourly or ten-minutely data can be imported. In particular, information regarding the time of the year, sun altitude, sun azimuth, DNI and DHI for an entire year at least, must be imported.

2.1.4. Sky block and sky map

The sky block takes the weather files as input and generates a skymap as an output. These steps are entirely carried out in the MATLAB environment using the scripts developed by Dr. Rudi Santbergen as used in [46]. The internal steps taking place in the sky block are listed below:

- The first step is to mesh the sky dome into a desired number of nearly equal units. Depending on the recursion factor selected by the user, the sky is discretized into a number of elements ranging from as low as 40 to even higher than 40,960 elements. Higher the number of elements, more the number of simulations that need to be run in ray-tracing (to ensure that every point in the sky map has a corresponding point in the sensitivity map developed by the sensitivity block). Thus, a trade-off between accuracy and computation time is made while choosing an ideal recursion factor of 4, resulting in 2560 sky elements.
- The imported weather files aid in determining the sun position at each time instant. While the direct normal irradiance at that time instant is simply added to the corresponding sky element that coincides with the location of the sun in the sky, diffuse irradiance is modelled using the third Perez model as explained in [46] to yield the skymap for each time instant.

2.1.5. Integration block and irradiance incident

The sky map for each time instant and the sensitivity map are multiplied to obtain the irradiance incident on the PV surfaces at each point in time. The equation 2.3 [46] used to calculate the irradiance for a given time instant in the year is given as:

$$Irradiance = \int_{dome} Sensitivity \cdot Sky\,Radiance\ d\Omega \tag{2.3}$$

where $d\Omega$ is the area of the infinitesimal sky element.For an annual simulation of hourly resolution, adding up all the hourly irradiance values yields the total irradiance incident on the PV surfaces annually. An example of the entire approach described applied by Muthukumar [46] to a complicated BIPV geometry by ZigZag Solar can be seen in Figure 2.6.

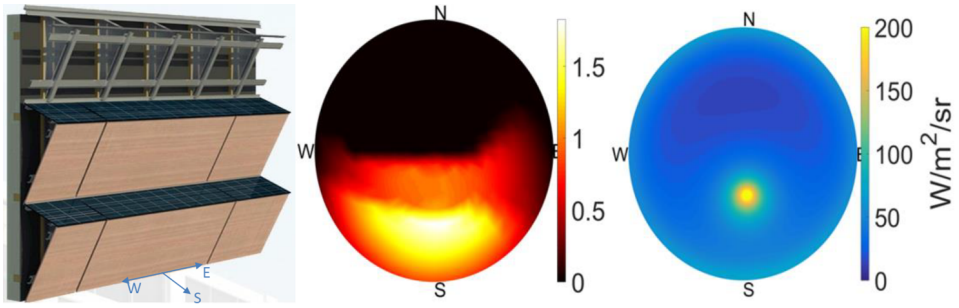

Figure 2.6: (L->R) BIPV structure designed by ZigZag Solar to reflect light onto the PV modules; Sensitivity map for a fixed orientation of the PV system to every angle of the sun's inclination; Sky Map indicating direct and diffuse irradiance for the given time instant at the given location

2.2. Electrical modelling

Translating the results of incident irradiance from the previous section into loads satisfied by the BIPV product when installed in a building, is the primary purpose of the electrical model. As seen in Figure 2.1, the electrical model considered in this thesis comprises a charge controller with maximum power point tracking, a battery bank and DC loads supplied by the system. Detailed modelling of power converters for conditioning of the PV power is beyond the scope of the current research. Thus, as a starting case, only DC loads will be supplied, with a higher emphasis on battery cycling for different DC load combinations than inverter and charge controller characteristics. This section starts with an overview of assumptions used in subsection 2.2.1, followed by load cases considered and battery sizing approach.

2.2.1. Assumptions

Since power electronics are not modelled, the following assumptions are made:

- One by-pass diode is to be incorporated per PV cut-cell in the curtain to ensure that shading has an impact only on the performance of the shaded cell and not of the entire string connected to the given cut-cell. The effect of shading in the simulation model translates to lower irradiance received by the PV surface and thus to lower power output from the shaded cell only.
- Irradiance incident is converted to electrical output by multiplying it with cut-cell efficiency. This is measured under standard test conditions in the controlled environment of the laboratory using a Neonsee steady state >class AAA solar simulator [49].
- Since the cloth part of the curtain is semi-transparent, it is assumed for simplicity, that the curtain is kept closed throughout the sunshine hours. While this setting allows sufficient non-glare daylight to enter the room, it also helps harness maximum PV output.
- DC cable losses are determined using Ohm's law. Constant temperature of operation, due to indoor environment, is assumed.
- An efficiency of 98 % is assumed for the charge controller-MPPT unit from datasheets of commercially available variants [50][51].
- Lithium ion (Li ion) technology is chosen for the battery in the PV system design. Its mass, power density and longer life compared to lead acid make it a favorable choice in this case [52]. A charge-discharge efficiency of nearly 99 % is another advantage [53]. Thus battery charge-discharge losses are assumed negligible.
- Depth Of Discharge (DOD) of the Li battery directly affects the life of the battery [54]. As a trade-off between size and life of battery bank, two cases of 60 % and 80 % DOD are chosen.

2.2.2. Load descriptions

Since the PV curtain is to be placed in a room in a building, two categories of load profiles can be generated based on the room use. Thus, two load cases- one for a PV curtain in an office room and one for a PV curtain in a residential room have been considered. Location of Delft in the Netherlands is assumed for formulating both load profiles. The DC load profiles for a typical day in each of the two cases are displayed in Table 2.1. Weekend variations and the influence of holiday seasons in the load profiles have been ignored for simplicity. The following specific loads are considered in drawing up the daily load profiles:

- **Laptop charging**: HP ProBook 440 G6 of TU Delft's laptop project is chosen as the reference laptop. With a battery capacity of 45 Wh and charge characteristics of 19.5 V charge voltage and 2.3 A peak current [55], this laptop reaches full charge in nearly 1.5 hours. Number of charges and time of charge is decided as per load case as shown in Table 2.1
- **Mobile charging**: Most smartphones today hover around the 3000 mAh mark [56]. Thus a 3000 mAh Li-ion battery of mobile is considered. A case of normal battery charge time of 2 hours for full charge is assumed as a good trade off between charge time and battery life (no fast charge considered). USB 3.0 charging at 5 V and 1.5 A (peak current) is assumed with charge characteristics assumed according to [57]. Number of charges and time of charge is decided as per load case as shown in Table 2.1
- **Decorative LEDs**: A string of LEDs for decorative purposes of 12 V 500 mA is chosen. The variant available online [58] also comes with remote control. The prospect of remotely controlling the lights in the future via voice control or other automation makes this load interesting. Since the sun path varies throughout the year ranging from sunset at 4:30 pm in the winter solstice to 10:00 pm during the summer solstice [59], hours of use would vary seasonally. This is assumed to be from 5 hours in the December (6:00 pm to 11:00 pm) to 1 hour in the June (10:00 pm to 11:00 pm). Usage is scaled from month to month according to sunset timings and kept constant for the entire month.
- **Curtain Automation**: Similar to the LEDs, another scope for automation is the opening and closing of the curtain. For simplicity, power consumption of any control units for the automation is assumed negligible. The power requirement of a simple stepper DC motor for automating the motion is about 4.83 V 0.84 A [60]. This motor is primarily chosen due to its compatibility with platforms like Arduino that can be used for automating the curtain. Each action of open and close is assumed to take 5 minutes. Thus, in the load profile, the motor load is distributed over half hour by dividing it by 6 since the minimum time step considered here is half hour. Two cycles of open and close are assumed throughout the day, mostly depending on sunrise and sunset times to avoid glare inside the house and harness maximum PV power. In this thesis however, due to the minor influence of the power requirements of the DC motor, the seasonal influence is ignored and the curtain is assumed to be closed during sunshine hours (constant from 6:00 am to 10:00 pm). The thesis assumes the cloth portion of the curtain to be semi-transparent which ensures that there will always be diffuse light entering the room, even if the curtain is closed.

Table 2.1: Load profile description for residential and office room case

Appliance	Power rating	Hours of use	Seasonal variations	Energy required (Wh)	Comments
			Residential case		
Curtain automation	4 W 4.83 V 0.84 A	0.33	yes	1.32	Two cycles of open close: morning and evening unless other user input
LED string	6 W 12 V 500 mA	1 to 5	yes	6 to 30	Usage dependent of sunshine hours
Mobile charging	7.5 W 5 V 1.5 A (peak)	4	no	<30	2 charge cycles of 2 hrs each
Laptop charge	45 W 19.5 V 2.3 A (peak)	3	no	<135	2 full charges of 1.5 hrs per day
TOTAL				172 to 196	(approximately)
			Office case		
Curtain automation	4 W 4.83 V 0.84 A	0.33	yes	1.32	Two cycles of open close: morning and evening unless other user input
Mobile charging	7.5 W 5 V 1.5 A (peak)	4	no	<30	2 charge cycles of 2 hrs each
Laptop charge	45 W 19.5 V 2.3 A (peak)	4.5	no	<202.5	3 full charge of 1.5 hrs per day
TOTAL				234	(approximately)

Load case 1: Residential use

In this case, as seen in Table 2.1, a combination of curtain automation, decorative LEDs, laptops and mobiles is assumed. It is assumed that the occupants (2) of the house are at work from 8:30 am to 5:30 pm. Hence all usage is typically shown from before or after these hours. Figures 2.7 and 2.8 show load profiles in the summer and winter respectively and Figure 2.9 shows the annual approximated load profile. Weekend variations and holiday seasons are ignored. The timing of various loads is explained below

- Mobile charging: Two charges considered, one from 6:00 am to 8:00 am and the second from 6:00 pm to 8:00 pm.
- Laptop charging: Two charges considered. One from 7:00 pm to 8:30 pm and the second from 9:00 pm to 10:30 pm.
- LED lights: Seasonal usage considered starting from 6:00 pm until 11:00 pm in December and starting from as late as 10:00 pm until 11:00 pm in June. The end time stays 11:00 pm but the start time ramps up from winter to summer and ramps down again from summer to winter.
- Curtain automation: For maximum PV power, curtain automation is such that it remains closed between 6:00 am and 10:00 pm, open for a while and closes again for the night to ensure privacy in the room.

The total annual load for this scenario amounts to roughly 48.86 kWh.

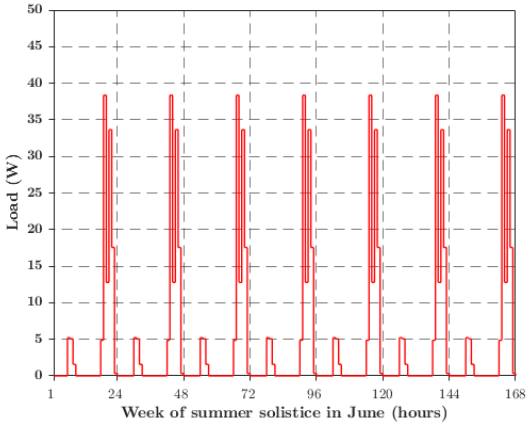

Figure 2.7: DC Load profile for a summer week in a residential home

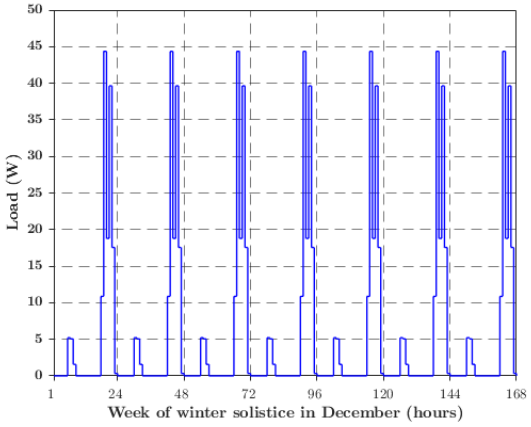

Figure 2.8: DC Load profile for a winter week in a residential home

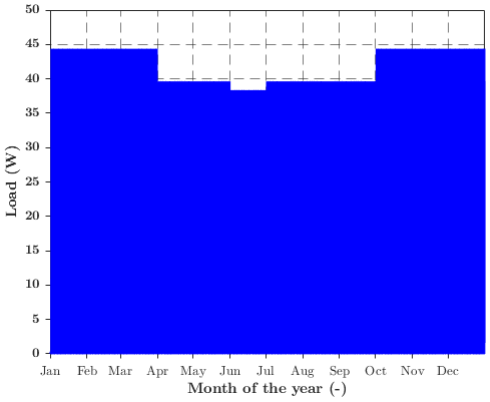

Figure 2.9: Annual DC load profile considered for a residential home

Load case 2: Office use

In this case, as seen in Table 2.1, a combination of curtain automation, laptops and mobiles is assumed. It is assumed that the office hours begin at 9:00 am to 5:00 pm. Hence all usage is typically shown between these hours. Since there is barely any seasonal loads, the load profiles look similar in summer and winter. Variations during weekends and holiday season are ignored. A typical weekly load profile is shown in Figure 2.10 and Figure 2.11 shows the annual approximated load profile. The timing of various loads is explained below

- Mobile charging: Two charges considered, one from 9:00 am to 11:00 am and the second from 2:00 pm to 4:00 pm.
- Laptop charging: Three charges considered. One from 9:00 am to 10:30 am, the second from 11:00 am to 12:30 pm and the third from 2:00 pm to 3:30 pm.
- Curtain automation: For maximum PV power, curtain automation is such that it is assumed to remain closed between 6:00 am and 10:00 pm.

The total annual load for this scenario amounts to roughly 57.76 kWh.

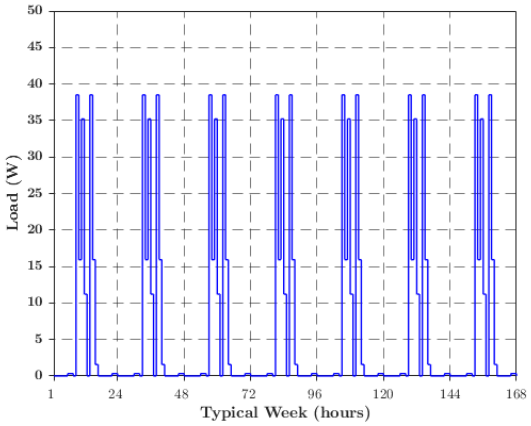

Figure 2.10: DC Load profile for a typical week in an office room

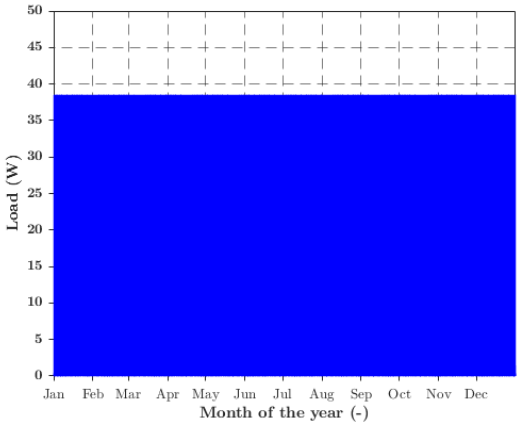

Figure 2.11: Annual DC load profile considered for a office room

2.2.3. Loss of load probability

The Loss Of Load Probability (LOLP) is a term commonly used in renewable energy off-grid systems to indicate the probability of the load not being met by the off-grid solution developed. In most literature, it is defined as the power failure time period divided by a given period of time (generally one year) [61]. For the two DC load cases proposed, LOLP will be calculated in this report using equation 2.4, to get a fair idea on the PV-load matching trends.

$$LOLP = \frac{Number\ of\ hourly\ load\ rejections}{Number\ of\ hours\ in\ the\ year} \tag{2.4}$$

Thus, both- the methodology for the irradiance model and the assumptions and load profiles for the electrical model- have been laid down in this chapter. The next chapter will apply the irradiance model to a scaled down version of the office room (validation model) and verify it with an experimental setup to prove the accuracy of the model. The irradiance model and the electrical model will then finally be applied to the office room case study in chapter 4.

3

Model Validation with Experimental Setup

A scaled down version of the office room with the PV curtain is modelled in this chapter with the purpose of validating the software simulation with an experimental setup. This is to ensure that the approach can be applied to gain insights on the performance of the real scale PV curtain in the office room, before fabrication. Four test cases have been prepared for this purpose, namely:

1. Reference Case: An empty room with the PV curtain.
2. Furniture Case: Reference room with furniture in it.
3. White wall Case: A white wall placed closer to the window, at less than half the length of the room, to simulate a smaller room with lower depth than the actual room
4. Black wall Case: Similar to the white wall case, but changing its color to black.

Each of these cases will be created in both the software model as well as the experimental setup and then compared for validation. Starting with the software model, section 3.1 will explain the application of the irradiance model described in chapter 2 for the validation model, section 3.2 will explain the details of the experimental set-up used, and section 3.4 will show the results of the tests, followed by a discussion on its interpretation.

3.1. Model description

The validation will be carried out in the controlled environment of the laboratory using the Eternal Sun Large Area Steady State Solar Simulator (LASS) [62] so that it can be replicated with a higher degree of certainty than in a real environment. The dimensions of the validation model are restricted by the size of the sun simulator which is 1.5 m × 2.0 m. The class AAA solar simulator works by shining a combination of lamps whose individual spectral distributions are superimposed to produce a near- AM1.5 spectrum. For likeness to AM 1.5 conditions, the sample must be placed in the centre of the simulator. Thus, a model one-sixth the scale of the true office room dimensions is chosen for validation. The following steps will elaborate each subsection of the irradiance model with respect to its application for the validation setup. Note that since the simulation is conducted indoor with direct normal illumination from the solar simulator, steps relating to the sensitivity map and sky map are omitted in this chapter.

Geometry preparation

A room of dimensions 1.08 m long × 0.72 m wide × 0.54 m high is modelled in Rhino 3D. (Note: These dimensions are selected due to availability of an identical setup already created by Dr. Hester Hellinga in the Faculty of Architecture under Dr. Truus Hordijk in TU Delft [63] and will be used in the experimental setup in section 3.2). The dimensional perspective view of the reference room developed in Rhino is seen in Figure 3.2. The room model in Rhino is made up entirely of surfaces. As mentioned in chapter 2, a PV integration of

30 % by area is assumed in the curtain and these are represented by strips that alternate with cloth to collectively form the curtain. This roughly amounts to 6 strips of 2 cut cells each when compared to the total area of the curtain. Details of the PV strip will be described ahead in section 3.2.2. The bifaciality of the PV in the curtain model is represented by having two exactly aligned surfaces separated by 0.001 mm so that front face and rear face power can be recorded separately during simulations. An assumption for curvature of curtain is shown in Figure 3.1 which shows that the entire length of the curtain is made of 5 waves, each of length- say L. Each individual wave is made up of two arches of width $L/2$ and height $L/25$ to maintain a smooth curvature throughout its length, much like a real curtain. A wireframe perspective view of the reference case (with dimensions in mm) is seen in Figure 3.2. Dimensional details of the reference case as well as the furniture and wall models can be found in Appendix A.

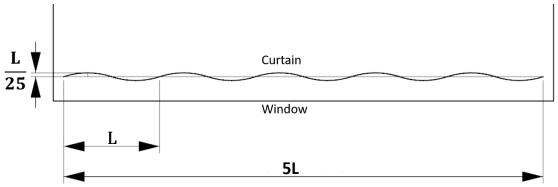

Figure 3.1: Top view of curtain in a room, showing dimensional assumptions for curtain curvature

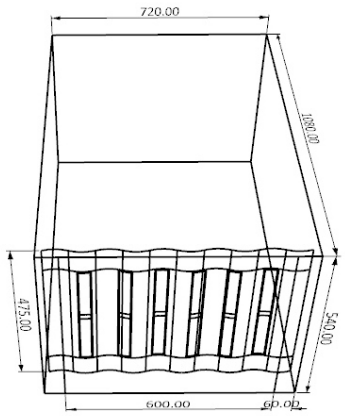

Figure 3.2: Perspective view of reference case model

Optical properties

After creating the geometry in Rhino, it is imported in STEP format in LightTools for ray tracing. As described earlier, all solid objects will be modelled as surfaces instead of solids to save on computational time. To not compromise on the accuracy of the model, it is necessary to account for these changes by adjusting the optical properties of these solid-surfaces in LightTools. For this, the following procedure is employed:

- All material properties in the model are set to air. This is done to ensure that the optical properties entered do not interfere with any contradicting intrinsic material properties.
- For glass walls, such as the single glass window in case of the validation model, the net absorptance, reflectance and transmittance is calculated from the geometry using Fresnel's equations and Lambert Beer's law (refer to Appendix B). The equivalent properties are then entered as wavelength and angle of incidence dependent, user-defined coatings for the glass in the LightTools library.
- For non-transmitting objects such as wooden furniture, flooring or walls in the room, the behaviour of surface and solid is approximated to be identical (due to absence of any total internal reflections) and thus the same global optical properties as that of the solid are applied to the corresponding surface. The effect of change of reflectance with thickness is assumed negligible.
- Wavelength dependent optical properties of the curtain cloth, wood, white walls, black walls, plastic encapsulation for the PV in the curtain, were measured using the LAMBDA 950 UV-Vis-NIR Spectrophotometer of Perkin Elmer. The measurement priciple, sample preparation and measured optical profile plots can be located in Appendix B.2. Note that the cloth chosen for this simulation is a moderately transparent linen fabric acquired from the local market and is kept constant (even for the office model), as the reference curtain material throughout this research.

A summary of material properties and assumptions is shown in Table 3.1:

Table 3.1: Summary of optical properties set and assumptions followed

Object in model	Optical properties- LightTools	Comments
	Reference case	
PV surfaces	Mechanical Absorber	Ensures that the irradiance recorded by the PV signifies total irradiance incident on its surfaces
Cloth	Simple scatterer- lambertian	Wavelength dependent measured optical behavior is weighted with the solar spectrum to obtain one value each for reflectance (R), transmittance (T) and absorptance (A). Lambertian behavior assumed from [64]
Curtain collars*	Simple scatterer- lambertian	Wavelength dependent measured optical behavior weighted with the solar spectrum to obtain one value each for R, T, and A. Lambertian behavior assumed from [64]
White interiors	Simple scatterer- lambertian	Optical properties for model given in the report of Hellinga [63] and lambertian behavior assumed from [65]
Flooring	Simple scatterer- lambertian	Optical properties for model given in the report of Hellinga [63] and lambertian behavior assumed
Plastic-EVA (around PV)	Smooth optical	Nearly specular behavior assumed [66]. Measured properties entered as wavelength dependent coating
Window glass	Smooth optical	Angular and wavelength varying reflectance and transmittance calculated (Appendix B.1.1) is entered as user coating for window
	Furniture case	
Wooden furniture	Simple scatterer- lambertian	Assumed to be a diffuse scatterer [67] since it is neither unfinished nor glossily polished. Measured wavelength dependent properties weighted with solar spectrum to obtain equivalent R, T, A values
	White wall case	
White wall	Simple scatterer- lambertian	Wavelength dependent measured optical behavior weighted with the solar spectrum to obtain one value each for R, T, and A. Lambertian behavior assumed from [65]
	Black wall case	
Black wall	Simple scatterer- lambertian	Wavelength dependent measured optical behavior weighted with the solar spectrum to obtain one value each for R, T, and A. Lambertian behavior assumed

*top and bottom thicker layers of double cloth that carry the cables

Defining the light source

A light source to simulate the sun is created as a volume source in the form of a cylindrical disc in LightTools as per the methodology described in section 2.1.2 of Chapter 2. With a spectrum of AM1.5 [47], the source is placed about 5000 m from the window of the room, such that it emits light normal to the plane of the window which forms its aim area. Since it is a scaled down version, to avoid complexity, artificial lights are excluded from the validation analysis.

Simulation run

LightTools simulations are based on the Montecarlo approach. It is thus necessary to calibrate the simulation environment for the right number of simulation rays such that any change in the seed that controls the randomness of the emitted fan of rays coming from the source, does not have a significant effect on the power recorded by the curtain (described in the Master thesis of Duran [68]). The calibration is conducted by introducing a surface, typically smaller in dimensions compared to the target surfaces and by varying the seed to check the deviation in power recorded by that surface for each new seed value. If the deviation is significant, the number of rays is increased. More rays directly translates into a more time consuming and

computationally heavy simulation and must be avoided, unless at the cost of accuracy. In this research, an obscure square in the corner of the room, as seen in Figure 3.3, is selected for calibration since accuracy for a nearly hidden corner in the room would guarantee accuracy for larger surfaces, closer to the light source, like the target curtain. From the calibration, it is decided to run the simulation for 10 million rays for a fair degree of repeatability between results. Each of the four cases described in the introduction of this chapter are simulated separately using forward ray tracing with 10 million rays each. The power absorbed by the front and rear faces of the PV strips in the curtain is recorded. The results of the simulation are tabulated and compared with the experimental setup in section 3.4. Figures 3.4-3.7 show the four cases prepared in LightTools. One side-wall in the model has been hidden for better visibility.

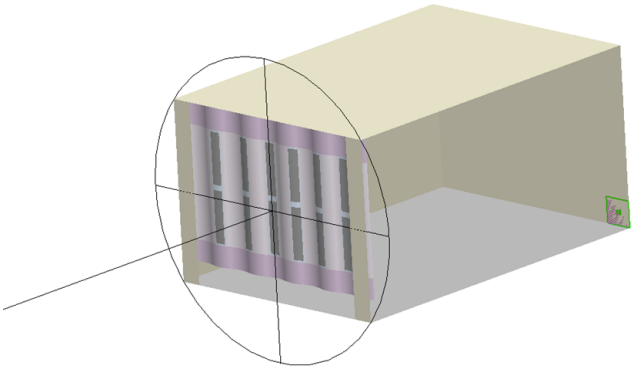

Figure 3.3: Model in LightTools with aim area marked as the black circle on the window and the corner calibration surface in green

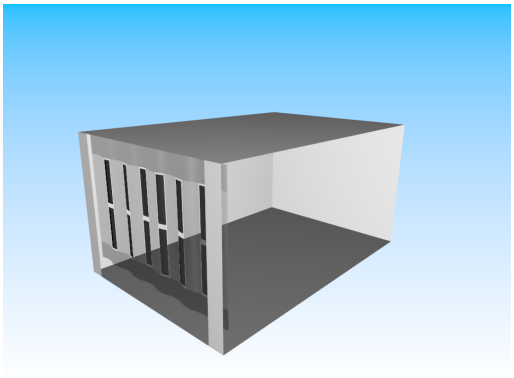

Figure 3.4: Reference case in LightTools

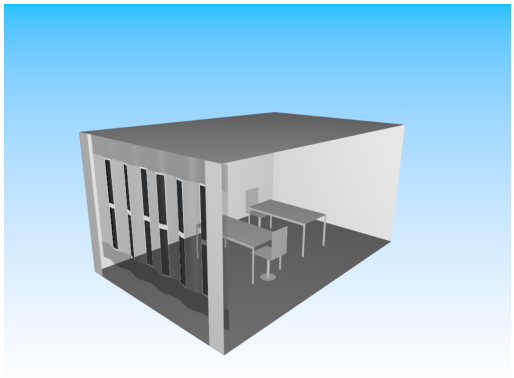

Figure 3.5: Furniture case in LightTools

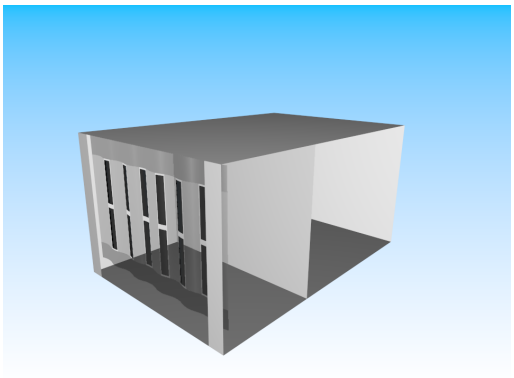

Figure 3.6: White-wall case in LightTools

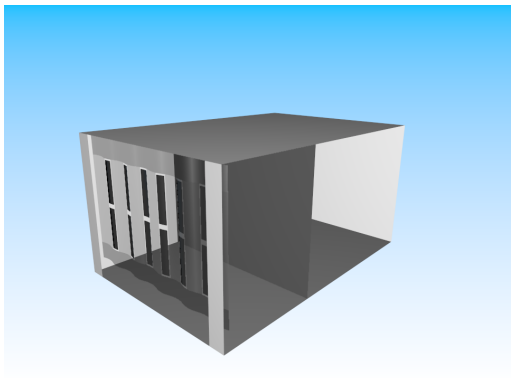

Figure 3.7: Black-wall case in LightTools

3.2. Setup description

The experimental setup for validation of the curtain model developed in section 3.1 is elaborated in this section. While subsection 3.2.1 gives an idea of the structure of the room used, subsection 3.2.2 explains how the crystalline silicon mini modules used in the curtain have been fabricated and characterized and finally subsection 3.2.3 shows the fabrication of the curtain from mini modules.

3.2.1. Architectural model

The architectural model acquired for experimental validation is shown in Figures 3.8 and 3.9. As seen in the figure, the window-side facade is removable, with four metal strips holding it in place. In the current research, the window facade shown in the figure is replaced by a second one as seen in the simulation earlier, with a 600 mm × 600 mm glass panel supported by two wooden flanks on both sides, both painted white internally, to match the color of the interior facade. All internal walls and ceiling are painted white with a reflection coefficient of 0.85 and the floor painted grey with a reflection coefficient of 0.20 [63]. The back wall and one side wall have a hole of 150 mm × 150 mm. Both are kept closed throughout the simulation and only used in the current research for taking photographs of the various cases. The intermediate wall for cases 3 and 4 is made of hardboard. One one side it is painted the same shade of white as the walls of the room (for use in case 3). On the other side side, it is coated with black paper which allows its use as the black intermediate wall in case 4 as well.

Figure 3.8: Image of scale-down model with removable window-side facade, adapted from [63]

Figure 3.9: Image of interior view of the experimental setup with removable furniture, adapted from [63]

3.2.2. Semi flexible mini modules

This subsection will elaborate on the mini modules produced as part of the validation model. First the fabrication process will be explained, followed by a discussion on the characterization techniques used to establish the quality of the solar cells and mini modules.

Mini module fabrication

For integrating bifacial PV in cloth, bifacial crystalline silicon Passivated Emitter and Rear Contacted (PERC) cells have been used [69]. The image posted by the manufacturer *Wisebiz* on an e-commerce site is shown in Figure 3.10. These 5 bus-bar mono crystalline cells have been laser-cut lengthwise into pieces 31.2 mm wide (distance between two busbars). To match the height of the window, a maximum of two such pieces can be connected end to end (with a centre gap for connections) to form a combined length of roughly 340 mm. Adding one more piece would mean a total length of about 520 mm, leaving hardly any room for the inter-connection circuitry between the mini modules that connect to form the curtain. Thus a system of two cells connected in series to form a mini module is chosen.

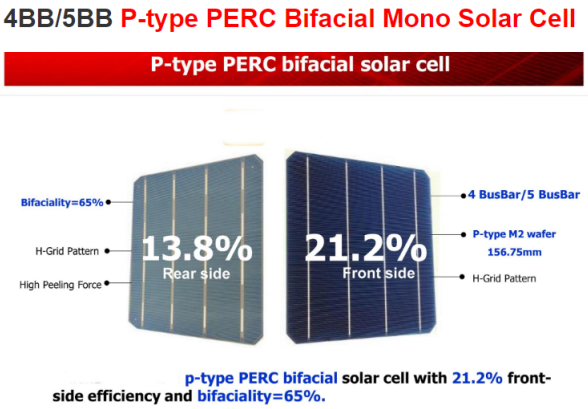

Figure 3.10: Snapshot of specifications mentioned by manufacturer of the bifacial PERC cells used in the current research

The process of making such a mini module is listed as follows:

1. **Cutting:** The complete solar cell is cut into pieces of width 31.2 mm using the Lasergraaf high power fiber laser cutter. The cutting parameters and working is described in Appendix C.1. Each piece retained contains one central busbar.
2. **Soldering:** Two such cut-cells are soldered in series using solder and liquid flux with a 1 mm wide, tin alloy coated, flat copper tabbing wire. Since these act as busbars, a low width tabbing wire is preferred, so as to shade minimum portion of the cell.
3. **Assembly:** The string of two cells is carefully sandwiched between two sheets of Ethylene Vinyl Acetate (EVA) slightly larger than the string area. The EVA is used as an encapsulant for the PV cell and is meant to protect it from adverse weather conditions. The EVA-PV string-EVA assembly is then placed between two transparent plastic foils which form the front and back sheet of the mini module.
4. **Lamination:** The assembly is carefully put on the preheated laminator platform and laminated for a cycle lasting 20 minutes at the end of which the finished mini module is ready. The operating principle of the laminator is briefly explained in Appendix C.2.

The entire chain is explained pictorially in the Figures 3.11 and 3.12 below:

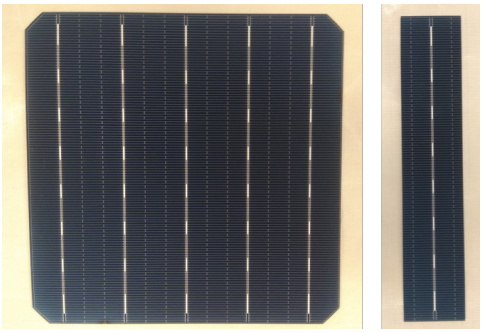

Figure 3.11: Bifacial c-Si full cell is laser-cut into strips

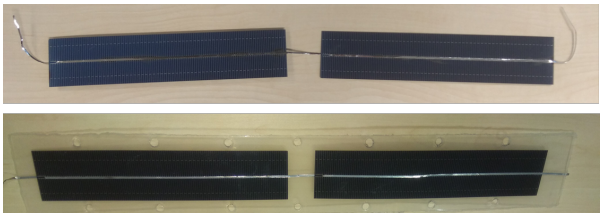

Figure 3.12: Two cut cells soldered together (above) and then laminated (below)

Solar cell characterization

Before assembling the mini modules to make a module in the form of a curtain, it is important to assess their quality. This comprises not only the mini modules that will be used in the curtain but also the full cell (laminated) to analyze the change in its performance because of the encapsulation and cutting. For this purpose, two tests are carried out- namely, IV (current(I) versus Voltage(V)) curve measurements and electroluminescence, procedures of which are explained in the sections below:

IV curve measurements

For IV curve measurement, the Neonsee solar cell analysis system at Solliance in Eindhoven is used. The set up is elaborated in Appendix C.4. To begin with measurements, the instrument is calibrated using the manual calibration mode. By shining the steady state Xenon light source in multiple bursts on the reference cell, the irradiance is set according to the maximum power point current (I_{MPP}) of the reference cell. Next, an attenuation cycle is run to set the various intermediate irradiance levels between zero and one sun illumination for ease of setting any in-between values during measurement. This attenuation of irradiance offers the possibility to tune the setup to a value lower than 1 sun illumination. This is particularly useful for conducting rear side illumination of the mini modules discussed in this research, under 0.2 sun illumination (often taken as an initial estimate for rear side illumination as per the under-development standard IEC 600904-1-2 [70] as cited in [71]).

While traditionally, for basic c-Si cell measurement, the Konica Minolta AK-200 c-Si reference cell is used, since the cells used in this research are of c-Si PERC bifacial technology , the instrument has been calibrated using one of the non-laminated bifacial PERC 6" × 6" cells from Wisebiz using the manufacturer's specifications of maximum power point current shown in the datasheet in Appendix C.3. Note, that this method of measurement introduces a degree of uncertainty, especially because of the uncertainty in the manufacturer's datasheet showing I_{MPP} fluctuations from 9.19 to 9.28. A intermediate value of 9.26 is chosen for calibration. The results in this section will only focus on measurements recorded using the bifacial full cell as the reference. The difference in the value of these measurements from the ones recorded using the Konica Minolta reference cell AK-200 can be located in Appendix C.4. Also hysteresis in capturing the IV curve is shown in the same appendix. A four-probe measurement technique, resulting in the elimination of sheet resistance, is used to obtain the IV characteristics for the cases listed in Table 3.2. All measurements are taken by placing the module on a black bed, ensuring that the rear side is shaded.

Table 3.2: IV curve measurement summary for samples tested under reference cell (c-Si bifacial PERC)

Sample	Side	P_{MPP} (W)	V_{MPP} (V)	I_{MPP} (A)	V_{OC} (V)	I_{SC} (A)	η (%)	Bifaciality (%)
Full cell (non-laminated)	Front	4.461	0.492	9.064	0.624	9.731	18.36	
	Rear	2.685	0.506	5.307	0.618	5.690	11.05	60
	Rear*	0.496	0.490	1.012	0.583	1.128	10.21	
Full cell (laminated)	Front	4.588	0.523	8.769	0.655	9.441	18.88	
	Rear	2.712	0.529	5.129	0.642	5.504	11.16	59
	Rear*	0.508	0.507	1.002	0.599	1.101	10.45	
Mini module	Front	1.923	1.057	1.820	1.318	1.939	**19.66**	
	Rear	1.377	1.046	1.317	1.284	1.403	14.08	72
	Rear*	0.258	0.987	0.262	1.180	0.281	**13.21**	
Cut-cell (non-laminated)	Front	0.945	0.512	1.846	0.632	1.970	19.31	
	Rear	0.592	0.514	1.152	0.622	1.228	12.10	63
	Rear*	0.111	0.489	0.227	0.583	0.246	11.35	
Cut-cell module (laminated)	Front	0.955	0.523	1.827	0.654	1.961	19.52	
	Rear	0.649	0.522	1.243	0.640	1.333	13.27	68
	Rear*	0.120	0.491	0.244	0.588	0.266	12.25	

*rear side at 0.2 sun (200 W/m^2) illumination

Note that the extra row on rear illumination at 200 W/m^2 is added as a realistic comparison according to industrial standards being discussed in the bifacial PV market [71]. This involves using the bifaciality times 0.2 sun illumination as a factor to add to the 1 sun illumination to be incident only on the front surface instead of illuminating both sides. This is also more realistic since in real conditions, the rear side in the curtain will never see as high irradiances as 1 sun. Since the irradiance of the source in the measuring instrument could not be tuned to a higher value without the loss of accuracy, results for 1 sun illumination on the front face plus results of 0.2 sun illumination for the rear side illumination will be considered as the net power output of the cell / mini module being characterized.

The following observations can be made from Table 3.2:

- While the manufacturer's datasheet states a bifaciality of 65 %, the non-laminated sample tested shows

a bifaciality of 60 %. Poor contact at some of the electrode terminals on the cell due to manual soldering and increased shading losses due to wide busbars are attributed to these differences.

- Using this cell as a reference cell, it is found that the laminated cell gives a marginally better efficiency. This is attributed to optical coupling that results in an enhancement in anti-reflective properties of the cell and stronger electrical contact points resulting from EVA-foil lamination.
- The effect of cutting the cell is unfortunately not visualized well in these measurements since the cut cells (both laminated and non-laminated) show a better performance than their respective full cells. This could be because a lower current generated by the cut cells due to their smaller size, results in lower current losses as compared to a full cell. Besides this, poor electrical contact in the non-laminated full cell, air bubbles in the laminated full cell and shading effect of busbars are deemed responsible for this behaviour. In general, the effect of the cut was found to be negligible.
- With an efficiency of 19.66 % and bifaciality of 72 %, the performance of the mini module to be used in the curtain is seen to be the best. A maximum power of 2.09 W (1.84 W (front) + 0.249 W (rear: 0.2 sun)) is recorded of the multiple mini module samples tested. This makes the total curtain in the validation model, a nearly 12.5 W installed power system (subject to albedo of the rear facing environment). Figure 3.13 shows the IV curves of the front and rear faces of the mini module.

Now that the efficiencies of the individual mini module (19.66 % front and 13.21 % rear) for the curtain have been established, the same efficiencies will be assumed for the finished curtain module while converting the LightTools simulation irradiance results into electrical PV power. Note that the model is made such that 1000 W/m^2 is incident on its front face.

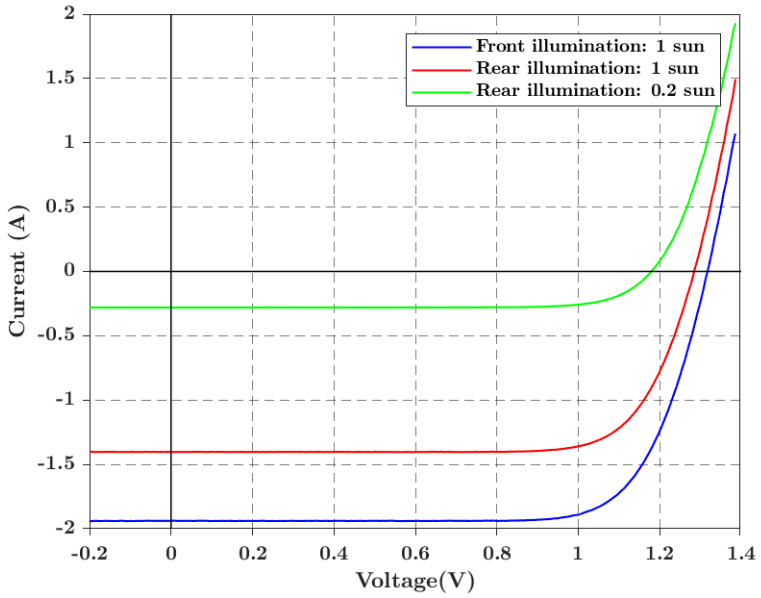

Figure 3.13: IV curves of the mini module to be used in the PV curtain validation model

Since a higher effective irradiance to simulate bifacial conditions cannot be obtained using the current measurement setup, instead, as a trial, a bifacial environment is simulated by introducing a platform (courtesy: Klaas Bakker, Solliance) inside the solar simulator. The mini module is suspended on top of the hollow platform and a white sheet (Figure 3.14) is placed at the base of the platform, about 16 cm away. The same procedure is repeated with a black sheet instead and the two results are compared with the front side illuminated IV in Figure 3.15. It is seen that the black sheet reflector gives a slightly better IV than the base case, while the white sheet reflector gives a much higher I_{SC} of nearly 2.419 A and a P_{MPP} of 2.36 W. This reveals that despite the color, most black surfaces are not perfect absorbers. Hence even slight reflections (5 %) are found to result in a slightly better performance than a case having no reflectors on the rear side. It will be interesting to note if this kind of a behaviour is observed also in case of the white wall and black wall cases

planned for the validation testing of the scaled down room.

Figure 3.14: mini module suspended on a platform above a white sheet for bifaciality

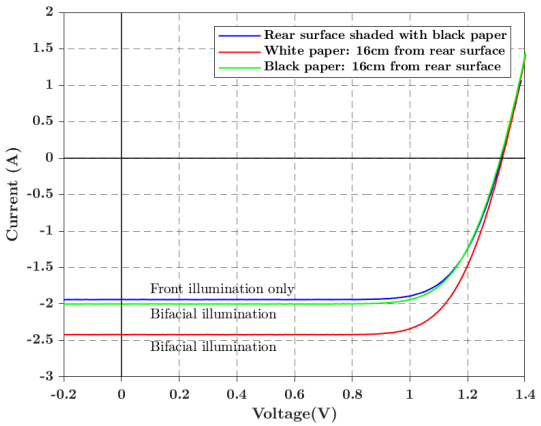

Figure 3.15: Comparison between IV curves for no reflector, white reflector and black reflector

Electroluminescence

Electroluminescence (EL) is a technique used for quality characterization of solar cells. It involves passing a direct current through the solar cell resulting in the emission of light due to radiative recombination of electron and holes in the semiconductor. Since silicon is an indirect bandgap material, recombination is dominated by Auger and other defect state related recombination. Still, the low radiative recombination is sufficient for detection when captured using a high resolution infrared-sensitive digital camera. The procedure for electroluminescence testing involves passing a current (close to the maximum power point of the solar cell) through the cell and capturing its luminescent image using the infrared sensitive camera. The brightness distribution in the photograph correlates with the distribution of the open circuit voltage, the minority carrier diffusion length, the series resistance, as well as with the quantum efficiency and the ideality factor of the examined cell [72]. Thus, any micro-cracks, poorly contacted areas and inactive regions appear as dark patches in the photograph. Figure 3.16 shows the elctroluminescence photograph for the mini module from the last subsection. The electroluminescence images for all other samples measured are shown in Appendix C.6. Since front and rear surfaces show nearly the same electroluminescence profile (thinner busbars in case of front side), only rear side photographs are shows due to higher resolution of images.

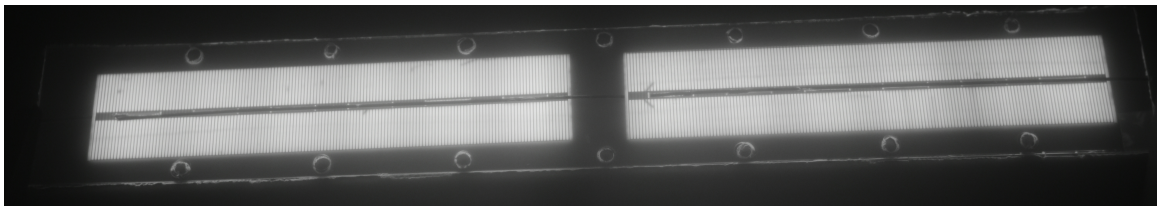

Figure 3.16: Electroluminescence image of rear side of bifacial mini module

The image shows few micro-cracks, especially on the right side cut cell in series but in general, the performance seems reasonable due to the absence of specific dark areas in the electroluminescence imaging.

3.2.3. Cell to module: curtain fabrication

To create a curtain out of the PV strips fabricated, it needs to be incorporated in a cloth base. The semi-transparent cloth (optical properties in Appendix B.1.1) is cut into strips and hemmed by hand stitches to smoothen out rough edges. To have 30 % integration of PV in the cloth (reference case assumed in this report), the ideal width of the strips should be 60 mm, but due to human error of imperfect stitches, the width of cloth strips prepared are found to vary between 55 mm to 70 mm. The hemmed cloth strips are then stitched

together with the PV strips. Holes are punched in the plastic encapsulation of the PV mini modules to facilitate the connection (as seen also in Figure 3.16). To convert the individual mini modules into the curtain module, they must be connected to one another. The choice between series connection or parallel connection is often determined by the choice of power converters being used and loads being served. Since this is a validation model, no loads or power converters are used. As a result, for simplicity, a configuration having all mini modules connected in series is preferred. This makes the curtain approximately a 12.54 W module (front side: 1 sun and rear side: 0.2 sun illumination). Figure 3.17 below shows the scaled down curtain in its intermediate stage and Figure 3.18 shows the curtain in a later stage, after the tabbing wires used for connecting the cells in series have been enclosed in the top and bottom collars of the curtain.

Figure 3.17: Intermediate stage of curtain fabrication after connecting cloth and PV strips

Figure 3.18: Tabbing wires between mini modules enclosed in cloth collars to make curtain module

Finally, to mount the curtain inside the scaled down room box, 3 mm holes are drilled at the top of the two side flanges next to the window, one in each flange such that the line joining the two holes is parallel to the width of the box. Two hooks are inserted into these holes, with the hook side inside the room so that a rod can be mounted, supported on both ends by the hooks. This forms the curtain rod for the room. Before mounting the second end of the rod onto the end hook, the curtain is slid onto the rod by means of the hollow created in the top collar that encloses the tabbing wires. The two terminals of the series connected curtain module are brought out to the top of the box from the top cloth collar, for measurements. The experimental setup is now ready. The experimental setup uses flat tabbing wire for connecting the mini modules to one another. This restricts the action of opening or closing the curtain. In a real case, the tabbing wires would be replaced by coiled cables, thus facilitating the action of opening and closing of the curtain.

3.3. Design of test bench

For designing the test bench for validation with the experimental setup, the following measurement devices have been used:

- Eternal Sun LASS [62] solar simulator: The solar simulator having a AAA-class solar spectrum is shown in Figure 3.19. AAA indicates that the spectral match, uniformity and stability of the simulator is of A class quality. Traditionally, to conduct IV curve measurements at STC, the module under consideration is placed on a table, right below the lamps in the simulator (equipment in the centre of the figure), PV side facing upwards. The two terminals of the module are connected to a voltage supply and ampere meter which are part of the LASS package [73]. A thermocouple is also connected to the module since it is susceptible to rapid heating when placed under the LASS and thus the IV generated will have to be

corrected for temperature to match STC values. Additionally, a c-Si reference cell on the table, is used to correct the reading for any variations in irradiance seen by the module.

- Pico Technology's Thermocouple Data Logger [74]: The TC-08 data logger (Figure 3.20) comes with 8 channels in which thermocouples can be inserted to record temperatures at different points in the model. With high resolution and accuracy for recorded data, the logger can record changes in temperature across milliseconds.

Figure 3.19: Large Area Solar Simulator for STC IV-curve tracing [62]

Figure 3.20: Pico TC-08 datalogger for thermocouples [74]

The experimental procedure is explained below:

1. The model room, carrying the PV curtain, is placed on top of a metre high movable table so that the setup can be wheeled to a set position in front of the LASS solar simulator. A table of such height is chosen to ensure that the window of the model lies nearly in the centre of the simulator's lit area as shown in Figure 3.22. Such a position aids in achieving a spectrum close to AM 1.5. Markers are added above the wheels of the table and on the floor beside the LASS, to aid in perfect alignment.

Figure 3.21: Test rig with reference cell on yellow pole mounted close to curtain

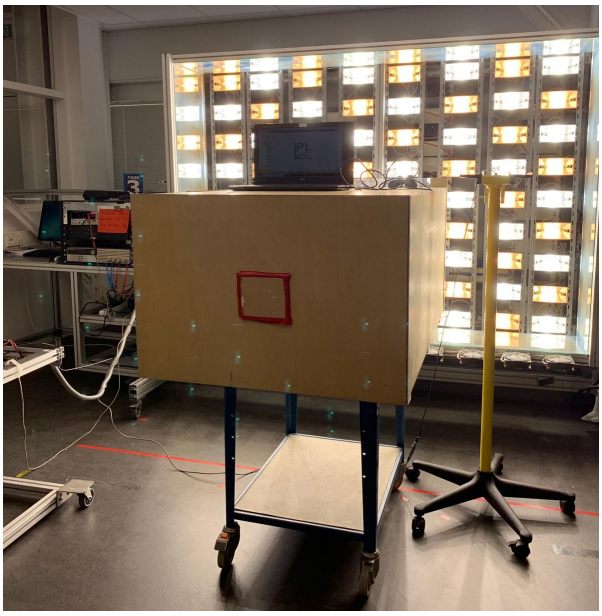

Figure 3.22: Complete test bench with validation model on table, 90° rotated LASS, reference cell and temperature sensors coupled

2. Thermocouples are connected to 6 different points in the setup: PV strip 1 - inside the room, PV strip 4 - inside the room, PV strip 6 - inside the room, lower portion of the glass window-inside the room,

lower portion of the glass window - outside the room and finally at a sidewall - inside the room. These positions can be visualized in Figure D.1 of Appendix D.1.

3. The reference cell of the LASS is mounted on a pole at the same height as the window of the model, right next to the model so that it can correct for irradiance.
4. In the ReRa tracer software for the LASS, module properties are entered as follows: Module Area = 0.0587 m^2, Single Cell Area = 48.9 cm^2, Strings per Module = 1, Cells per string = 12.
5. The two end terminals of the model are connected to the voltage supply and ampere meter of the LASS.
6. Each of the four cases -Reference, Furniture, White-wall and Black-wall cases are run consecutively and the IV curves using ReRa tracer are recorded.

The figures 3.23-3.26 below show the different validation cases realized in the experimental setup, clicked from the two holes in the side wall and back wall.

Figure 3.23: Reference case

Figure 3.24: Furniture Case

Figure 3.25: White wall case

Figure 3.26: Black wall Case

3.4. Results and discussions

The results of the experiments and simulation are elaborated in this section. Beginning with the experimental results, a summary of temperature distribution in the model and variations from case to case are discussed in subsection 3.4.1, power measurement results are shown in subsection 3.4.2, simulation power output is shown in subsection 3.4.3 followed by a discussion on validation in subsection 3.4.4.

3.4.1. Temperature distribution across the model

The temperature across the model for the reference case, at the time of IV capture, recorded by the datalogger is shown in Figure 3.27. As seen from the figure, the temperatures of the PV modules and glass are nearly in the same range whereas the ambient inner room temperature is much lower. Even between cases, this kind of a pattern between values is observed with temperatures on the inner wall being quite stable around 25°C irrespective of the glass and PV temperature. This could be due to the large volume of the room that causes an even distribution of heat avoiding any significant rise in temperature in the short time span of the roughly

five-minute-long measurements. It is also observed that all PV surface temperatures do not vary much from one another, within each case. Thus, for each case, the average of the temperatures of the PV mini modules is assumed as one average module temperature. Figure 3.28 shows a comparison between PV module temperatures between the cases. Despite a low variation between cases, for a fair comparison with simulation results (simulated for STC temperatures), temperature correction of IV curve must be performed.

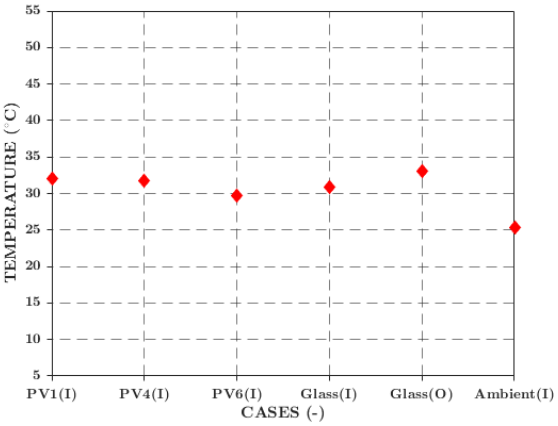

Figure 3.27: Temperature across the room during measurement

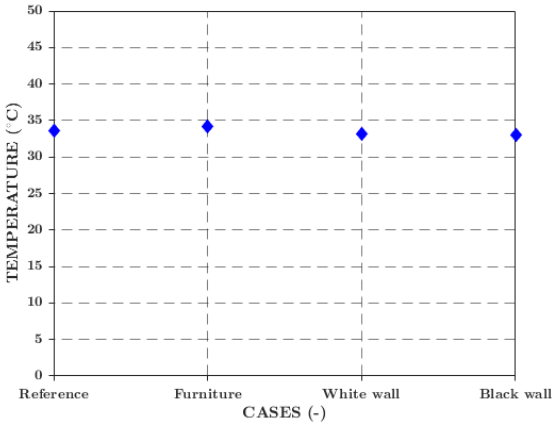

Figure 3.28: Comparison of module temperatures across cases

3.4.2. Measured power

The detailed IV curve data for all 4 cases is shown in Appendix D.2. The measured data is first corrected for temperature to bring it to STC scale. Temperature coefficient for maximum power of the bifacial solar cell according to the manufacturer's datasheet (Appendix C.3) is -0.3673 %/K. The comparison between measured and corrected data is shown in Figure 3.29. Since the temperature of measurement is higher than 25°C the readings recorded are lower than what they would be, had the measurements taken place at STC temperature. After temperature correction, it is seen that the reference case would have generated 12.32 W at 25°C instead of the 11.94 W it generated at 33.6°C.

3.4.3. Simulation results

LightTools simulation results give an idea of irradiance absorbed by each side of the PV cells in the model. By multiplying the irradiance per side (front or rear) of the PV with the corresponding side efficiency, the net PV electrical power is calculated. From section 3.2.2, a practical front efficiency of 19.66 % and rear side efficiency of 13.21 % is assumed. The comparison is shown in Figure 3.30.

3.4.4. Validation

Figure 3.31 shows a plot of temperature corrected STC results of the experimental measured PV power compared with the LightTools PV power results. The plot shows that the trend of slight increase in power between reference case and furniture, followed by a much higher power output for the case of a white intermediate wall and a lower power for the black intermediate wall case. The trend is followed in both the measured data and simulation results. The slight increase in power due in the furniture case could be attributed to the higher reflectance of the furniture of roughly 55 % in the visible wavelength range compared to the floor reflectance of 20 %. In case of the white wall, it is intuitive that a shorter room will result in higher daylight reflection of incoming radiations. In this case, more high intensity rays are intercepted at a shorter distance and reflected back to the window. Thus, more power is recorded as compared to the reference room case, where the intensity of reflected light is much reduced due to the higher path length of the light ray to the rear wall and back. For the black wall case, it may be initially anticipated that most of the light is absorbed and very little or none reflected back to the window. This would hold true if the material of the wall was a perfect absorber. In the current research however, the wall material showed a reflectance of 20-30 % in the near infrared zone

between 650 nm - 1200 nm. Since this lies in the sensitivity zone of the PV, it results in a higher net power output for the black wall case than what it would have been if a perfect absorber had been used. Moreover, since the light reflected is of high intensity due to the positioning of the wall 680 mm closer to the window, this 20 - 30 % reflection of high intensity rays is seen to have a higher effect on rear side PV power than in the case of the reference room, again due to the high path length for rays travelling from the window to the rear wall and back.

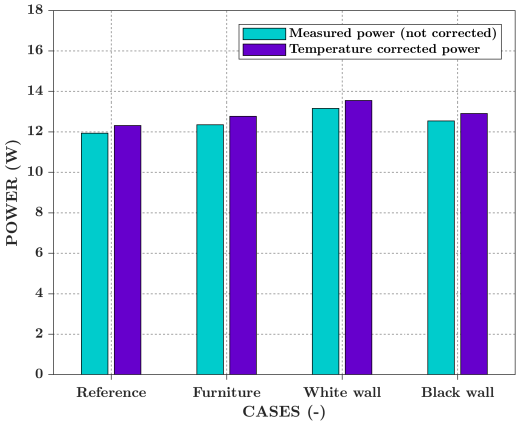

Figure 3.29: Measured readings versus corrected readings

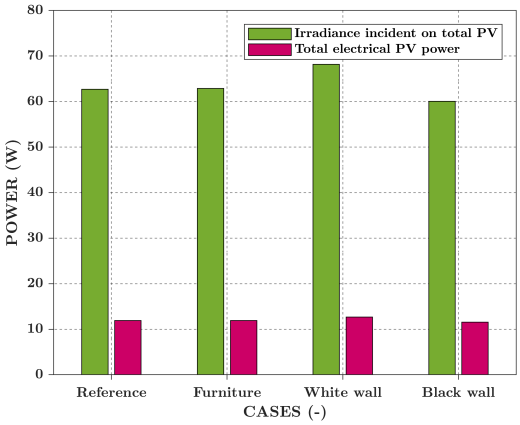

Figure 3.30: LightTools: Irradiance recorded versus PV power

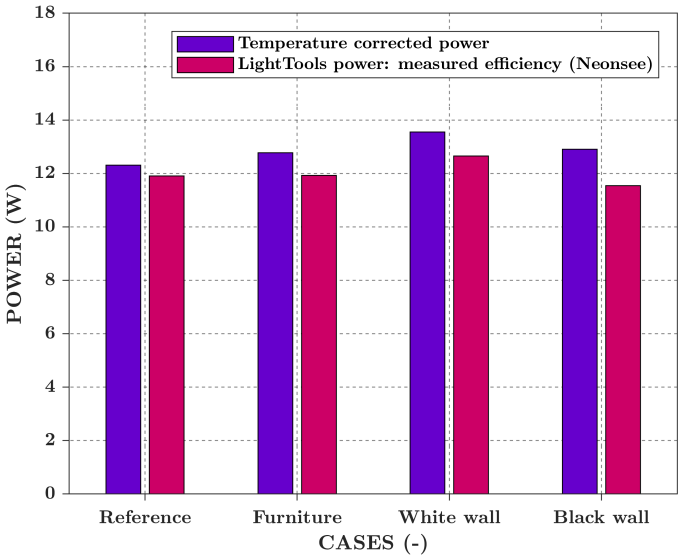

Figure 3.31: Temperature corrected results versus simulation results

Despite nearly matching trends, the scale of results from the simulations is seen to be slightly lower than the recorded results. This could be attributed to the following general causes :

- During measurements, power in the entire model is corrected according to the reference cell mounted on one side of the validation room box. However, the irradiance profile is seen to vary across the window depending on the combination of lamps directly in front of the point where the measurement is being taken. This poses an uncertainty in measurement results that cannot be easily accounted for by corrections due to variations not only in irradiance values recorded across the different PV strips but also due to the variations in spectral distributions across these strips. An over-correction of irradiance could be responsible for higher apparent measured results.

- Cell efficiencies obtained from characterization are used to convert irradiance from the LightTools model to PV power. The characterization however assumes the non-laminated but connected (with tabbing wire busbars), full bifacial cell as the reference cell by setting its I_{MPP} to 9.26 A. The cells from one batch are said to vary in I_{MPP} from 9.18 A to 9.28 A. The output of a set of 8 cells from later measurements at a bifacial cell-specific measurement unit, that used the base cells without any shade inducing busbar tabbing wires, showed 9.0 A as the maximum achieved I_{MPP} (shown in appendix C.5) from all samples tested. The results also showed a front face efficiency of 20.3 to 20.5 % unlike the 18.36 % reported using the earlier measurement technique. This mismatch could be responsible for an underestimation of efficiency, translating to a lower overall power output from the simulation model compared to experimental results.

- In this work, reflectance values for the floor and walls of the architectural unit have been taken from the report of Hellinga [63]. The unit was built at least 6 years before the current measurement period. Any age related fading, change in optical properties have not been taken into account in the current research due to lack of appropriate measuring equipment for that high a sample size. It is speculated by observation, that the reflectance of the floor is more than 20 %. This could be responsible for an underestimation of simulation results. Accuracy of other optical properties, especially their diffuse and specular reflectance components can be another source of error.

A more case-specific reasoning for the differences between simulation and experimental results is presented below:

- For the first reference case of an empty room, an error of 3.3 % was observed. Assumptions related to material properties and cell-characterization taken in the simulation model are attributed to this error. Since it is well within 5 %, this error is most acceptable.

- The furniture case, in simulation, gave results almost similar to the first one. This result is dependent on the reflective properties of the furniture. Real readings recorded show nearly 6.6 % higher PV power than simulations. This could be linked to the fact that the wood is entered as a lambertian scatterer in the model. Since the type used is neither perfectly glossy nor perfectly specular, it is difficult to assess which would be a better assumption to make in LightTools.

- The case of a white wall too showed nearly 6.6 % higher power in experiments than in simulation. Non-uniformity of optical properties can be considered as the most obvious cause for this. This could be because the intermediate wall (made of hard board) was painted by hand, resulting in unequal coats of paint at different spots, which is difficult to measure or represent accurately in LightTools. In addition, tiny gaps and spaces between the wall and the floor and ceiling could also have resulted in loss of a couple of rays to the back of the room.

- The black wall has the highest disagreement between simulation and experimental data in the cases evaluated. Non uniformity in optical properties and the possibility of a large specular component in reflection is seen as the primary factor responsible for this mismatch.

Despite the mismatch, nearly matching trend lines and an acceptable error percentage between measured and simulated results lying between 3 - 11 % prove the validation to be successful. In the next chapter, the model will hence be applied to the real case scenario of an office room.

3.4.5. Bifaciality gains

It is interesting to note the bifaciality gains, even though they may be inconsequential at such small scales of operation. From the side-wise PV power output results by LightTools, the front and rear PV power is calculated to determine the bifaciality gain as shown in Table 3.3. Note, this factor cannot be determined easily from the experimental setup since placing any measuring device like a pyranometer to check irradiance on module on the inside results in unwanted shading of the module itself. Bifaciality is calculated using Equation 3.1.

$$Bifacial\,Gain = \frac{Bifacial\,Power - Monofacial\,Power}{Monofacial\,Power} \times 100\,\% \tag{3.1}$$

Table 3.3: Bifaciality gains for validation cases

Case	Front PV (W)	Rear PV (W)	Bifaciality (%)
Reference	11.045	0.860	7.789
Furniture	11.048	0.882	7.987
White wall	11.124	1.533	13.778
Black wall	11.004	0.539	4.902

As anticipated from the discussion in the previous section, the bifacial gain of the furniture case is slightly higher than the reference. The white wall case gives the best bifacial gain due to reflection of high intensity short-path-length radiations back to the rear side of the curtain. For the black wall case, it is anticipated to have a slightly higher bifacial gain than the reference case. The error between simulation and experimental results due to inaccuracy in optical property inputs is held responsible for the unanticipated low gain.

4

Real-Scale Model

With the scaled down model successfully validated, this chapter focuses on applying the approach of the model to the real case scenario of a PV curtain in a room. Section 4.1 describes the system modelling approach taken for the base case, section 4.2 discusses the sensitivity of the developed model to variations in the environment along with the intrinsic assumptions in the model, followed by section 4.3 which briefly touches up on the life-cycle assessment of the PV curtain as a product.

4.1. Base case

As mentioned earlier, the office room LB02.490 at EEMCS faculty of TU Delft is chosen as the base case room for this final case study. This section discusses the irradiance model and load matching in the context of the base case.

4.1.1. Irradiance model

This subsection applies the methodology described in chapter 2 to the base case, starting from geometry preparation and up to the annual irradiance yield.

Geometry preparation

A room of dimensions 6.86 m long × 4.15 m wide × 3.23 m high is modelled in Rhino. For curtain curvature, the same assumptions as those in the validation case, are used. Figure 4.2 shows a wireframe perspective view of the office room modelled in Rhino (all dimensions in metres). More detailed dimensional data can be accessed in Appendix A. After modelling, the total area of the curtain is found to be approximately 9 square metres (not considering the area of the top and bottom 150 mm collars used for wiring). To have a 30 % integration of PV in the curtain, 2.7 square metres of the curtain must be occupied by PV. Assuming that the base 6 inch solar cell is cut along the two edge and central busbars, into pieces of width 62.4 mm (refer to Figure 4.1), this would amount to roughly 20 vertical stripes of PV, each 62.4 mm wide with 14 cut cells in one stripe. For convenience of modelling, the 14 cut-cells per vertical PV stripe are shown by three equivalent longer PV bands per vertical stripe. This results in a total of 60 PV surfaces on the front face of the curtain and another 60 on the rear face of the curtain.

Using the power value per mini module obtained in section 3.2.2 of 2.09 W, the installed capacity of the curtain module amounts to approximately 585 wattpeak (Wp) of bifacial installed capacity (or 538.44 Wp considering only front illumination). Although the room is modelled according to the office room in TU Delft, detailing of interiors of the room is kept minimal as it is not the primary focus of research in this work. Also, the effect of height of the room in the building and the impact of a non-free horizon due to nearby buildings in not considered in the current research.

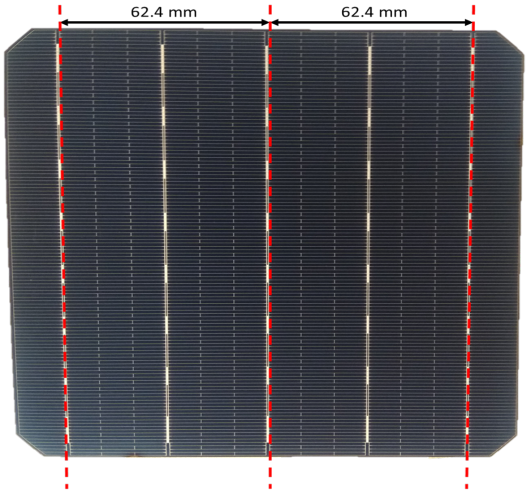

Figure 4.1: Bifacial solar cell with cut lines indicating new width of mini modules

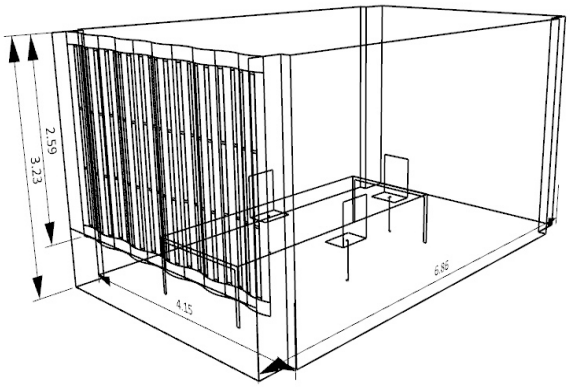

Figure 4.2: Wireframe perspective view of office room in Rhino

Optical properties

Once the 3D model is imported in LightTools, optical properties are assigned. Similar to the case of the validation model, all solids are modelled as surfaces and hence the optical properties must be carefully set. Since the validation model is a scaled down version of the office model, nearly all assumptions used in setting the optical properties for the reference case described in section 3.1 are applied for the office room model as well. The areas where assumptions differ from the ones in the validation model are listed as follows:

- Unlike the validation model which has a single glass window, the office room lies in a building with a double skin facade. This essentially means two facades separated by an air gap to allow ventilation and reduce the heating and cooling energy demand of the building. In this case, it involves two 3 mm glass facades separated by a 1 m air gap. This entire arrangement is to be replaced by a single surface in LightTools, for which Fresnel's equations are used. The conversion of the air-glass-air-glass-air arrangement to an equivalent air-glass-air arrangement is elaborated in Appendix B.1.1.
- The furniture in the base case of the office model is painted white, unlike the validation case where it is of a wooden texture. The paint is observed to match the wall color but differ in glossiness. Thus the same optical properties as that of the white wall are assumed with the exception of reflection behaviour as 'smooth optical' instead of 'simple diffuse'.

Defining the light sources

Two types of light sources have been used for simulations:

1. Natural light source: A light source similar to the validation model case is modelled to simulate the sun in LightTools, radiating 1000 W/m^2 of AM1.5 spectrum on the aim area. However, in this case, the source is placed directly above the window, 5000 m away instead of in front of it. The reason for this arrangement is that in the next step, the source has to be circulated to every point in the skydome and this is done using a macro that begins with the sun position at the zenith of the model.
2. Artificial Light Source: LightTools has an inbuilt library of artificial light sources from several popular lighting brands. Since the purpose of this thesis is to also analyze the effect of internal artificial lights on the performance of the bifacial system, the lighting in the office room LB02.490 is replicated for the corresponding simulation model by selecting the same lamps from the library, namely the Philips TL-D 58W 840 Super 80 MASTER. Note that the additional box type fluorescent light fixture in which the tube is mounted is ignored in this simulation. The positioning of the lamps in the model as per their position in the actual office in the LightTools modelling environment is shown in Figure 4.3.

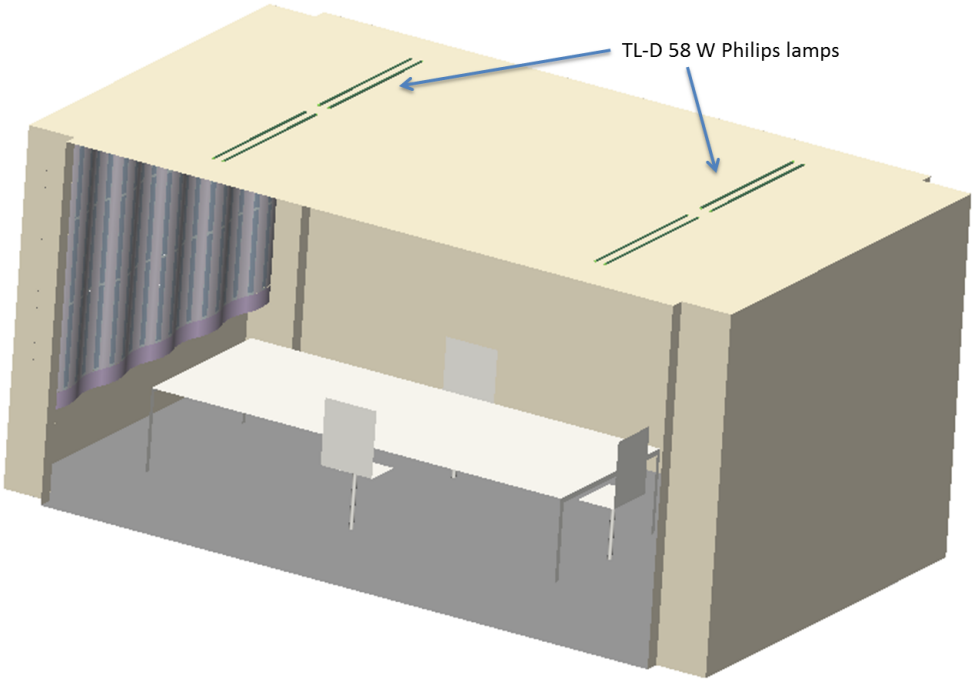

Figure 4.3: Office room in LightTools with artificial ceiling lights marked

Sensitivity simulations and sensitivity map

As explained in chapter 2, the aim of simulations is to circulate the sun source to every point in the skydome (using a macro function) and assess the sensitivity of the model to the sun's location. The sensitivity is processed in MATLAB into a sensitivity map which will be used later with the skymap for determining the true annual irradiance incident. The following approach is followed for running the simulations:

1. From the MATLAB scripts developed by Dr. Rudi Santbergen in TU Delft as cited in [46], the sky is meshed into several elements. The number of elements is decided by a number called the recursion level. Recursion levels of 3, 4 and 5 indicate 640, 2560 and 10240 sky elements respectively. To maintain a fair degree of accuracy and reasonable computation time for a complex geometry such as this case, a recursion level of 4 is selected. Using the same MATLAB script, a macro to move the sky source in LightTools to 2560 points across the skydome is generated.

2. Before beginning with the macro simulations, the model is calibrated according the approach in [68]. This is to find out how many rays are needed in the simulation to have good repeatability of results, irrespective of the seed in the forward-tracing Montecarlo approach. For calibration, the sun source is placed normal to the window like in the validation case since this is the most critical power generating arrangement of the source. With a standard deviation of 3 % and a simulation time of 7 seconds per simulation, a beam of 1 million rays is chosen as a good trade-off between computation time and simulation accuracy. The next most accurate option of 10 million rays gives a standard deviation of 1.5 % but with a simulation time of 1 minute 12 seconds per run. Between the two cases, the total simulation time to run a macro over 2560 sky points would take roughly 5 hours in the case of a million rays but 52 hours in case of 10 million rays which is why 1 million ray simulations are preferred.

3. An important observation made during pre-macro trial simulations is that the irradiance absorbed in the absence of artificial lights in the model is higher than that in the presence of lights. This is because, LightTools splits the total number of rays per simulation equally between the two light sources. Although the total power emitted is same in each case, the odds of striking the PV surface for the high power rays from the sun source are much lower in the presence of the artificial lights than in their absence due to smaller fan of rays being emitted from the sun source compared to the latter case. As a solution, the simulation is effectively run twice, for higher accuracy- first with the sun source alone (the

macro) and next with the artificial lights alone (single simulation). The results of power absorbed by PV due to indoor artificial lights are added in the end to the irradiance results obtained due to natural daylighting to obtain total irradiance on the PV curtain.

4. After running the macro, the results are imported in the MATLAB post-processing scripts. Here, the results of power absorbed by each of the PV surfaces for each of the 2560 positions of the sun source are converted into the sensitivity by dividing the PV power absorbed by the total power incident (1000 W/m^2) on the aim area. Thus a sensitivity map for each PV surface is generated.

Weather files and sky map

For the base case, as mentioned, Delft in the Netherlands is chosen for analysis. Hourly data for time of the year, sun altitude, sun azimuth, DNI and DHI for Delft [52.012°N, 4.357°E] for the year 2015 from the Meteonorm database [48] is used. While the direct light from the sun is located easily using the sun altitude and azimuth data, the diffuse light for every hour in the year from every element in the sky is determined using the Perez model, elaborated in detail in the thesis report of [46]. By combining the two, the skymap is constructed.

Annual irradiance and bifacial gain

The sensitivity map and skymap are combined to find the total irradiance incident on each PV surface. For the purpose of this report, three reference cases have been picked of 7 am, 11 am and 2 pm on the same day (30th June) to show how the sensitivity map and sky map at the time instant integrate to give the irradiance of the PV surfaces. Note, that these cases are most interesting since after noon, due to the orientation of the room towards the north-east, the curtain only receives diffuse irradiance. Figures 4.4 and 4.5 show the irradiances in the plane of array of the curtain at 11 am only. The comparison between the three cases can be located in Appendix E.1. For representation, only one surface (PV surface 1 on the top right corner) is chosen for plotting the sensitivity map. Note that every PV surface shown here is representative of roughly 4 to 5 cut PV cells that have been grouped together for ease of modelling.

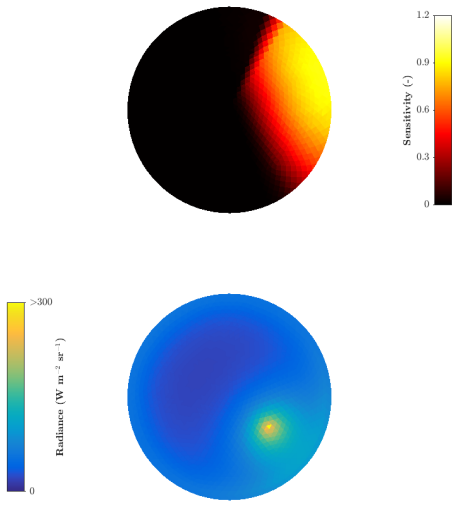

Figure 4.4: Sensitivity map (top) for a single PV surface and sky map (bottom) for 11 am on 30th June

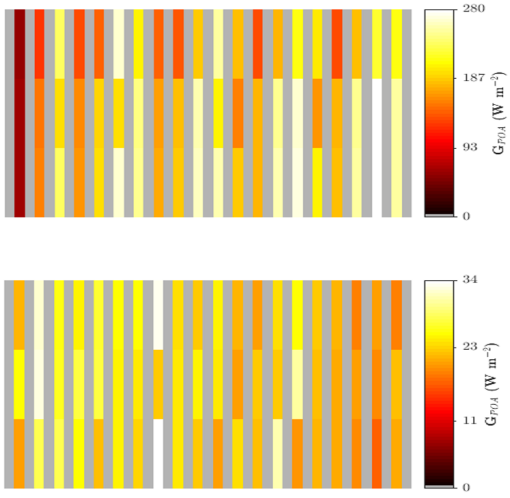

Figure 4.5: Irradiance on the front face (top) and rear face (bottom) of the PV curtain at 11 am on 30th June

The average of all front side PV irradiance in the plane of the PV surfaces in the curtain for every hour in the day, for every day in the year is shown in Figure 4.6. As anticipated, this shows a higher yield in the morning hours and lower yield in the afternoons due to the orientation of the northeast facing room.

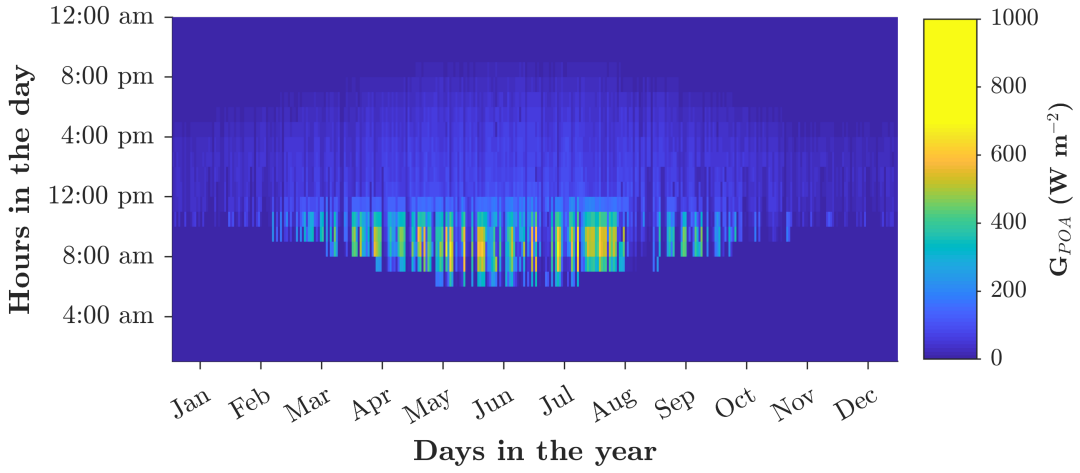

Figure 4.6: Average POA irradiance on the front face of the PV curtain in the office room

It is interesting to note the comparison between the irradiance on the curtain as compared to that on a module installed at the same location but at a more optimal tilt and azimuth. For this purpose, the online tool Photovoltaic Geographical Information System (PVGIS) by the European Commission, is used. Optimal tilt considered by the tool is found to be 40° at an optimal azimuth of 3° westward from the south . Plane of array beam and diffuse components are added to get total POA irradiance as shown in Figure 4.7.

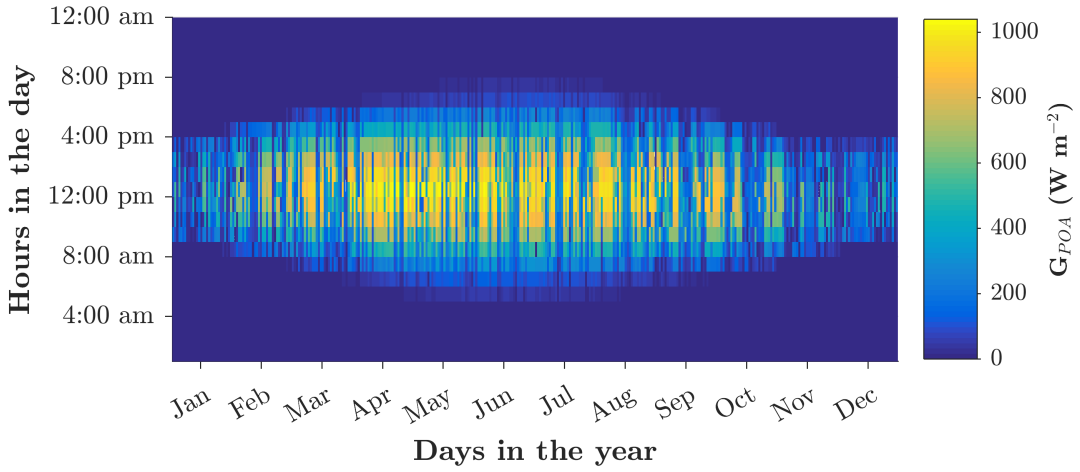

Figure 4.7: POA irradiance on a PV module at the optimal tilt and azimuth at same location

From the two figures, the difference in irradiance received by the curtain module due to non-optimal tilt and azimuth, is clearly seen. Variations in irradiance due to slight folds in the curtain also contribute to the lower average irradiance on the curtain's POA compared to that of a module installed at optimal tilt. The contour plot of plane of array irradiance for a module installed at the same tilt (vertical, taken as constraint since the window is vertical) but at a more optimal azimuth, at the reference location, can be found in Appendix E.2.

Using the same mini module efficiency figures for front and rear faces of 19.66 % and 13.21 % respectively from section 3.2.2 of chapter 3, annual bifacial gain of such a system is found to be 8.64 %.

Table 4.1: Annual bifacial gain of base case- office room

Case	Front PV (kWh)	Rear PV (kWh)	Annual DC yield (kWh)	Bifaciality (%)
Office Room	173.46	14.99	188.45	8.64

Without the 10 hours of indoor artificial lights, the annual PV power reduces to 185.95 kWh. The rear side PV power was seen to drop to 12.85 kWh annually and the bifacial gain was seen to reduce to 6.91 %. Thus the artificial lights were seen to make a contribution of just about 1.33 % to the annual PV energy yield.

4.1.2. Application matching: electrical model

This section applies the electrical model with load cases from chapter 2 to the base case office room. Although detailed electrical modelling is not within the scope of this thesis, a type of series-parallel configuration for the curtain module is proposed in subsection 4.1.2. The yield obtained from subsection 4.1.1 is matched with the load cases prepared for an office room as well as for a household room to observe the effect of change in time of energy use.

Module configuration

From the PV characterization conducted using the neonsee solar simulator in section 3.2.2, it is known that each laminated 31.2 mm × 156.75 mm cut-cell produces roughly 1.075 W (0.955 W front (1 sun) + 0.120 rear (0.2 sun)) of DC power. A maximum voltage of 0.523 V and maximum current of 2.071 A (1.827 A front (1 sun) + 0.244 A rear (0.2 sun)) is expected. Thus if all 280 cut cells of double the width (hence double the current) in the curtain are connected in series like the validation model, it would result in a module of 4.142 A and 146.44 V. Having an open curtain of such high voltage in close proximity to humans is not advisable. However, a parallel connected module leads to an increase in current, causing more significant cable losses. As a trade of, it is proposed that every set of 5 stripes must be connected in series amounting to a 36.6 V 4.142 A block. 4 such blocks connected in parallel yield an equivalent system of 36.6 V 16.56 A. This restricts the voltage to a relatively safe level. The layout of the configuration can be seen in Figure 4.8. With a total DC cable length of 12.185 m, using ohm's law, the cable losses are calculated to be 5.75 % for 12 AWG copper cables (diameter: 2.05 mm). This loss is factored in while calculated DC power available for meeting the loads. Losses in the laminated tabbing between cut-cells in the tabbing wire have been neglected in this analysis. Also, the use of flexible coiled cables such as those shown in Figure 4.9 is proposed for easy opening and closing of the curtain. The insulated stranded cables ensure safety against any fire hazard by sufficiently encapsulating all current carrying components.

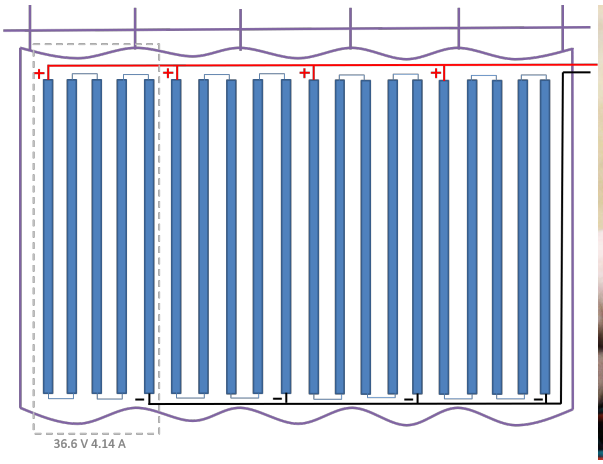

Figure 4.8: Series-parallel configuration of the curtain module: 36.6 V 16.56 A

Figure 4.9: Coiled cables proposed for curtain connections [75]

Scenario 1: Curtain in office room

Using the load profile for the office scenario described in chapter 2, a load combination of 3 laptop charges, 2 mobile charges and curtain automation is considered. Figure 4.10 shows the PV power for every hour in the year compared with the load required to be met at that particular time instant. An LOLP plot for this data is constructed, based on the Li-ion 11.1 V 4.4 Ah standard battery. Of all Lithium ion battery specifications, the said one is chosen for its light weight (0.3 kg per battery), making it more suitable for mounting near

the indoor curtain. Note, this plot of LOLP is constructed with a 60 % DOD cycle for the battery bank. The LOLP plot in Figure 4.11, shows that in the absence of a battery, for 24.36 % of the time, load is not met. However, increasing the battery bank size beyond the knee point of this LOLP plot only results in marginal improvements in LOLP at a much higher cost and weight of the battery. Thus, a point close to the knee of the graph at three batteries (totally < 1 kg) is considered optimum, resulting in an LOLP of 5.18%, typically during the months of December and January as shown by the SOC plot (Figure 4.12) in green. Also the amount that has to be dumped during the summer months is visible in the plot.

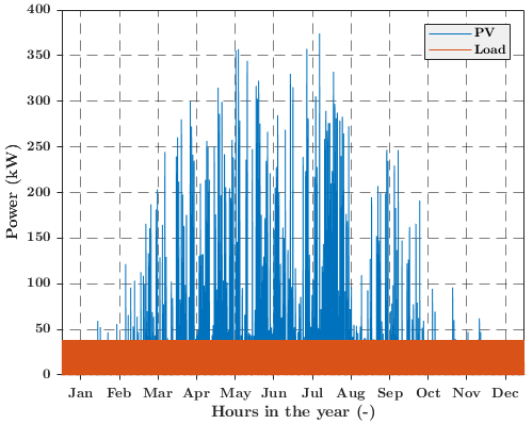

Figure 4.10: Load power and PV power for each hour in the year

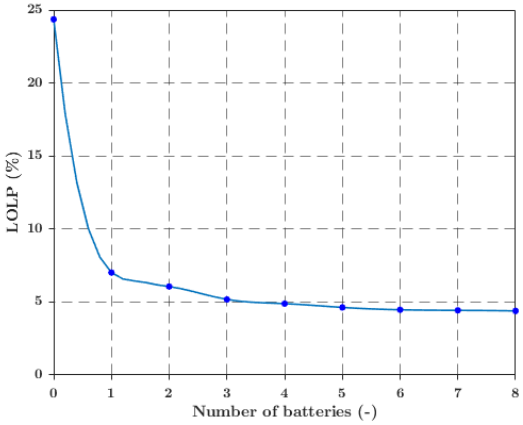

Figure 4.11: Loss of load probability for 0 to 8 Li ion batteries of 11.1 V 4.4 Ah each

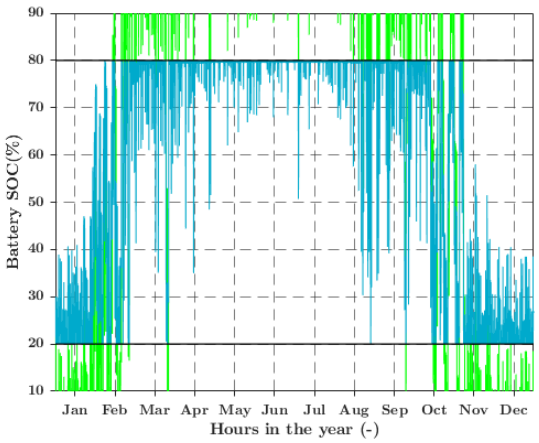

Figure 4.12: State of charge variations across the year for a 3-battery system between 20 % and 80 % DOD (blue) and between 0 % and 100 % DOD (green)

Similar MATLAB simulations are run to find the LOLP for the case with 80 % DOD and the results are tabulated in Table 4.2. The dump shown in the last column is a concept similar to LOLP but indicates the amount of PV power wasted due to absence of enough loads in the summer.

Table 4.2: Comparison between 60 % and 80 % DOD battery cycling for the 11.1 V 4.4Ah three-battery system

DOD (%)	LOLP (%)	Dump (%)
60	5.18	0.01
80	4.89	0.01

By meeting all loads for 95 % of the time in the year, the model can be said to perform well, despite the

non-optimal tilt and azimuth of this unique PV module. Since the area of the window and room orientation is a inevitable limitation, this translates directly to a limit on the output PV power.

Scenario 2: Curtain in residential room

Although the base case considered is an office room, to see a better variation in results due to seasonal loads (like fairy lamps in households), the load case if the base room was used in a home instead of an office is considered. However, for simplicity in PV yield calculation, influence of indoor lighting on bifacial PV yield is considered only from 19.00 hours to 23.00 hours without any seasonal variations. As per the load case described in chapter 2, a load profile of 2 laptop charges, 2 mobile charges, curtain automation and 1 to 5 hours of LED lighting, depending on the season, is considered. Figure 4.13 shows the PV power for every hour in the year compared with the load required to be met at that particular time instant. An LOLP plot for this data is constructed, based on the Li-ion 11.1 V 4.4 Ah standard battery (60 % DOD cycling) like in the office room case. The LOLP plot in Figure 4.14, shows that in the absence of a battery, for 26.46 % of the time, load is not met. Increasing the battery bank size results in a steady drop in LOLP until the knee point, beyond which only marginal improvements in LOLP are achieved but at a much higher cost and weight of the battery. Thus, a point close to the knee of the graph at six batteries (totally < 2 kg) is considered optimum, resulting in an LOLP of 8.05 %, typically during the months of December and January as shown by the SOC plot (Figure 4.15) in green.

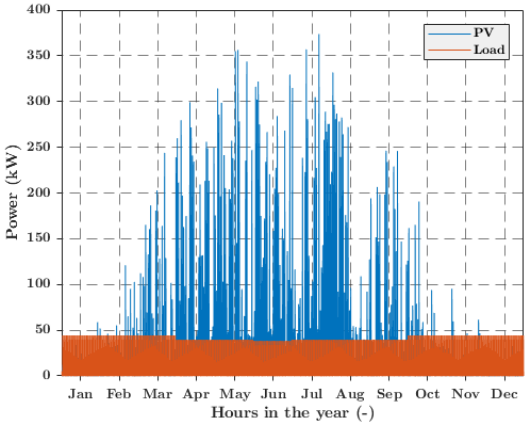

Figure 4.13: Load power and PV power for each hour in the year

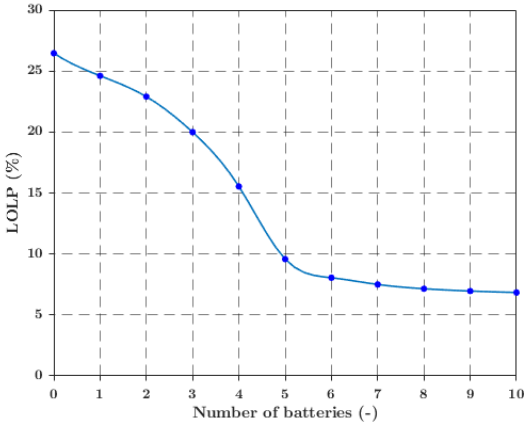

Figure 4.14: Loss of load probability for 0 to 10 Li ion batteries of 11.1 V 4.4 Ah each

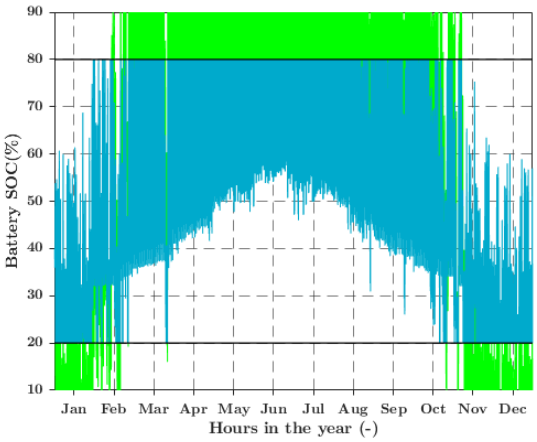

Figure 4.15: State of charge variations across the year for a 6-battery system between 20 % and 80 % DOD (blue) and between 0 % and 100 % DOD (green)

MATLAB simulations are also run to find the LOLP for the case with 80 % DOD and the results are tabulated in Table 4.3.

Table 4.3: Comparison between 60 % and 80 % DOD battery cycling for the 11.1 V 4.4 Ah six-battery system

DOD (%)	LOLP (%)	Dump (%)
60	8.05	0.01
80	7.15	0.01

The PV curtain, in a household, is seen to meet the DC loads designed for 92 % of the time with a battery bank of 6 Li-ion 48.84 Wh batteries. Since none of the DC loads considered here are critical, this system can be considered as one that supplies typical DC loads in households for 92 % of the year on clean energy.

4.2. Sensitivity analysis

The base case considered in the previous section, analyses yield characteristics for a very specific room. However, it is important to analyze the sensitivity of this yield to different parameters in the room that may help enhance its performance in an alternate setting. This section looks at various sensitivities in the model such as sensitivity to orientation of the room, location in the world, depth of the room and the percentage of PV integration.

4.2.1. Orientation of room

The room considered in the base case study faces the north east. Being situated in the Netherlands which lies in the northern hemisphere, the location could be considered quite unsuitable for PV. However, this room has been intentionally chosen to observe what loads could be met, even with a sub-optimal orientation. Figure 4.16 shows how a change in the orientation of the room, more towards the south could favorably assist in meeting more loads due to the higher PV power generated.

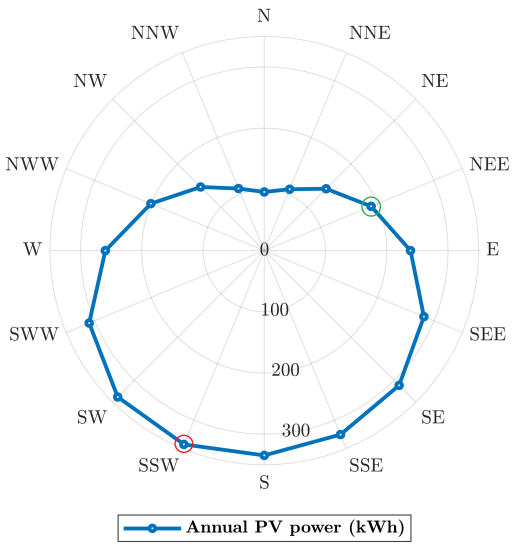

Figure 4.16: Variation in total annual PV power (kWh) for different orientations of room- current orientation in green and the best orientation in red

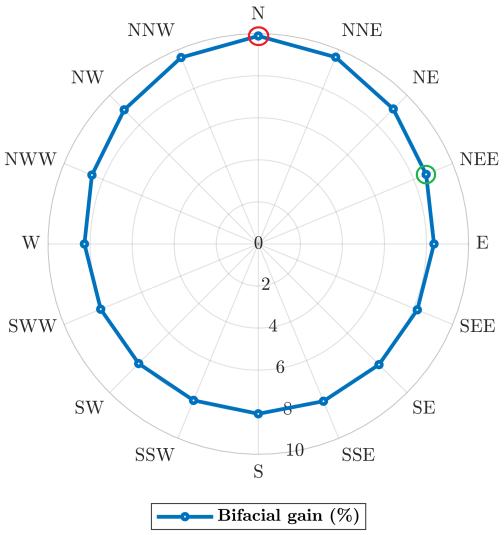

Figure 4.17: Variation in bifacial gain (%) for different orientations of room- current orientation in green and the best bifacial gain orientation in red

As is seen in the figure, a change in the azimuth of the room to 202.5° (where 180° is south) as compared to the original 67.3° causes an increase in annual power yield from 188.45 kWh to 342.67 kWh. This is an important criteria for determining which type of room and what kind of loads can be met using the PV curtain. Figure 4.17 also shows how bifacial gain changes with orientation. Exactly contrasting to the previous figure, this plot

shows a maximum bifacial gain of 9.88 % for a room pointing north. This shows the relatively low dependence of indoor radiation impinging on the PV, on outdoor solar radiation. Since the indoor effects remain nearly constant across different orientations, the bifacial gain is felt more in the north facing orientation, despite a lower annual PV yield.

4.2.2. Location in the world

Different places in the world see different equivalent sunshine hours and different sky paths compared to the ones seen by the base case office room. To see how the PV power output changes with location in the world, a set of 13 different cities across the world at varying latitudes and longitudes are considered. These are marked in Figure 4.18.

Figure 4.18: Cities considered in this study, marked on the world map

The table below shows key parameters about each location considered such as latitude, longitude and insolation (kWh/m^2) per day for a average day in June and December respectively.

Table 4.4: Summary of cities with their code as shown in the Figure 4.19 with their winter and summer insolation [59]

City	Code	Latitude	Longitude	Insolation (kWh/m^2/day)	
				Jun	Dec
Berlin	A	52.517	13.389	4.77	0.48
Buenos Aires	B	-34.67	-58.5	2.06	6.78
Auckland	C	-36.92	174.6	2.06	6.51
Miami	D	25.817	-80.283	6.17	3.28
Vancouver	E	49.24	-123	5.53	0.86
New Delhi	F	28.62	77.22	6.34	3.31
Beijing	G	39.93	116.4	6.00	2.21
Dubai	H	25.23	55.28	7.40	3.67
Cape Town	I	-33.93	18.47	2.50	7.96
Bogota	J	4.63	-74.08	4.62	4.48
Rotterdam	K	51.92	4.48	5.53	0.49
Madrid	L	40.417	-3.704	6.75	1.51
San Fransisco	M	37.617	-122.367	7.72	1.85

Figure 4.19 below shows change in PV power output with location. As is intuitive, since the room faces the north east, cities located in the southern hemisphere such as Buenos Aires, Auckland and Cape Town perform much better compared to the rest. Next come cities located in the northern hemisphere but those that lie relatively closer to the equator such as Miami, New Delhi, Dubai, Bogota, Madrid and San Francisco. Since these cities lie in the tropical and sub tropical belts, they see high irradiance nearly all year round with very few seasonal variations resulting in a higher annual PV yield. Finally, the locations in the temperate zones such as Berlin, Vancouver, Beijing and Rotterdam show the lowest PV performance due to a non-ideal azimuth. Figure 4.20 shows the annual solar radiations received by each location. Confirming the previous hypothesis, the graph shows that despite receiving nearly equal annual irradiation, the PV curtain in the base case room performs better in Capetown than New Delhi and Dubai due to a more favorable azimuth. Thus, to get the most power output from the same system, careful consideration of window position for the given location is advised. Nevertheless, it is also important to see how despite a non-optimal azimuth, most DC loads in the room can be met >90 % of the year.

Figure 4.19: Annual power output of PV curtain in cities across the world

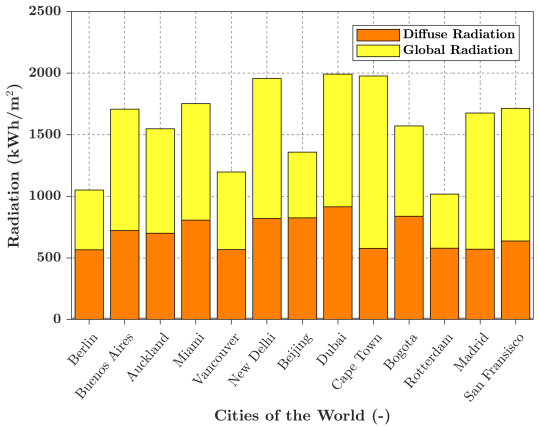

Figure 4.20: Annual radiation profile in terms of DHI and GHI at the location based on data from [48]

Figure 4.21 shows bifacial gain for power produced by the PV curtain across different cities.

Figure 4.21: Comparison of bifacial gain between different cities in the world

Interestingly, it is observed that the higher latitude cities performing worst in the PV power generation such as Berlin, give the highest bifacial gain of 8.52 %. This can be explained by the fact that since the annual radiation incident from outside is not high enough as compared to the tropical cities, the indoor artificial lighting as well as reflected light makes a more significant contribution to annual power output than tropical cities and those located in the southern hemisphere at more favorable altitudes. The graph also shows how the effect of indoor lighting and reflected light remains nearly the same for all cases, irrespective of location.

For this reason, it can be seen that Capetown, that gave the best results for PV power, has the lowest bifacial gain since the outdoor radiations the curtain sees are far higher than nearly constant indoor radiations seen by the PV.

4.2.3. Depth of room

To assess the impact of depth of room on PV curtain performance, a second room similar to the base case room is designed, but only of half the depth (3.43 m instead of 6.86 m) is prepared and the same procedure of irradiance modelling is run on the new half sized model. The results can be seen in Table 4.5, while the model can be visualised in Appendix E.3.

Table 4.5: Annual bifacial gain of base case- office room

Case	Front PV (kWh)	Rear PV (kWh)	Bifaciality (%)
Base-case room	173.46	14.99	8.64
Half-depth room	174.04	18.45	10.60

A shorter room is seen to give a better bifacial performance of 10.6 % due to a greater reflection of high intensity radiations from the back wall, now closer to the window than in the original case. This is much like the case investigated in the validation model, where an intermediate white wall, placed at 30 % the original room depth led to an enhancement of the total PV yield from the room. With a total annual PV yield of 192.49 kWh compared to the original case of 188.45 kWh, a pure gain of 4.04 kWh (2.1 %) can be achieved per year. Thus, a shorter room is seen to have a direct influence on the PV yield of the system.

4.2.4. Percentage of PV integration

Analyzing the influence of PV integration is of much interest for observing its effect on the bifacial gain. While reducing the PV can result in better rear side yield at the cost of lower overall yield, increasing the PV can result in reduced rear side yield but higher net yield. Two cases of 15 % PV integration and 60 % PV integration were simulated (models can be visualized in Appendix E.3). While the first case was simply modelled in Rhino, by taking off half the PV strips from the base case model, for the latter, a new curtain with 27 stripes of 93.6 mm wide PV cut cells instead of the initial 62.4 mm, was modelled. The results can be viewed in Figure 4.22.

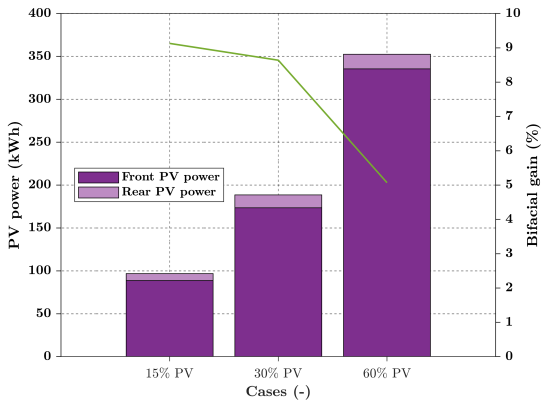

Figure 4.22: Comparison between PV curtain with 15 %, 30 % and 60 % PV with bifacial gain in green

As is observed from the graphs, a room with a lower percentage of PV, despite a higher bifacial gain of 9.13 %, only yields 96.8 kWh of energy per year. In the second case (base case), a 30 % PV integration, already yields nearly double the quantity of PV power by generating 188.45 kWh annually, albeit at a decent bifacial gain of 8.64 %. Finally the third case with 60 % integration of PV yields energy in the order of 352.5 kWh but only with a 5.07 % bifacial gain. Despite the low bifacial gain, the amount of rear side PV generated in case 3 is higher than both case 1 and case 2 due to the higher amount of surfaces available for active capture of the irradiance.

Although the case with 60 % integration gives the highest yield, it may not be considered very aesthetically appealing since now it covers more than half the curtain, not making it semi transparent any more. Under such conditions, it is more likely to be drawn open for most of the day, which in turn will take effective energy generating hours out from the curtain's annual production, perhaps making it just as good as case 2 in terms of annual energy generation.

4.3. Energy pay back time

Due to its tag of being a clean technology and due to rapidly falling prices due to mass manufacture in places like China, the market for PV is rapidly growing. This trend has expanded from commercial and utility PV systems to several niche products that integrate PV as well such as solar boats, solar cars, solar windows and, as explored in the current research, solar curtains. However, it important to analyze, especially in case of niche products, if the product truly performs as a clean technology by generating more energy in its lifetime than the amount of energy spent in manufacturing it. Energy Pay Back Time (EPBT) is a very commonly used parameter in assessment of (environmental) impact performance of different technologies and will be applied to the context of the PV curtain in this section.

Assumptions

Since life cycle assessment is not the prime focus of this research, a couple of assumptions are made for simplicity. These are listed below:

1. The EPBT calculated in this section is more of a comparison with the current situation of a non-solar curtain. Thus, every new component in the curtain module, excluding the cloth, has been taken into account for the analysis.
2. A 2006 study on embodied energy in photovoltaic systems [76] is consulted for assumptions on energy consumption for silicon purification and processing and for cell fabrication. Most of these values are in kWh/m^2. However, it must be noted that silicon consumption per cell has steadily been reducing. Literature states that the use of bifacial can reduce lifecycle CO_2 emissions by 38 % [77]. Use of PERC cells too has been cited to result in a reduction in EPBT compared to conventional solar cells [78] . This has not been factored in, in this study, due to the lack of availability of more recent open data.
3. Assuming fiber laser cutting of silicon cells, a cut speed of 200 mm/s and electricity consumption of 1.5 kW is assumed from supplier's datasheet [79].
4. For tabbing, lamination and testing, an IEA 2011 report [80] is consulted. For tabbing, the study assumes an electricity consumption of 0.0191 kWh per cell of area 125 mm × 125 mm. Since this is double the size of one cut-cell used in this thesis, for 280 cut-cells in the curtain module, an energy requirement of 2.674 kWh will arise. For lamination 9.95 kWh per 1.25 m^2 of module area is considered. Since the total solar laminated area in the curtain module is 3.13 m^2 (width of PV strip (0.0624 m cell width + 0.006 m clearance for plastic foil) × 2.29 m PV strip length × 20 strips), the energy needed will be 17.4 kWh. Testing is assumed to be 0.01 kWh per 1.25 m^2 of module area.
5. According to a 2012 study [81], cumulative energy consumed by Li-ion batteries was approximately 88-90 MJ/kg. Since the system proposed here involves using a 3 battery bank system weighing totally 0.9 kg, embodied energy of 22.5 kWh is considered.
6. An extra 5 % is assumed for power electronics (such as an off-grid power converter) and cabling involved.
7. Replacement of battery bank in 5 years is neglected in this analysis.

All these assumptions are tabulated in Table 4.6. The average life of a curtain is said to be 10 years [82]. With a pay back period of 12.3 years (as seen in the table), the curtain consumes more energy than it is able to deliver in its lifetime. However, this can change over the next decade with developments in recycling strategies, resulting in lower material and energy consumption, especially in the most energy intensive part of this curtain, which is silicon processing and purification. Until then, it would be most advisable to deploy such a curtain only in south oriented rooms, which would result in a payback of roughly 6.6 years or in another

location in the world, at optimal azimuth such as Cape Town with the current base room orientation for a 4.4 year pay back period.

Table 4.6: EPBT assessment for PV curtain by summing embodied energy of all PV system components

Parameter	Energy Consumed (kWh)	Source and comment
Silicon processing	1826.92	666 kWh/m^2 [76]
Cell fabrication	329.18	120 kWh/m^2 [76]
Laser-cutting	0.17	1.5 kW Fiber laser cutting at 200 mm/s [79]
Tabbing/stringing	2.67	0.0191 kWh per cell of 125 mm × 125 mm [80]
Lamination	17.40	6.95 kWh per 1.25 m^2 module area [80]
Testing	0.02	0.01 kWh per 1.25 m^2 module area [80]
Battery	22.5	90 MJ/kg [81]
Power electronics, cabling	109.94	Assuming 5% of total for power electronics like MPPT and miscellaneous items like cabling
Total	2308.81	
EPBT	**12.25 years**	

4.4. Conclusions

After validating the LightTools simulation approach in chapter 3, it was applied to a real case study of the Master thesis office room in TU Delft. The results from the simulation yielded a total PV power output of 188.45 kWh for a curtain module of a roughly 585 Wp installed capacity. It must be noted here, that although by manufacturer's specifications, the base solar cell is rated at 5.16 Wp, in testing, it is never attained. Thus the tested maximum wattpeak of the mini module of 2.09 W is taken as the installed DC power per cut cell, leading to a total bifacial installed capacity of 585 Wp or 538.44 Wp (considering only front illumination). This makes the system a 323 kWh/kWp curtain module. Matching it to the load cases showed that while the system was able to meet most of the DC loads described for the office room, for 95 % of the year with a relatively small power bank, the situation is quite different when concerning a household. This is because, in a residential scenario, most load cases lie outside the sunshine hours of the curtain. Thus the battery bank designed must be of a much higher capacity to store all the energy generated during the day for consumption at night.

Next, the sensitivity of the model to different orientations was assessed and it was found that a similar room oriented to the south west could yield nearly double the PV power as the current room. Also, the sensitivity of the model to location (with the current orientation) resulted in a higher yield in cities in the southern hemisphere since the room faces the north east or low latitudes due to the better average insolation they see throughout the year. Room depth also turned out to play a significant role in PV power output, giving a nearly 2 % improvement in both bifacial gain and annual PV power output for the same room of half the depth. It was also concluded, by varying the percentage of PV in the curtain, that although 60 % PV gives a much higher (nearly double) annual PV yield compared to the base case with 30 % PV integration, it may not be the best option, considering that the curtain will not classify as semi-transparent anymore due to 60 % PV coverage. As a result, it will be opened frequently, resulting in loss of effective energy generating hours and a dip in annual energy produced by the system.

Finally, the EPBT for the solar curtain in question was calculated, giving a energy payback time of 12.25 years. The importance of this calculation not only in the context of the PV curtain, but also for any new niche application integrating PV in the environment was highlighted.

5

Conclusions and Recommendations

The need to rapidly transition nZEB buildings has led to a growing focus on BIPV and BAPV. Designing a solution that allows even existing and monumental buildings to be 'solarized', without needing any renovation, has been a motivation for the research on PV curtains presented in this report. To this effect, a research objective of assessing- through modelling and simulation- the energy potential of a bifacial PV curtain that is able to harness energy from indoor lighting as well as outdoor radiations, with a special focus on its bifacial gain, was set. To achieve this, the tasks and objectives laid down in section 1.5 have been met. The key findings of this report have been listed in section 5.1, followed by recommendations for future work in section 5.3. Some important practical learnings alongside the primary research are also presented in Appendix F.

5.1. Key findings

To effectively assess the power yield of a PV curtain in a room, a methodical approach of modelling, simulation, validation and application was used. First a mock-up of a room with the PV curtain was modelled and then simulated with a light source to assess PV yield. The model was validated using an experimental setup and after validation, applied to a real case of an office room. The key findings in the two major focus points of this work- validation of model and its application to a case study- are elaborated in sections 5.1.1 and 5.1.2 respectively.

5.1.1. Validation

The validation model involved simulating a scaled down version of the PV curtain in an office room and comparing it with experimental results from a similar design. The key findings here are listed as follows:

1. Characterization of PV cells showed a higher efficiency for the mini modules, compared to the non-laminated base full cell. This was attributed to several causes, first being optical coupling, that leads to an enhancement in anti-reflective properties of the cell due to encapsulation using a material of refractive index between air and crystalline silicon. The second reason could be poorer contact between the cell in tabbing wire in case of the non-laminated base cell, compared to the laminated mini module. Although a reduction in performance due to the cut was anticipated, the reverse was seen. This seems logical when one sees that the current carried by the mini module is much lower than the current carried by the full cell. Thus ohmic losses across resistances are elevated in case of the full cell, but much smaller for the mini module. A final trial of IV curve measurement using an elevated platform and a black reflector and then a white reflector on the floor of the platform revealed that despite the color, most black surfaces are not perfect absorbers. Even low reflection coefficients for the black reflectors (5 %) were found to result in a slightly better performance than a case having no reflectors on the rear side. This was proved to be correct since it resonated exactly with the validation model experimental cases which showed that the case of the black wall yielded a better response experiementally, than the case with no intermediate walls.

2. With an error margin ranging from 3 % to 11 %, between the software simulation and experimental results, the modelling approach was successfully validated. A marginally lower irradiance seen by the reference cell in these measurements is considered responsible for an overestimation of experimental results. Other sources of error could be inaccurate representation of optical properties in the simulation model such as use of outdated coefficients for room walls and non-uniformity of optical properties assumed for cloth, the furniture, the white and black walls. The absence of values on angular reflectance of the various facets of the curtain and slight uncertainties due to batch variations in calculating efficiencies of the mini modules are other factors to be considered.

3. The trend showed a slightly higher power output for the case of furniture as compared to the base case. The white-wall case performed best by reflecting maximum incoming irradiance back on to the cell. The black wall case too performed better, experimentally, than anticipated, showing that the little reflection of incoming irradiance from its surface onto the PV was still slightly more significant than the reflection from the distant rear wall. The simulation model however predicted a slightly lower yield for the black wall case due to an underestimation of reflection in material property assumptions.

4. In terms of bifaciality, the simulations yielded a result of 7.7% gain for the reference case, 7.9% for the furniture case, 13.778% for the white wall case and 4.9% for the black wall case. Since the error margin for the black wall case is highest, it is treated with a certain level of uncertainty. Nevertheless the trend showed that a shorter room of highly reflecting walls can result in an improvement in power output and bifacial gain compared to the base case.

5. According to the standard IEC 600904-1-2, which is still under development, one approach considered for measurement of bifacial modules is front illumination of an irradiance higher than 1 sun such that it factors in the bifaciality and a condition of 0.2 suns illuminating the rear face. Since the light source during characterization could not be increased beyond 1000 W/m^2 at AM1.5, the rear face was instead analyzed through single side illumination at 0.2 suns and the results were added to arrive at the equivalent power of 2.09 W per mini module. These assumptions were then used to convert incident irradiation from the ray-tracing into PV power, for the simulation of the validation model prepared. Since the model is said to be valid, the assumption here also can be treated as also valid.

5.1.2. Case study: Office room

By applying the optical model validated by experimental setup for the real case of an office room in TU Delft, useful insights were gained. These are listed below:

1. For a location in the northern hemisphere, to maximize PV power output, a south facing orientation of the PV is recommended. Despite considering a north-east facing room as the base case, a decent annual power output of 188.45 kWh or 323 kWh/kWp was achieved. A bifacial gain of 8.64 % was obtained. The contribution of 3650 hours of artificial lighting throughout the year were only seen to have a 1.33 % impact on the PV power output of this curtain.

2. With an assumption that the curtain remains closed throughout the day (due to the fact that the cloth in the curtain is semi-transparent and only blocks glare from the room), a moderate DC load profile drawn for an office case scenario of 3 laptop charges and 2 mobile charges was met for 95 % of the time in a year with a storage capacity comprising 3 Li-ion batteries of 11 V 4.4 Ah each.

3. A second DC load profile of a residential room, drawn out to assess the performance of the system when hours of consumption are different from hours of generation (unlike the office case), showed that the system could now meet loads (2 laptop charges, 2 mobile charges and seasonal fairy lights (LEDs)) for 92 % of the time. The system also required a fairly larger storage capacity of 6 Li ion batteries of 11 V 4.4 Ah each. The effect of time of use of electricity on the system design was evident from this analysis.

4. Testing the model for sensitivity to orientation revealed that a direction with a room azimuth of 202.5° gave nearly double the annual PV power at 342.67 kWh compared to the base case of 173.46 kWh. Due to the south facing orientation, the curtain in such an orientation would see naturally more sunshine hours resulting in the higher PV output. On the contrary, the bifacial gain was seen to be lowest for this orientation and highest for a room oriented to the North. This shows that the effect of the indoor reflected (diffuse) light and artificial lighting remains nearly constant across all orientations resulting in a

higher bifacial gain for situations where front illumination is low and a lower bifacial gain for conditions where the front illumination is high.

5. When the model created was assessed for sensitivity to different locations in the world, it was found that the highest yield was associated with locations in the southern hemisphere receiving high average annual insolation such as Capetown. An intermediate yield was achieved for tropical locations in the northern hemisphere and lowest for locations located in the temperate zones of the northern hemisphere such as Berlin and Vancouver. This again established sensitivity of the model to hours of radiation received daily and optimal azimuth and tilt of the module, which are different for different locations across the world.

6. The model was seen to be partly sensitive to the depth of the room as well, giving a 2 % improvement in bifacial gain as compared to the validation model that considered a similar case but achieved a 6 % improvement in bifacial gain. This can be explained by the fact that the former considers annual power output. During annual simulations, the bifacial yield keeps changing per hour depending on the level of outdoor irradiance and the net result is based on the sum of front and rear irradiances absorbed which comprises a mix of days with high outdoor irradiance (low bifaciality) and low outdoor irradiance (high bifaciality). The case of the validation model only considers results for one setting (STC) of outdoor irradiance. This explains why the results of the full room case may not be as high as those from the validation. Another reason could be the fact that the wall is placed at half the room depth in the validation model but less than half the room depth in the case of the office room model. Also, the validation model has the entire window side facade made of glass, unlike the room model.

7. Finally, assessing the model for sensitivity to percentage of PV in the curtain revealed, intuitively, that between 15 %, 30 % and 60 % PV integration, the annual yield increases from lowest percent of integration to highest percent while bifacial gain reduced in the same order of cases. Despite highest yield for the 60 % PV integration case, the report still recommends the 30 % integration case for implementation. It is speculated that the loss of translucency due to higher PV integration would eventually result in more frequent opening of the curtain, thus reducing the effective sunshine hours seen by curtain and have a direct impact on power yield.

8. A rough energy pay-back analysis revealed that the curtain takes 12.25 years to pay back the energy that it consumes in its manufacture, compared to a regular curtain. Knowing that a curtain has a lifetime of barely 10 years, having a PV curtain for the room under consideration would not be useful. Instead, installing the curtain in a location with higher receptivity to the current orientation, such as Cape Town can result in an energy pay-back of roughly 4 years, which is reasonable.

5.2. Concluding remarks

In the current research, the concept of PV curtains for buildings to harness solar energy without needing any renovation, was explored. For locations in the northern hemisphere, especially those in the temperate climate zone like Delft in the Netherlands, a bifacial curtain can significantly raise the PV yield by 8-9 %. Over all, a bifacial curtain makes most sense for a short room with a non-optimal azimuth in a location that receives lower sunshine hours. However, to ensure that the curtain is able to recover more than the energy expended in its manufacture, a better orientation such as south-south-west (for a room in Delft) is advisable. Even in this condition, a significant bifacial gain of nearly 8 % can be achieved. Thus, the current research recommends a bifacial curtain over a monofacial. The current findings must be however, supplemented by the recommendation covered in the next section to make the case most complete.

5.3. Recommendations

A number of recommendations are proposed for future work:

1. As mentioned earlier, this thesis did not lay much focus on electrical modelling of the curtain. Thus preparation of an optimum electrical model with the most suitable configuration, depending on the choice of power converters is advised.

2. Due to the absence of an electrical model, the impact of shade on the PV power output could not be accurately represented in this research. Thus all scopes of shade were nearly eliminated by having a very low curvature for the curtain profile and neglecting completely the effect of a crowded horizon. For future work, once the detailed electrical model is coupled with the optical model, the sensitivity of the curtain to a crowded horizon as well as highly curved cloth inter-layers, must be explored.
3. Incorporating a level of calculation for the sensitivity of the model to opening and closing frequency for the curtain is another topic of much importance in accurately determining the power yield of the curtain.
4. Adding a segment for thermal modelling can expand the utility of this model to locations where the room in hotter locations without any air-conditioning.
5. In the event of implementing the curtain in a real room, special care for ensuring insulation of all live wires is imperative to protect it from any fire hazard. this must be given focus in future work.
6. Assessing the sensitivity of the model for the bifacial component, to the color of the paint and indoor complexity can be useful for making the model complete.

Bibliography

[1] IEA(2019), "Global energy demand rose by 2.3 % in 2018, its fastest pace in the last decade." [Online]. Available: www.iea.org/newsroom/news/2019/march/global-energy-demand-rose-by-23-in-2018-its-fastest-pace-in-the-last-decade.html

[2] IEA(2019), "Perspectives for the Clean Energy Transition," Tech. Rep., 2019. [Online]. Available: www.iea.org/publications/reports/PerspectivesfortheCleanEnergyTransition/

[3] IEA(2013), "Transition to Sustainable Buildings: Strategies and Opportunities to 2050," Tech. Rep., 2013.

[4] D. Chwieduk, *Solar energy in buildings: thermal balance for efficient heating and cooling*. Elsevier, 2014.

[5] E. Biyik, M. Araz, A. Hepbasli, M. Shahrestani, R. Yao, L. Shao, E. Essah, A. C. Oliveira, T. Del Cano, E. Rico *et al.*, "A key review of building integrated photovoltaic (bipv) systems," *Engineering Science and Technology, an International Journal*, vol. 20, no. 3, pp. 833–858, 2017.

[6] N. M. Kumar, K. Sudhakar, and M. Samykano, "Performance comparison of bapv and bipv systems with c-si, cis and cdte photovoltaic technologies under tropical weather conditions," *Case Studies in Thermal Engineering*, vol. 13, p. 100374, 2019.

[7] M. Tripathy, P. Sadhu, and S. Panda, "A critical review on building integrated photovoltaic products and their applications," *Renewable and Sustainable Energy Reviews*, vol. 61, pp. 451–465, 2016.

[8] F. J. Osseweijer, L. B. Van Den Hurk, E. J. Teunissen, and W. G. van Sark, "A comparative review of building integrated photovoltaics ecosystems in selected european countries," *Renewable and Sustainable Energy Reviews*, vol. 90, pp. 1027–1040, 2018.

[9] E. Delponte, F. Marchi, F. Frontini, C. Polo López, K. Fath, and M. Batey, "BIPV in EU28, from Niche to Mass Market: An Assessment of Current Projects and the Potential for Growth through Product Innovation," in *31st European Photovoltaic Solar Energy Conference and Exhibition*. WIP, nov 2015, pp. 3046–3050. [Online]. Available: www.eupvsec-proceedings.com/proceedings?paper=33873

[10] Y. Hiraki, "Solar cell panel assembly for driving motor-driven screen device," Jul. 9 1991, uS Patent 5,029,428.

[11] W. Corazzini, "Solar powered window shade," May 9 1995, uS Patent 5,413,161.

[12] P. P. Popat, "Solar-powered, wireless, retrofittable, automatic controller for venetian blinds and similar window converings," Jun. 2 1998, uS Patent 5,760,558.

[13] A. Liu, "Solar-powered window covering automation system," Nov. 5 2013, uS Patent 8,575,877.

[14] L. W. Reid and S. W. Reid, "Systems and methods for solar energy utilization," Jul. 11 2017, uS Patent 9,702,592.

[15] M. M. Moslehi and P. Kapur, "Solar photovoltaic blinds and curtains for residential and commercial buildings," Apr. 16 2015, uS Patent App. 14/275,869.

[16] Solar Gaps, "About a Product: What is SolarGaps SGV1." [Online]. Available: www.solargaps.com/about-product/

[17] Solar Curtain, "Models." [Online]. Available: www.solarcurtain.co

[18] Textiel Lab- Textiel Museum, "Inside Outside designs flexible solar curtain in Textile Lab." [Online]. Available: www.textiellab.nl/en/news/inside-outside-designs-flexible-solar-curtain

[19] A. H. Taieb, S. Msahli, and F. Sakli, "Design of illuminating textile curtain using solar energy," *The design journal*, vol. 12, no. 2, pp. 195–216, 2009.

[20] M. Helgesen, M. Jørgensen, T. Nielsen, and F. Krebs, "Printed polymer solar cells," in *Printed Films*. Elsevier, 2012, pp. 550–574.

[21] HomeTone, "Suntiles: Groovy green curtains." [Online]. Available: www.hometone.com/suntiles-groovy-green-curtains.html

[22] Kennedy and Violich Architecture, "IBA Softhouse." [Online]. Available: www.kvarch.net/projects/87

[23] Qanvast(2017), "Curtains Vs. Blinds: Which Is Better?" [Online]. Available: www.qanvast.com/sg/articles/curtains-vs-blinds-which-is-better-953

[24] M. A. Green, E. D. Dunlop, D. H. Levi, J. Hohl-Ebinger, M. Yoshita, and A. W. Ho-Baillie, "Solar cell efficiency tables (version 54)," *Progress in Photovoltaics: Research and Applications*, vol. 27, no. 7, pp. 565–575, 2019.

[25] M. A. Green, "Third generation photovoltaics: Ultra-high conversion efficiency at low cost," *Progress in Photovoltaics: Research and Applications*, vol. 9, no. 2, pp. 123–135, 2001.

[26] W. C. Sinke, "Development of photovoltaic technologies for global impact," *Renewable energy*, vol. 138, pp. 911–914, 2019.

[27] J. Benick, A. Richter, R. Müller, H. Hauser, F. Feldmann, P. Krenckel, S. Riepe, F. Schindler, M. C. Schubert, M. Hermle *et al.*, "High-efficiency n-type hp mc silicon solar cells," *IEEE journal of photovoltaics*, vol. 7, no. 5, pp. 1171–1175, 2017.

[28] F. Solar, "First solar builds the highest efficiency thin film pv cell on record," 2014.

[29] Solar Frontier(2019), "Solar Frontier Achieves World Record Thin-Film Solar Cell Efficiency of 23.35%." [Online]. Available: www.solar-frontier.com/eng/news/2019/0117_press.html

[30] T. Matsui, A. Bidiville, K. Maejima, H. Sai, T. Koida, T. Suezaki, M. Matsumoto, K. Saito, I. Yoshida, and M. Kondo, "High-efficiency amorphous silicon solar cells: impact of deposition rate on metastability," *Applied Physics Letters*, vol. 106, no. 5, p. 053901, 2015.

[31] C. E. Gemmer, *Analytische und numerische Untersuchungen von Solarzellen unter wechselnden Beleuchtungsbedingungen*. Der Andere Verlag, 2003.

[32] T.-M. I. Bajenescu, "Present and future of photovoltaics," *Electrotehnica, Electronica, Automatica*, vol. 63, no. 1, p. 31, 2015.

[33] B. M. Kayes, H. Nie, R. Twist, S. G. Spruytte, F. Reinhardt, I. C. Kizilyalli, and G. S. Higashi, "27.6% conversion efficiency, a new record for single-junction solar cells under 1 sun illumination," in *2011 37th IEEE Photovoltaic Specialists Conference*. IEEE, 2011, pp. 000 004–000 008.

[34] P. Chiu, D. Law, R. Woo, S. Singer, D. Bhusari, W. Hong, A. Zakaria, J. Boisvert, S. Mesropian, R. King *et al.*, "35.8% space and 38.8% terrestrial 5j direct bonded cells," in *2014 IEEE 40th Photovoltaic Specialist Conference (PVSC)*. IEEE, 2014, pp. 0011–0013.

[35] E. H. Jung, N. J. Jeon, E. Y. Park, C. S. Moon, T. J. Shin, T.-Y. Yang, J. H. Noh, and J. Seo, "Efficient, stable and scalable perovskite solar cells using poly (3-hexylthiophene)," *Nature*, vol. 567, no. 7749, p. 511, 2019.

[36] S. Dong, K. Zhang, B. Xie, J. Xiao, H.-L. Yip, H. Yan, F. Huang, and Y. Cao, "High-performance large-area organic solar cells enabled by sequential bilayer processing via nonhalogenated solvents," *Advanced Energy Materials*, vol. 9, no. 1, p. 1802832, 2019.

[37] M. Hosoya, H. Oooka, H. Nakao, T. Gotanda, S. Mori, N. Shida, R. Hayase, Y. Nakano, and M. Saito, "Organic thin film photovoltaic modules," in *Proceedings of the 93rd Annual Meeting of the Chemical Society of Japan*, 2013, pp. 21–37.

[38] InfinityPV(2019), "InfinityPV foil." [Online]. Available: www.infinitypv.com/products/opv/foil

[39] K. A. Schmitt, "Future of Energy: A Chemist and a Designer Team Up to Weave Solar Panels Into Fabric." [Online]. Available: www.smithsonianmag.com/innovation/chemist-designer-team-up-to-weave-solar-panels-into-fabric-180960431/

[40] Sandia National Laboratories, "Plane of Array (POA) Irradiance." [Online]. Available: www.pvpmc.sandia.gov/modeling-steps/1-weather-design-inputs/plane-of-array-poa-irradiance/

[41] D. Reindl, W. Beckman, and J. Duffie, "Evaluation of hourly tilted surface radiation models," *Solar energy*, vol. 45, no. 1, pp. 9–17, 1990.

[42] J. R. S. Brownson, "Empirical Correlation for Estimating Components of Light." [Online]. Available: www.e-education.psu.edu/eme810/node/683

[43] R. C. A McNeil, "Radsite-radiance-detailed description." [Online]. Available: www.radiance-online.org

[44] D. O'Reilly, "Computer generation of photorealistic images using ray tracing," Ph.D. dissertation, Dublin City University, 1991.

[45] M. Alhasni, "Multi-gpu parallelization of a dynamic heat transfer model on the moon," 2018.

[46] V. Muthukumar, "A new method for calculating solar irradiance on pv systems facing reflective surfaces," Master's thesis, Delft University of Technology, 2016.

[47] National Renewable Energy Laboratory, "Solar Spectra." [Online]. Available: www.nrel.gov/grid/solar-resource/spectra.html

[48] Meteonorm, "Irradiation data-Meteonorm Software." [Online]. Available: www.meteonorm.com/en/

[49] Neonsee, "Solar cell analysis systems." [Online]. Available: www.neonsee.com/en/solar-cell-analysis-systems/

[50] Victron Energy- Blue Power, "SmartSolar charge controller-MPPT." [Online]. Available: www.victronenergy.com/upload/documents/Datasheet-SmartSolar-charge-controller-MPPT-75-10,-75-15,-100-15,-100-20,-100-20_48V-EN.pdf

[51] Hanfong Winiversal, "Hanfong MPPT solar controller." [Online]. Available: www.inverters.cc/sale-8208124-hanfong-mppt-solar-controller-hot-sell40a-illimit-solaire-mppt-charge-controller-hot-victron-energy-.html

[52] B. Diouf and R. Pode, "Potential of lithium-ion batteries in renewable energy," *Renewable Energy*, vol. 76, pp. 375–380, 2015.

[53] Battery University Group, "BU-104a: Comparing the Battery with Other Power Sources." [Online]. Available: www.batteryuniversity.com/learn/article/comparing_the_battery_with_other_power_sources

[54] T. Guena and P. Leblanc, "How depth of discharge affects the cycle life of lithium-metal-polymer batteries," in *INTELEC 06-Twenty-Eighth International Telecommunications Energy Conference*. IEEE, 2006, pp. 1–8.

[55] Bol.com, "HP ProBook 440 G6 i5-8gb-256ssd." [Online]. Available: www.bol.com/nl/p/hp-probook-440-g6-i5-8gb-256ssd/9200000117101164/?Referrer=ADVNLGOO002021-G-63901387835-S-579027066627-9200000117101164&gclid=CjwKCAjw1f_pBRAEEiwApp0JKNhpyX_IigX-ZRUIe7FUZPLn1Q_h2laK7ATIeaXIxK3CZ2Jtv_Zx_RoCkNcQAvD_BwE

[56] S. E, "Best smartphones for long battery life." [Online]. Available: www.lowdown.carphonewarehouse.com/feature/best-smartphones-for-long-battery-life/39612/

[57] Battery University Group, "BU-409: Charging Lithium-ion." [Online]. Available: www.batteryuniversity.com/learn/article/charging_lithium_ion_batteries

[58] amazon.de, "Erchen Strom-betrieben LED Lichterkette, 165 FT 500 LED 50M Stecker dimmbare Kupfer Draht Lichterketten mit 12V DC Adapter ." [Online]. Available: www.amazon.de/Lichterketten-Sternenlichter-Kupferdraht-Fernbedienung-Warmwei%C3%9F/dp/B07MJR9GDK/ref=sr_1_3?keywords=kupferdraht+500+leds&qid=1554301948&s=gateway&sr=8-3

[59] Gaisma. [Online]. Available: www.gaisma.com/en/location/delft.html

[60] Gearbest, "GZGW09 3D Printer Reprap Stepper Motor Driver Module Works with Official Arduino." [Online]. Available: www.gearbest.com/development-boards/pp_101725.html

[61] E. Kondili, "Design and performance optimisation of stand-alone and hybrid wind energy systems," in *Stand-Alone and Hybrid Wind Energy Systems*. Elsevier, 2010, pp. 81–101.

[62] Eternal Sun, "Solar Competence Center." [Online]. Available: www.eternalsun.com/services/solar-competence-center/

[63] H. Hellinga, "Daylight and view: The influence of windows on the visual quality of indoor spaces," Ph.D. dissertation, Delft University of Technology, Netherlands, 2013.

[64] "Chapter 2: Radiometry- measuring light." [Online]. Available: www.cmp.felk.cvut.cz/cmp/courses/dzo/resources/chapter_radiometry_forsyth.pdf

[65] M. Janecek and W. W. Moses, "Optical reflectance measurements for commonly used reflectors," *IEEE transactions on nuclear science*, vol. 55, no. 4, pp. 2432–2437, 2008.

[66] C. Wang and S.-i. Kamata, "Removal of transparent plastic film specular reflection based on multi-light sources," in *2012 Symposium on Photonics and Optoelectronics*. IEEE, 2012, pp. 1–4.

[67] E. Csanády, E. Magoss, and L. Tolvaj, *Quality of machined wood surfaces*. Springer, 2015.

[68] E. D. Urzua, "Optical effects of curvature on current density of pv modules with complex geometries," Master's thesis, Delft University of Technology, 2016.

[69] "High efficiency bifacial monocrystalline solar cell 4bb." [Online]. Available: www.wisebiz.en.alibaba.com/product/62109057880-801397098/High_efficiency_Bifacial_Monocrystalline_Solar_Cell_4bb.html

[70] V. Fakhfouri *et al.*, "Iec 60904-1-2: Measurement of current-voltage characteristics of bifacial photovoltaic devices," in *Presentation at 3rd bifi PV workshop, Miyazaki, Japan*, 2016.

[71] A. Weeber, L. Slooff-Hoek, P. Danzl, and P. Manshanden, "Challenges for Bifacial solar cell and module measurements-ECN," Tech. Rep. [Online]. Available: www.publicaties.ecn.nl/PdfFetch.aspx?nr=ECN-O--17-024

[72] A. Mansouri, M. Zettl, O. Mayer, M. Lynass, M. Bucher, O. Stern, and R. Burhenne, "Defect detection in photovoltaic modules using electroluminescence imaging," in *27th European Photovoltaic Solar Energy Conference and Exhibition*, 2012, pp. 3374–3378.

[73] A. Smets, "Et3034tux solar energy course," 2013.

[74] Pico Technology, "8 channel thermocouple data logger." [Online]. Available: www.picotech.com/data-logger/tc-08/thermocouple-data-logger

[75] M. Warren, "Make coiled wire." [Online]. Available: www.instructables.com/id/Make-Coiled-Wire/

[76] I. Nawaz and G. Tiwari, "Embodied energy analysis of photovoltaic (pv) system based on macro-and micro-level," *Energy Policy*, vol. 34, no. 17, pp. 3144–3152, 2006.

[77] N. Gazbour, G. Razongles, C. Schaeffer, and C. Charbuillet, "Photovoltaic power goes green," in *2016 Electronics Goes Green 2016+(EGG)*. IEEE, 2016, pp. 1–8.

[78] W. Luo, Y. S. Khoo, A. Kumar, J. S. C. Low, Y. Li, Y. S. Tan, Y. Wang, A. G. Aberle, and S. Ramakrishna, "A comparative life-cycle assessment of photovoltaic electricity generation in singapore by multicrystalline silicon technologies," *Solar Energy Materials and Solar Cells*, vol. 174, pp. 157–162, 2018.

[79] Wuhan Sunic Photoelectricity Equipment Manufacture Co. Ltd, "Solar cell laser cutting machine." [Online]. Available: www.alibaba.com/product-detail/solar-cell-laser-cutting-machine-Germany_60202503701.html

[80] V. Fthenakis, H. Kim, R. Frischknecht, M. Raugei, P. Sinha, M. Stucki *et al.*, "Life cycle inventories and life cycle assessment of photovoltaic systems," *International Energy Agency (IEA) PVPS Task*, vol. 12, 2011.

[81] M. C. McManus, "Environmental consequences of the use of batteries in low carbon systems: The impact of battery production," *Applied Energy*, vol. 93, pp. 288–295, 2012.

[82] Eclipse Shutters, "Lifetime of california or plantation shutters." [Online]. Available: www.eclipseshutters.ca/lifetime-of-california-or-plantation-shutters

[83] S. D. Jain, *Engineering physics*. Universities Press, 2010.

[84] PV Lighthouse. [Online]. Available: www.pvlighthouse.com.au/refractive-index-library

[85] A. Sayigh, *Solar energy application in buildings*. Elsevier, 2012.

[86] N. Levati, L. Vitali, D. Fustinoni, and A. Niro, "Spectrophotometric evaluation of optical performances of polarizing technologies for smart window applications," in *Journal of Physics: Conference Series*, vol. 547, no. 1. IOP Publishing, 2014, p. 012013.

[87] F. Padera and C. Shelton, "Uv/vis spectroscopy."

[88] PerkinElmer, "Application note- transmission measurements using integrating spheres for the lambda 950/850/650 uv/vis/nir and uv/vis spectrophotometers." [Online]. Available: www.perkinelmer.com/cmsresources/images/44-74192app_lambda950850650transmsrmts.pdf

[89] Lasergraaf, "Q-switched fiber markeer laser "emma" full desk." [Online]. Available: www.lasergraaf.nl/product/20-30-watt-q-switched-fiber-laser-emma/

A

Model Geometry

This appendix shows dimensional detailing for geometries developed in Rhino for ray-tracing. Section A.1 concerns the models related to the validation setup and section A.2 deals with the office room model.

A.1. Validation Model

Dimensional drawing of the various cases developed in chapter 3 are shown in the figures below. Figure A.1 shows the front view of the room while Figure A.2 and Figure A.3 show the side and top view of the Furniture case respectively. Note, all shown **dimensions are in millimetres**. Also, the un-rippled curtain length is 700 mm.

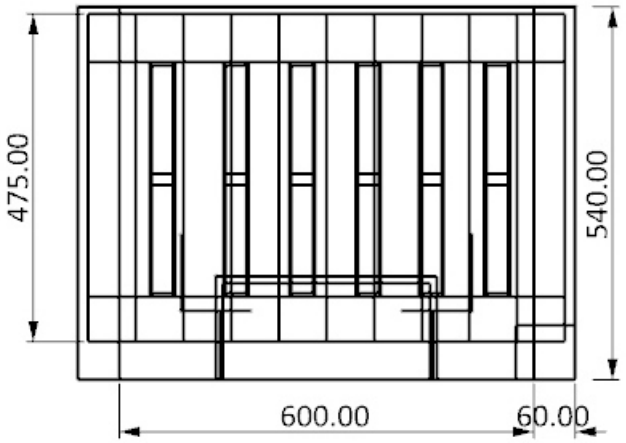

Figure A.1: Front view of room with curtain

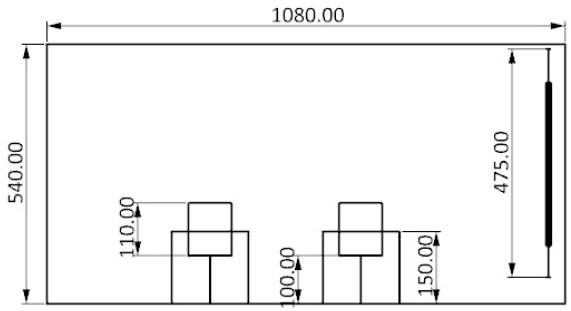

Figure A.2: Side view of room with furniture case

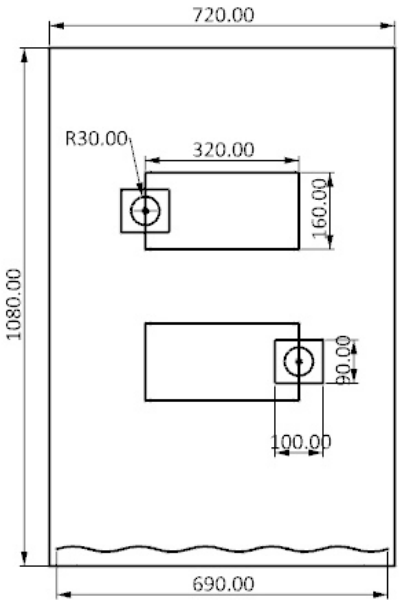

Figure A.3: Top view of room with furniture case

Figures A.4 and A.5 show the side and top view of the 'wall' cases respectively. Since the two cases of black and white wall only differ in color, their structural geometry is identical.

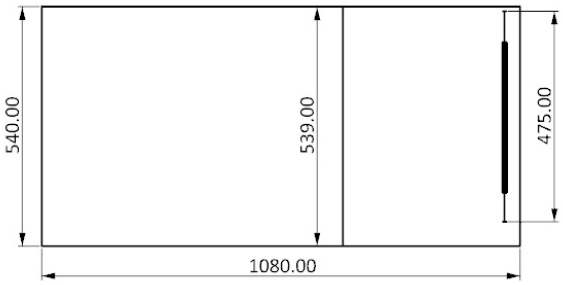

Figure A.4: Side view of room with white or black wall

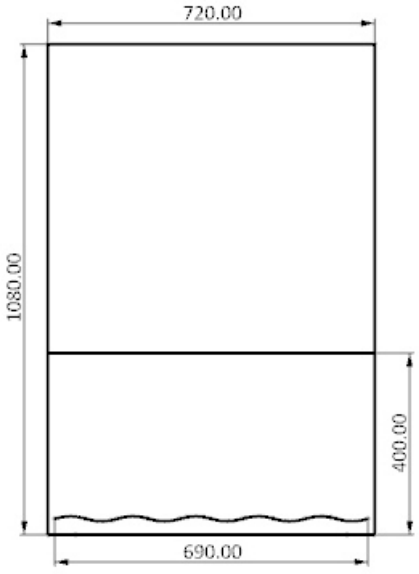

Figure A.5: Top view of room with white or black wall

A.2. Office Room

The figures below show the model developed in RHINO for the target room, with **dimensions in metres**, is shown in Figures A.6, A.7 and A.8

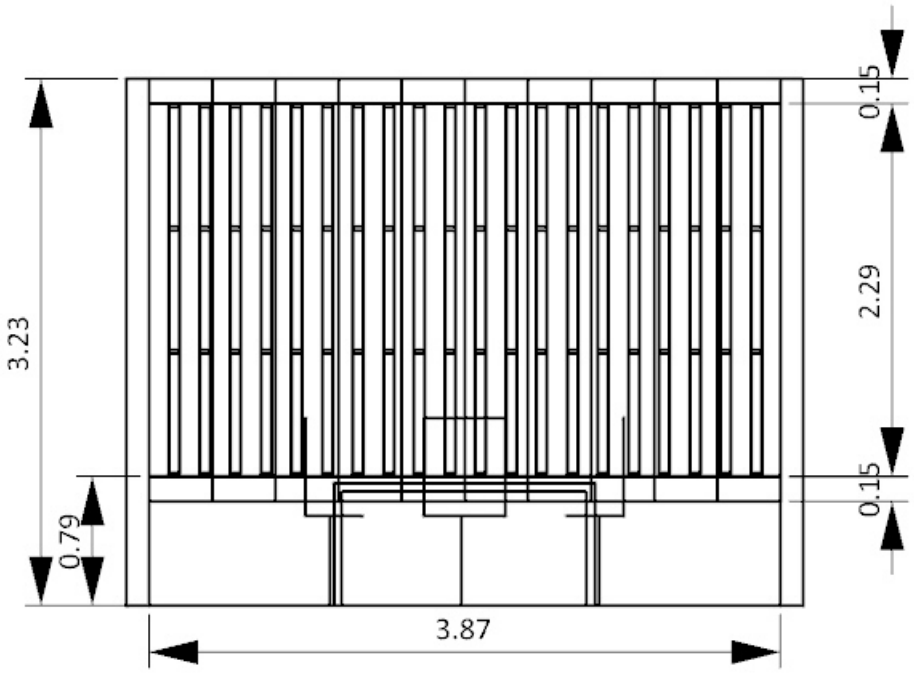

Figure A.6: Front view of office room with PV curtain

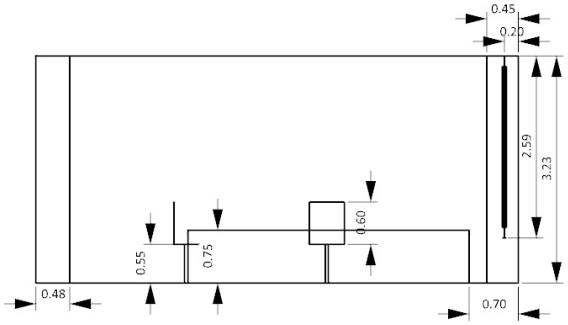

Figure A.7: Side view of office room with PV curtain

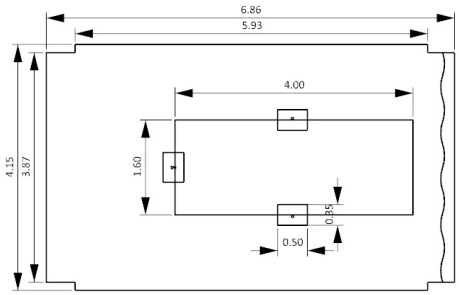

Figure A.8: Top view of office room with PV curtain

B

Optical Properties

This appendix will discuss various assumptions and methodologies applied in fixing the optical properties of the constituents of the model developed in LightTools, starting with the calculations for glass facades deployed in subsection B.1, followed by optical measurements in the Lambda 950 UV/VIS spectrophotometer of Perkin Elmer.

B.1. Equivalent glass surface model

For an electromagnetic ray traversing from medium 1 to 2, Snell's law,

$$n_1 sin(\theta_i) = n_2 sin(\theta_r) \tag{B.1}$$

where n_1 and n_2 are refractive indices of medium 1 and 2 respectively. This can be visualized better in Figure B.1.

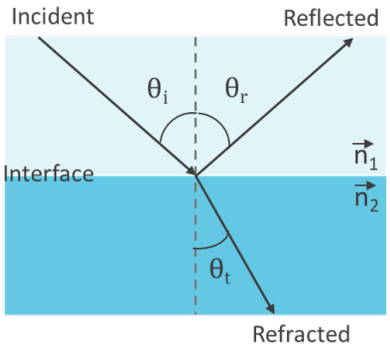

Figure B.1: Path of ray as it traverses from one medium to another

To effectively model the relation between incident, reflected and refracted beams at any interface, Fresnel's equations are used. These are given by:

$$r_s = \frac{n_1 cos(\theta_i) - n_2 cos(\theta_t)}{n_1 cos(\theta_i) + n_2 cos(\theta_t)} \tag{B.2}$$

$$t_s = \frac{2n_1 cos(\theta_i)}{n_1 cos(\theta_i) + n_2 cos(\theta_t)} \tag{B.3}$$

where r_s and t_s indicate the reflection and transmission coefficients for s-polarized or perpendicularly polarized light and

$$r_p = \frac{n_1 cos(\theta_t) - n_2 cos(\theta_i)}{n_1 cos(\theta_t) + n_2 cos(\theta_i)} \tag{B.4}$$

$$t_p = \frac{2n_1 cos(\theta_i)}{n_1 cos(\theta_t) + n_2 cos(\theta_i)} \tag{B.5}$$

where r_p and t_p indicate the reflection and transmission coefficients for p-polarized or parallel polarized light. Natural sunlight is said to be unpolarized [83]. For unpolarized light, the mean of the two reflection coefficients is taken to give reflectance R as:

$$R = \frac{{r_p}^2 + {r_s}^2}{2} \tag{B.6}$$

Assuming that at the interface, no absorption takes place, we can say that

$$R + T = 1$$

where T is the coefficient of transmission. Hence,

$$T = \frac{n_2 cos(\theta_t)}{2n_! cos(\theta_i)} ({t_s}^2 + {t_p}^2) \tag{B.7}$$

Now that a relation for coefficients of transmission and reflection at the interface have been established, it is also important to characterize the absorption taking place in the bulk. A relation for absorption related attenuation of rays in a medium is given by the Lambert-Beer law as follows:

$$I(\lambda, x) = I_o(\lambda) exp(-\alpha(\lambda) x) \tag{B.8}$$

All the equations used above are used to convert the complicated air-glass-air profiles of the two geometries modelled, into an equivalent profile shown below in Figure B.2

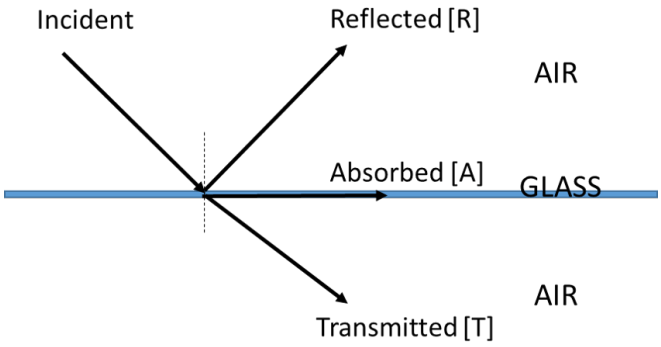

Figure B.2: Equivalent coefficients of reflection, transmission and absorption for representing glass of finite thickness with a surface

B.1.1. Validation model

In case of the validation model, only a single glass of 60 cm × 60 cm having 3 mm thickness was used to simulate the window of the room. This can be represented in Figure B.3, where the numbers on the right indicate the medium. In this case medium 1 is air outside, medium 2 is the glass and medium 3 is the air inside the room. r_{12} and t_{12} thus represent reflection and transmission coefficients at the interface of mediums 1 and 2. The effect of absorption is accounted for by attenuating the base signal every time it traverses the glass. Equivalent coefficients were calculated for angles of incidence from 0 °to 90 °for wavelengths from 300 nm to 2500 nm. Values for real refractive index (n), extinction coefficient (k) and absorption coefficient (α) of Pil low-iron sodalime glass were obtained from the PV Lighthouse database [84]. The terms appearing at the top (along with the influence of absorption attenuation) are summed to obtain the equivalent reflectance of the arrangement. Similarly, summing up the terms appearing below the lower glass gives the equivalent transmittance of the arrangement. The rest is assumed to be absorbed in the bulk of the glass.The optical profile of the equivalent glass surface to be modelled in the LightTools for a normal incidence of light, is plotted in Figure B.5

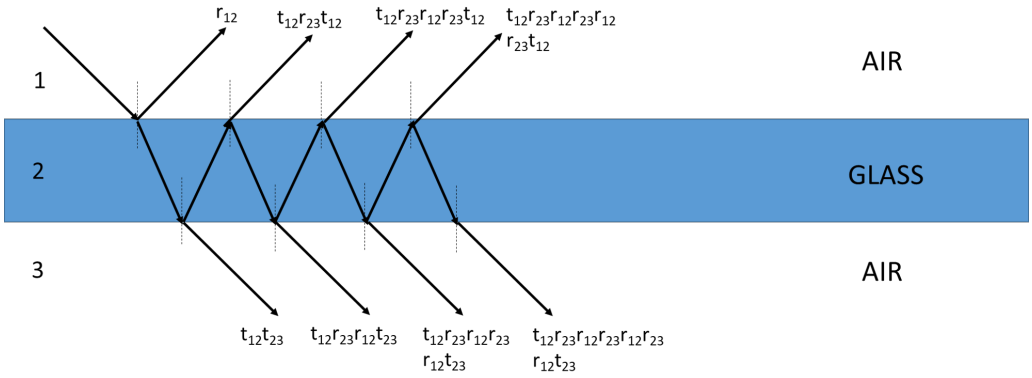

Figure B.3: The air-glass-air interface in validation model that needs to be represented as Figure B.2

B.1.2. Office Room

Contrary to the validation model, the office room is located in a building with a double skin facade. Double skin facade is an architectural terminology to describe a building having two glass facades separated by an air gap for ventilation. In the case of the office room, the arrangement comprises a 3 mm thick outer glass facade separated by an air gap of 1 m from the second glass window facade of again 3 mm thickness. The arrangement can be seen schematically in Figure B.4. Similar relations as described for the validation model, are used to obtain equivalent wavelength and AOI dependent reflectance, absorptance and transmittance for the arrangement shown in the figure.

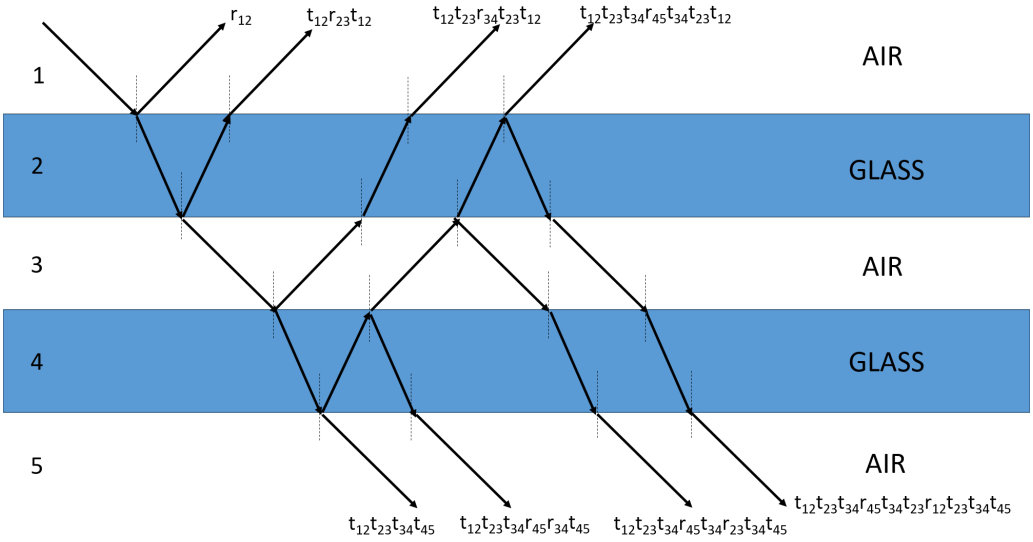

Figure B.4: The double skin facade that needs to be represented as Figure B.2

The wavelength dependent property variation for both arrangements for a normal incidence is seen in figure B.6 and figure B.5. These results (for the validation model glass) are found to be conclusive with literature that claims a transmittance of approximately 92 % for normal incidence for a clear, non-absorptive glass [85].

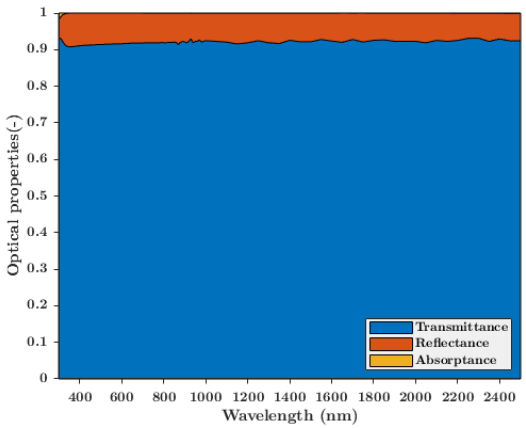

Figure B.5: Optical profile (for normal incidence) of glass in validation model

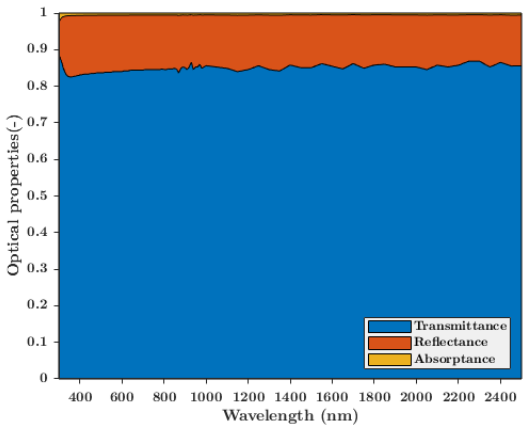

Figure B.6: Optical profile (for normal incidence) of glass in office model

B.2. Measurement of optical properties using Spectrophotometry

Optical reflectance and transmission coefficients of materials used in the validation model were measured using the PerkinElmer Lambda 950 UV-Vis-NIR double monochromator spectrometer.The sources of the double rays are a deuterium lamp for the UV region, and a tungsten lamp for the Vis/NIR range. Lambda 950 comes with a 150 mm spectralon integrating sphere mounting a Photomultiplier Tube (PMT) sensor for the UV-Vis range, and a Gallium Arsenide (InGaAs) sensor for NIR measurements where the switch between the two detectors occurs at 860 nm. The total spectral range is between 200 and 2500 nm with a wavelength accuracy of ± 0.08 nm in the UV/Vis range, and ±0.30 nm in the NIR range[86]. The instrument has been calibrated with a certified Spectralon sample where the measurement errors, both in reflectance and transmittance mode, are less than 0.11 % in the UV-Vis range, and less than 0.23 % in the NIR range. For the measurements presented in this section, a measurement range of 300 and 1200 nm with 5 nm - 10 nm intervals is chosen. Note: reflection measured here comprises diffuse and specular components. Figure B.7 shows an exterior view of the Lambda 950 spectrophotometer [87]. The schematic below in Figure B.8 shows a top view of the measuring equipment.

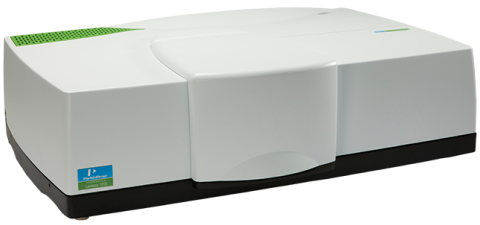

Figure B.7: Picture of 150 mm integrating sphere installed in the Lambda 950 spectrometer [87]

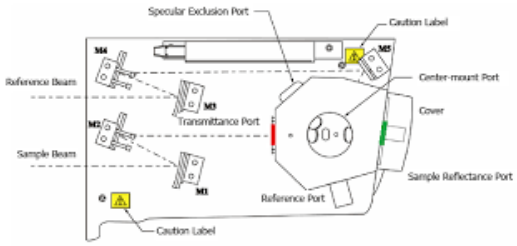

Figure B.8: Schematic of Lambda 950 where the green line marks the area where transmission is measured and red line marks the reflection area [87]

The operating principal of the measuring equipment can be better understood from Figure B.9.

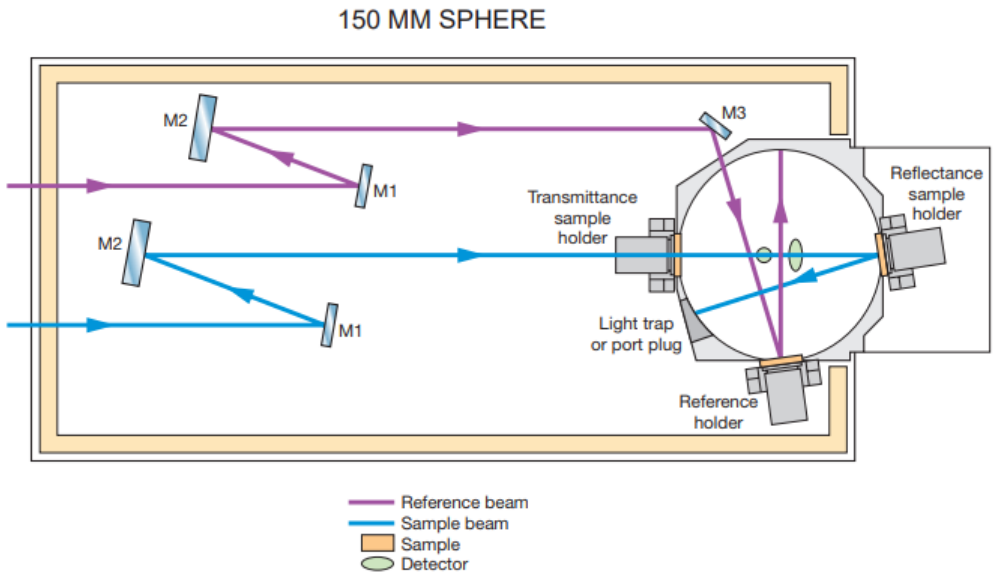

Figure B.9: PerkinELmer 950 working principal adapted from [88]

For a fair comparison between simulation and the real setup, material properties of components in the setup as mentioned in part 3.1 are measured using the above apparatus and entered in ray tracing package LightTools. Figure B.10 shows the sample preparation for measurement using spectrometry. Sample size is restricted by measurement equipment to be within 50 mm by 50 mm.

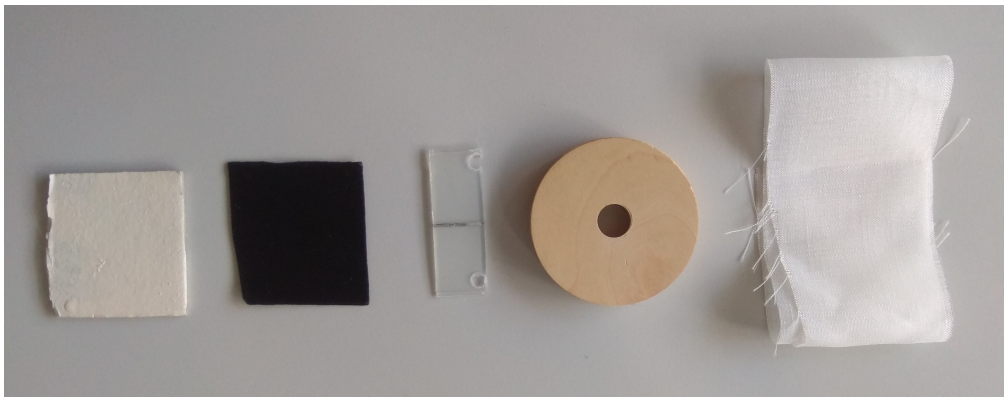

Figure B.10: Samples prepared for testing

The figures below show measured plots of reflectance, transmittance and absorptance for the cloth of the curtain (Figure B.11, double cloth (from top and bottom curtain collars- Figure B.12), wood furniture sample taken from the wooden chair in the model-Figure B.13), plastic-EVA laminated encapsulation piece B.14, white intermediate wall cut-out (Figure B.15) and black intermediate wall cut-outs (Figure B.16) respectively.

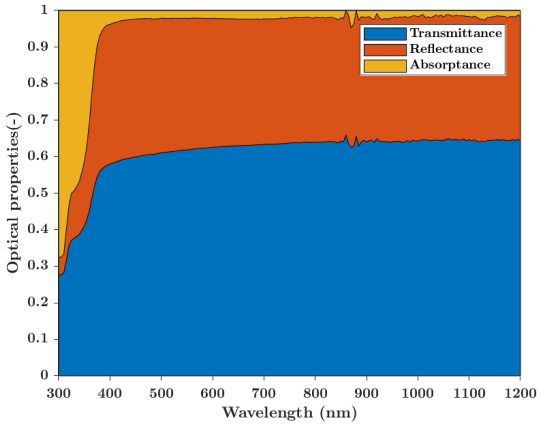

Figure B.11: Optical profile (for normal incidence) of cloth strips in Validation model

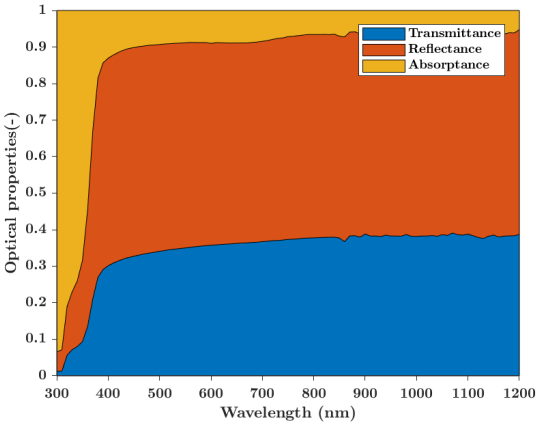

Figure B.12: Optical profile (for normal incidence) of double cloth collar in Validation Model

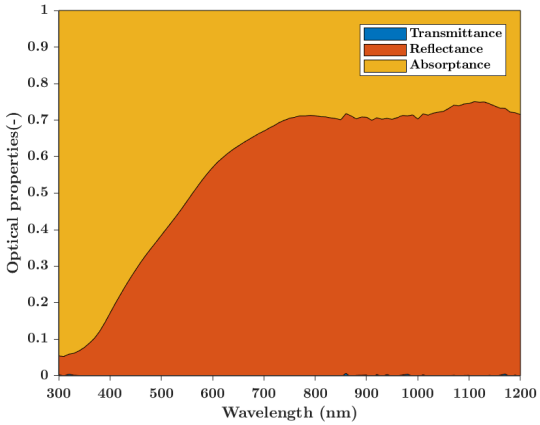

Figure B.13: Optical profile (for normal incidence) of wood furniture in Validation model

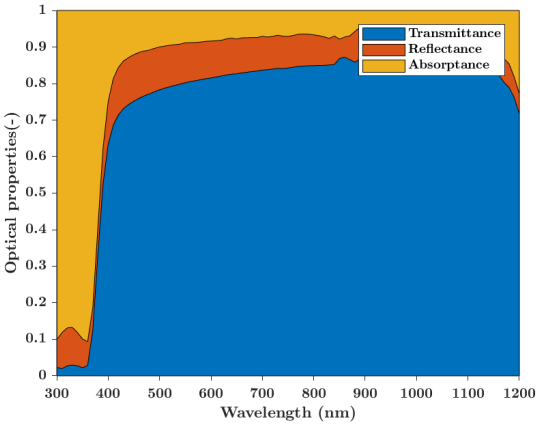

Figure B.14: Optical profile (for normal incidence) of plastic-EVA encapsulant in Validation Model

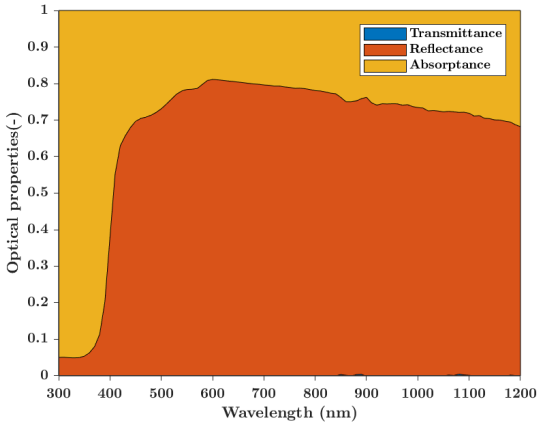

Figure B.15: Optical profile (for normal incidence) of white intermediate wall in Validation model

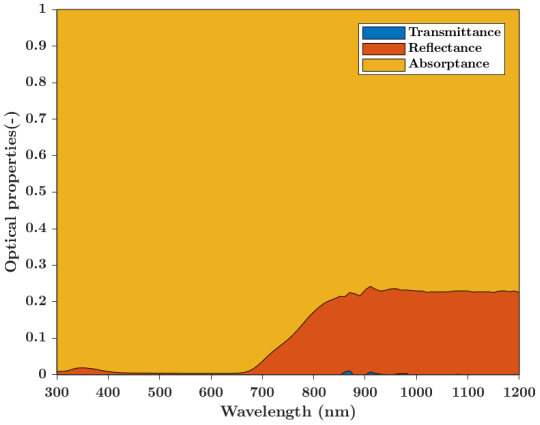

Figure B.16: Optical profile (for normal incidence) of black intermediate wall in Validation Model

C

Mini module fabrication and characterization

This appendix starts with the devices used for fabrication, followed by the datasheet of the base cell used and subsequently, IV measurement results and electroluminescence images for cells and mini modules.

C.1. Laser-cutting specifications

Bifacial mono crystalline silicon solar cells were cut using the Q-switched fiber mark laser EMMA full desk [89], a class 1 fiber system equipped with a computer as shown in Figure C.1.

Figure C.1: Lasergraaf Q-switched fiber mark laser EMMA

The working principle of the laser involves use of high energy density in the focus point of the laser beam which results in melting and evaporation of the material. Adjustable mirrors and an F-theta lens are used to direct the high power laser beam. The cutting process for each specific material can be optimized for a smooth cut by adjusting laser parameters such as scanning speed, laser power, frequency, pulse width and number of scans. The optimum parameters attained for the PERC bifacial cells used in the current research, with EMMA, are shown in Table C.1.

Table C.1: Laser parameters used to obtain smooth cut without jagged edges

Parameter	Value
Speed [mm/s]	450
Power [%]	100
Frequency [KHz]	90
Q Pulse Width [ns]	20

C.2. Cell Lamination

Experia Photovoltaic LAM600 laminator (in Figure C.2 was used for lamination of the bifacial mini modules described in Chapter 3.With a peak power of 6 KW, the laminator is able to achieve temperatures as high as 180 ° C. The process of lamination begins with placing the sample in a pre-heated laminator and creating vacuum to remove air and avoid bubble formation. Since the crosslinking of the EVA and curing requires a temperature of about 140° C-150° C, a maximum temperature of 140 ° C is set for the lamination cycle. Also, the application of pressure helps to enhance the distribution of molten EVA ensuring better adhesion between different sub-layers of the module. By trial, a maximum in-cycle pressure of 200 mbar was found to be suitable for foil-foil modules without causing any damage to the module.

Figure C.2: Experia Photovoltaic LAM600 laminator used for laminating the mini modules in chapter 3

C.3. Bifacial PV solar-cell datasheet

WISEBIZ LIMITED

CHINALAND SOLAR ENERGY
www.wisebiz-solar.com

WB B6-5 5BB Bi-Facial Mono-Crystalline Silicon Solar Cell

MECHANICAL DATA AND DESIGN	
Dimension	156.75mm×156.75mm±0.25mm
Thickness	180um±30um
Front(-)	Five 0.8mm wide bus bars(silver) with distance 31.2mm , acid texturized surface with blue silicon nitride AR coating
Back(+)	1.4mm wide silver/aluminum soldering pads, aluminum local back surface field

TYPICAL ELECTRICAL CHARACTERISTICS									
Efficiency	Eff(%)	21.60	21.50	21.40	21.30	21.20	21.10	21.00	20.90
Power	Ppm(W)	5.277	5.253	5.228	5.204	5.18	5.155	5.131	5.106
Open Circuit Voltage	Voc(V)	0.670	0.699	0.669	0.668	0.667	0.666	0.666	0.665
Max.Power Voltage	Vpm(V)	0.569	0.567	0.565	0.563	0.561	0.560	0.558	0.556
Short Circuit Current	Isc(A)	9.799	9.788	9.778	9.767	9.756	9.745	9.734	9.724
Max.Power Current	Ipm(A)	9.283	9.269	9.256	9.242	9.228	9.214	9.200	9.186

Standard test conditions: AM1.5, 1000W/㎡, 25℃ . efficiency tolerance :average +0.3%/-0.1% absolute.

TEMPERATURE COEFFICIENTS		
Current Temperature Coefficient	α(Isc)	.+0.0413 %/K
Voltage Temperature Coefficient	β(Voc)	.-0.2835 %/K
Power Temperature Coefficient	γ (Pmax)	.-0.3673 %/K

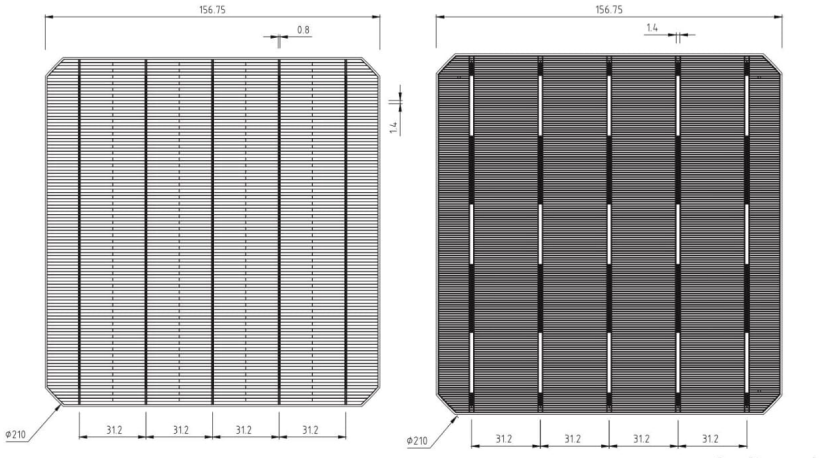

Package Configuration
Typical package for one carton contains 1,200 cells sealed in cell box every 100pc
Gross weight per unit carton shall be around 16.6kg

IV Curve

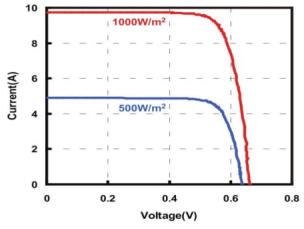

Figure C.3: Datasheet of bifacial cells used for mini modules

C.4. IV Curve measurement-Konika Minolta reference cell (Neonsee)

The neonsee solar cell analysis system (as seen in Figure C.4), at Solliance is a steady state solar simulator having an 'exceeding class AAA solar simulation' [49].

Figure C.4: Neonsee solar cell analysis system [49]

This section will discuss the results of IV measurements when using the Konica Minolta AK-200 as reference cell. After manual calibration and irradiance attenuation as described in chapter 3, first a hysteresis check was run. The following plot (Figure C.5) was obtained. The slight difference is curves can be a source of reduced accuracy but for simplicity is assumed negligible in the current research. Note, this hysteresis behaviour is for measurements using the full c-Si 6" bifacial PERC cell. Figure C.6 shows the IV curves for different conditions of illumination of the PV mini module used in the curtain fabrication.

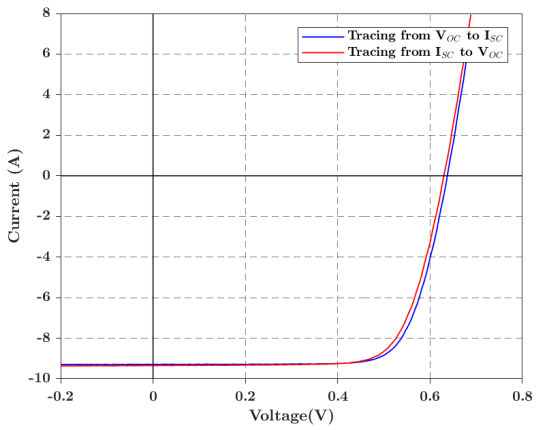

Figure C.5: Hysterisis curve for IV measurement of full non-laminated bifacial c-Sir PERC cell

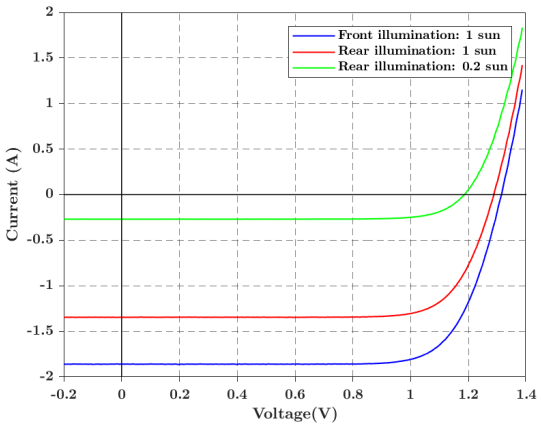

Figure C.6: IV curves for 1 sun illumination of front and rear sides and 0.2 sun rear illumination of PV mini module

The Table C.2 shows the IV parameters for all sample cases attempted with reference cell AK-200. It must be noted that this technique of measuring from beyond the range of the IV curve is to counter any capacitance related adverse effects associated with the measuring equipment. The results can be interpreted as follows:

- Counter-intuitively, the efficiency of the full cell is seen to rise with cutting (comparing between non laminated full cell and non laminated, half mini module cut cell). This could be attributed to lower

power losses in the cut cell due to lesser area and current carrying tabbing wires as compared to the full cell. Other likely causes could be an inherent different in performance between the two base cells since the manufacturer states a variation in output power from 5.10 W to 5.27 W for the same batch of cells.

- The table also shows that the non-laminated version of full cell gives better results than the laminated version. Lamination imparts anti-reflective properties to the c-Si cells due to optical coupling, which should ideally result in a higher power yield. another possible reason for this unexpected trend could be the existence of air bubbles within the lamination (due to slight change in recipe owing to the replacement of thermal heating pad in Laminator). The bubbles shade direct illumination of cell, resulting in a poorer performance than anticipated.

Table C.2: IV curve measurement summary for samples tested under reference cell (AK-200)

Sample	Side	P_{MPP}(W)	V_{MPP}(V)	I_{MPP}(A)	V_{OC}(V)	I_{SC}(A)	η (%)	Bifaciality (%)
Full cell (non-laminated)	Front	4.473	0.514	8.696	0.643	9.292	18.41	
	Rear	2.637	0.521	5.064	0.631	5.423	10.85	59
	Rear*	0.487	0.500	0.962	0.593	1.074	9.90	
Full cell (laminated)	Front	4.425	0.529	8.371	0.657	9.006	18.21	
	Rear	2.613	0.532	4.913	0.643	2.268	10.75	59
	Rear*	0.487	0.508	0.958	0.599	1.056	10.02	
Mini module	Front	1.840	1.057	1.741	1.313	1.860	18.81	
	Rear	1.324	1.050	1.260	1.287	1.345	13.54	72
	Rear*	0.249	0.994	0.250	1.185	0.269	12.71	
Cut-cell (non-laminated)	Front	0.907	0.515	1.761	0.633	1.879	18.54	
	Rear	0.574	0.522	1.100	0.629	1.173	11.73	63
	Rear*	0.107	0.497	0.216	0.590	0.234	10.98	
Cut-cell (laminated)	Front	0.877	0.503	1.743	0.634	1.882	17.92	
	Rear	0.614	0.516	1.190	0.633	1.280	12.55	70
	Rear*	0.114	0.487	0.233	0.585	0.255	11.62	

*rear side at 0.2 sun (200 W/m^2) illumination

C.5. Testing of bifacial cells using bifacial reference (Wacom)

The testing of bifacial full cells was repeated after the measurements at Solliance, at ECN-TNO in Petten, the Netherlands, by calibrating the Wacom cell measurement unit a bifacial c-Si cell. The results are seen to be much different from the ones measured using the Konica Minolta reference cell at Solliance, especially in terms of current measurement. This is attributed mainly to the losses due to poor connectivity of the tabbing wires with the cell and shading occurring due to these bus bars. Table C.3 shows the results of the measurements. Of 8 cells tested, the last three showed hair fractures. This helps in giving an idea on how much the cells in the same batch differ in performance.

Table C.3: Results from base (non-laminated) cell measurements for a batch of 8 cells, conducted in ECN-TNO at Petten.

Cell	I_{SC} (A)	V_{OC} (V)	I_{MPP} (A)	V_{MPP} (V)	P_{MPP} (W)	FF (-)	η (%)
Good cells							
1	9.453	0.660	8.913	0.561	5.001871	0.801	20.499
2	9.464	0.661	8.946	0.561	5.017199	0.802	20.562
3	9.440	0.658	8.965	0.562	5.038365	0.811	20.649
4	9.493	0.656	9.005	0.556	5.010803	0.805	20.536
5	9.423	0.655	8.875	0.559	4.961935	0.804	20.336
Poor cells							
6	9.569	0.669	9.015	0.551	4.969202	0.777	20.366
7	9.465	0.657	8.898	0.558	4.967226	0.799	20.357
8	9.538	0.664	8.866	0.547	4.848832	0.765	19.872

C.6. Electroluminescence Images

Electroluminescence images of rear surface of PV samples from section 3.2.2 of chapter 3 are shown in Figures C.7 - C.10

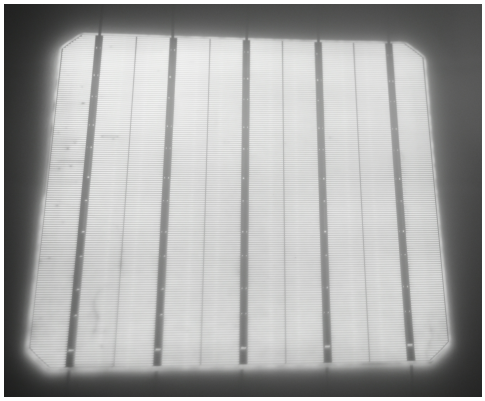

Figure C.7: Non-laminated full cell EL

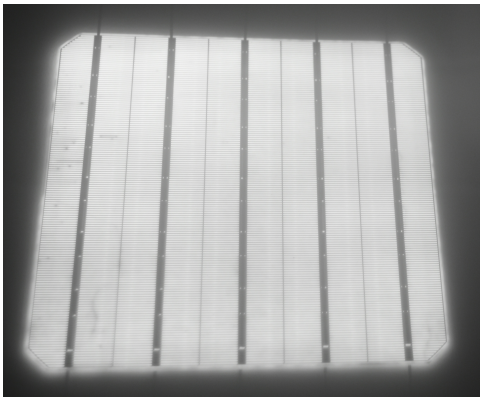

Figure C.8: Laminated full cell EL

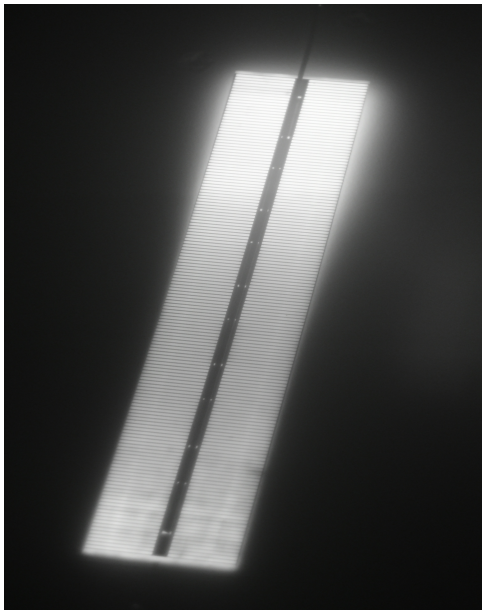

Figure C.9: Non-laminated cut cell EL

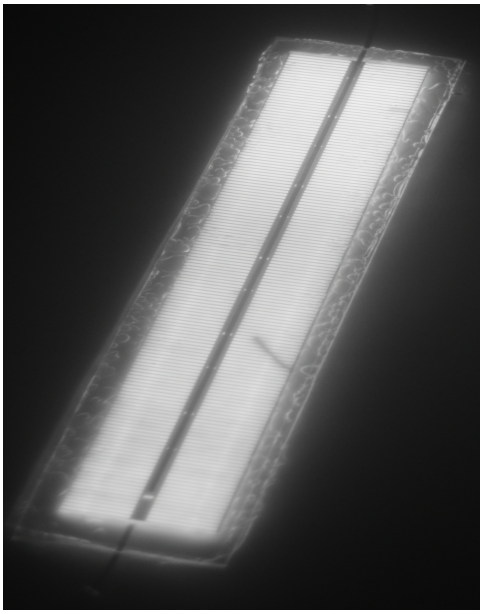

Figure C.10: Laminated cut cell EL

D

Validation Model Results

Detailed IV curve results are discussed in section D.2 of this appendix, preceded by an image of location of temperature sensors in the model in section D.1.

D.1. Test rig for Validation Case

The location of temperature sensors in the validation model can be seen in Figure D.1

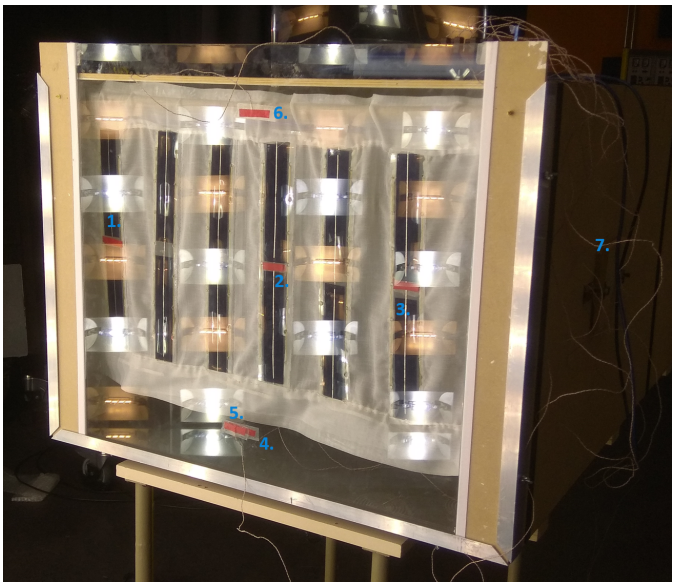

Figure D.1: Location of temperature sensors in model

D.2. IV Curve measurements for validation cases

IV curve parameters for the four cases measured are shown in Table D.1

Table D.1: IV curve measurement summary for samples tested

Case	P_{MPP}(W)	V_{MPP}(V)	I_{MPP}(A)	V_{OC}(V)	I_{SC}(A)	η (%)
Reference	11.938	6.251	1.910	8.004	1.959	20.344
Furniture	12.359	6.072	2.035	7.867	2.119	21.061
White wall	13.152	6.145	2.140	7.926	2.260	22.413
Black wall	12.525	6.182	2.026	8.104	2.137	21.345

E

Office Model Results

The sky and sensitivity maps for three cases discussed in chapter 4.1 are discussed in section A.2 followed by the case of POA irradiance on a c-Si module at the same location and tilt as that of the PV curtain in an office room, but at optimal azimuth in section E.2.

E.1. Sensitivity and Sky maps for Basecase

Figure E.1 shows the front view of the room curtain, where the PV is shown in orange and cloth in light white-grey. Figures E.2 to E.7 show the comparison between skymaps and irradiance recorded on the PV curtain at different points of time in the day. Here too, the grey bands in the irradiance map indicate cloth stripes.

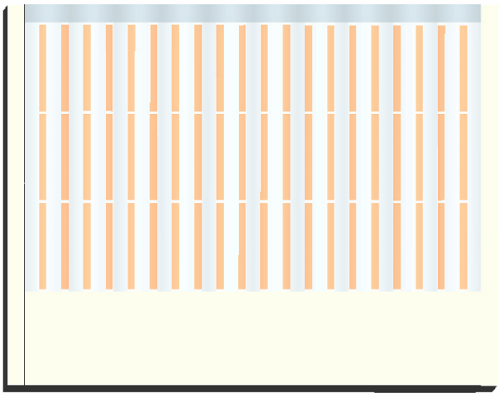

Figure E.1: Front view of PV curtain with PV shown in orange and cloth in white-grey

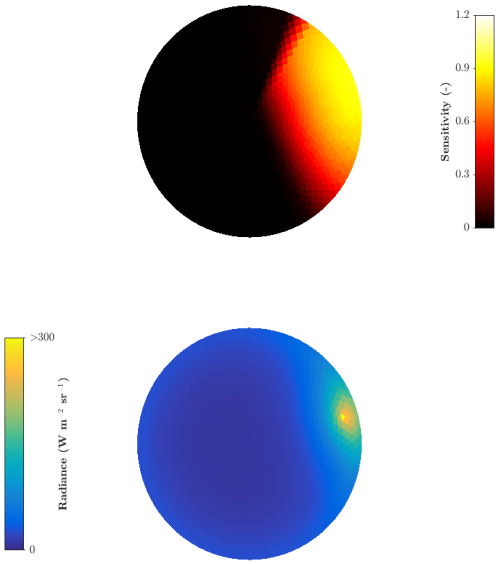

Figure E.2: Sensitivity map (top) for a single PV surface and sky map (bottom) for 7 am on 30^{th} June

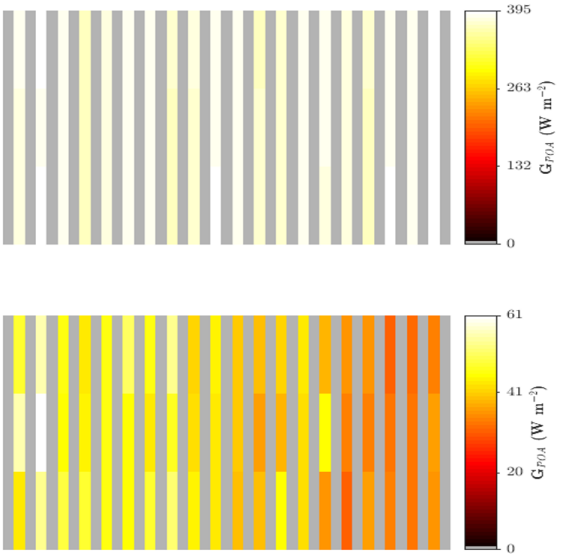

Figure E.3: Irradiance on the front face (top) and rear face (bottom) of the PV curtain at 7 am on 30^{th} June

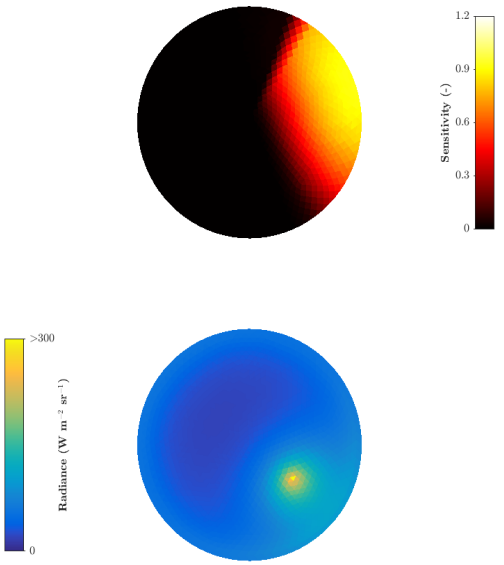

Figure E.4: Sensitivity map (top) for a single PV surface and sky map (bottom) for 11 am on 30^{th} June

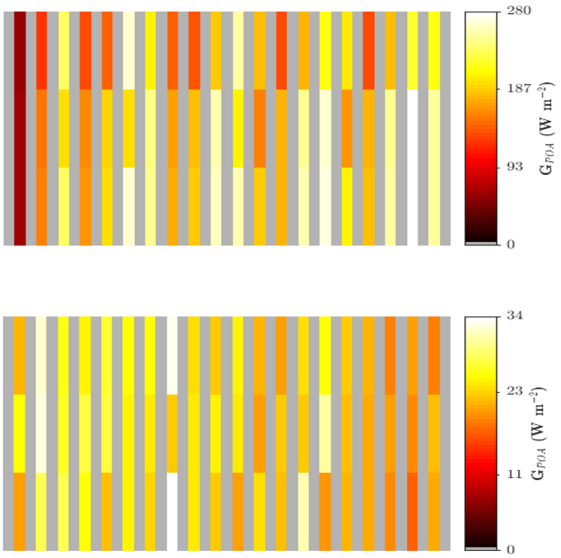

Figure E.5: Irradiance on the front face (top) and rear face (bottom) of the PV curtain at 11 am on 30^{th} June

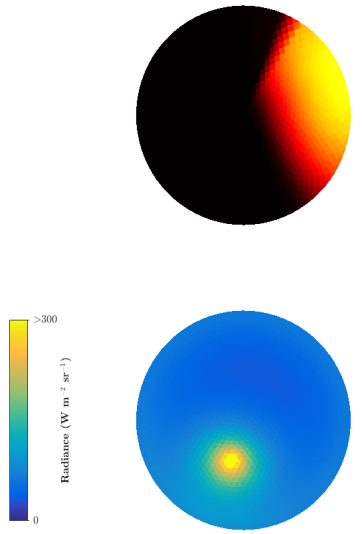

Figure E.6: Sensitivity map (top) for a single PV surface and sky map (bottom) for 2 pm on 30^{th} June

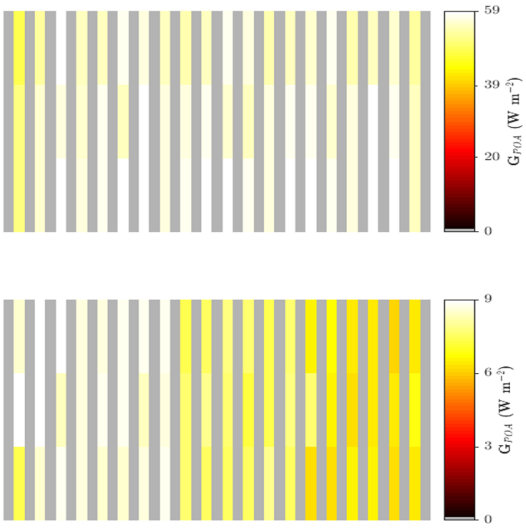

Figure E.7: Irradiance on the front face (top) and rear face (bottom) of the PV curtain at 2 pm on 30^{th} June

E.2. Plane of array irradiance for non-optimal tilt but optimal azimuth at Delft

Figure E.8 shows the irradiance incident on a module at Delft at an optimal azimuth but non optimal tilt of 90 °.

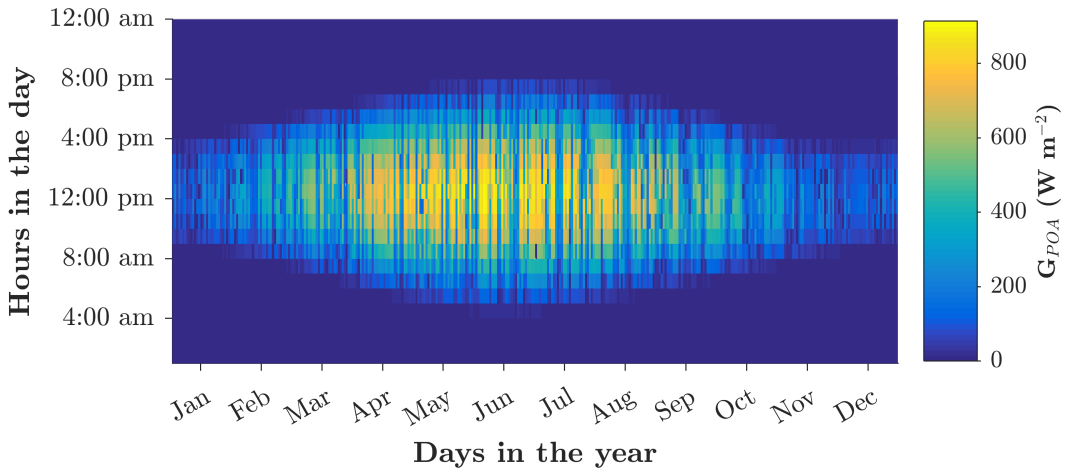

Figure E.8: POA irradiance on a PV module at the optimal azimuth and a tilt of 90 °

E.3. Sensitivity case models

The LightTools models prepared for analysing the sensitivity of the base case to slightly different conditions are shown in this section. Figure E.9 shows the original base case model (with 30 % PV integration), figure E.10 shows a room of half the depth while figures E.11 and E.12 show the models for 15 % and 60 % PV integration respectively

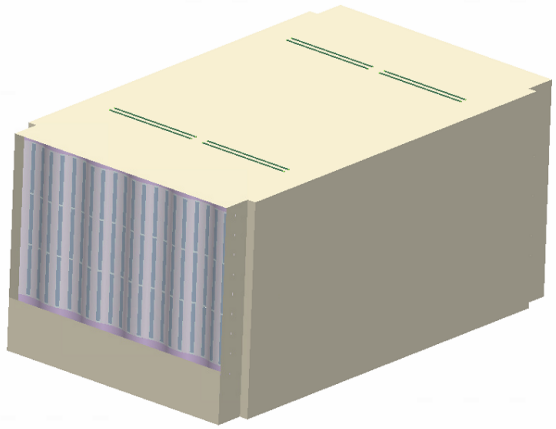

Figure E.9: LightTools model for base case room

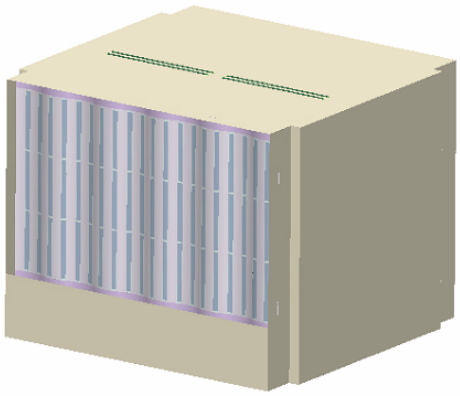

Figure E.10: LightTools model for room of the half depth as base case room

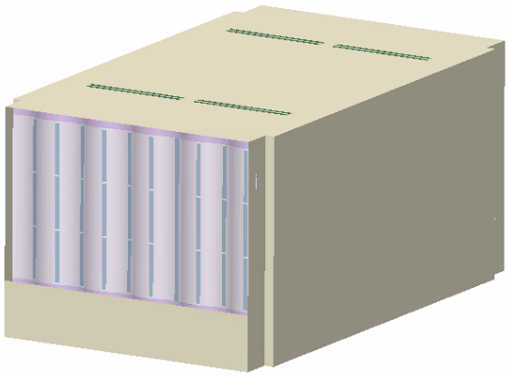

Figure E.11: LightTools model for curtain with 15% PV integrated in the cloth

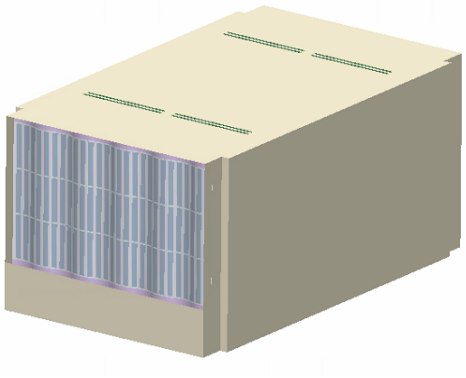

Figure E.12: LightTools model for curtain with 60% PV integrated in the cloth

F

Practical Learnings

Few of the practical learnings achieved in the course of this thesis, are listed below as a guide for anyone wishing to continue this work or pursue research of a similar nature:

- The research started with a choice of optical simulation platform to be considered for analysis of the curtain. Since the backward ray-tracing open software package coded in high level language 'Radiance' is most cited in literature, an approach based on Radiance was started. This involved the use of Rhino 3D along with grasshopper, ladybug and honeybee add-ons. While these are quite extensive with countless online forum discussions, these are best suited for architectural daylighting simulations and most of all for situations where licenses for heavier software like LightTools may not be available. LightTools was eventually chosen because of its ability to even allow for the more accurate but more time consuming forward ray tracing (as well as backward ray tracing) and its validation through previous works at TU Delft and for ease of modelling.
- In its initial stage, an analysis of the bifacial PV curtain using the "effective medium theory" to represent the PV and cloth together was used. This theory involves representing a composite non-homogeneous material by averaging the properties of the constituents that make up the composite. By adjusting the optical properties accordingly, a model of such sorts was prepared, without making any PV strip layout on the curtain. However, this model is only applicable to microscopic quantities and cannot be extrapolated to large scale models like the curtain in question. This led to high errors between the two optical models- one with PV strips and one without but with adjusted optical properties to account for it. Hence, this approach was abandoned.
- During simulation using LightTools, initially a solid curtain (using a sine wave equation) and solid window were modelled in LightTools itself instead of Rhino. Solids transmitting bodies result in much more computational effort due to multiple internal reflections, even for thin solids. This was done because a certain bug in LightTools would not allow imported surfaces to be completely transmitting, even if its material was set to air. This resulted in a computation time of 5 hours for generating results for just a single position of the sun for 10 million rays. The bug was fixed by applying double sided ray trace on the entire model (mainly the transmitting objects).
- Air must be set as the material for all defined geometry so that any any optical properties defined are relative to air and not superimposing on the material assigned which may result in unexpected results.
- During validation by experimentation, an initial trial was run without using a reference cell (since a PERC bifacial cell was not available), but instead measuring the irradiance for every PV strip (12 points front and 6 points on the rear side) using a pyranometer and correcting the readings for STC. The pyranometer readings showed high values around 1500-1600 W/m^2. This was because it is sensitive in a range from 300 nm to 2500 nm, and the solar simulator used gives high amount of radiations in the infrared spectrum. To correct for this, the irradiance measured was converted to a AM1.5 value by running a second experiment comparing the output of a spectrometer and pyranometer at the same point under the LASS. Since the spectrometer only measures in the range of the solar cell, the percent of ir-

radiance in the pyranometer's readings, that lie between 300 nm and 1100 nm was obtained. Factoring this in with NREL equivalents for AM1.5 between 300 nm and 1100 nm and multiplying this with the entire solar spectrum, gave an equivalent irradiance in the AM1,5 wavelength range for all cases. This was used to correct all results to STC. However, high errors led to an abandonment of this approach. The measurements were then repeated with the c-Si monofacial aluminium back surface contacted, reference cell to obtain more realistic readings. Nevertheless, errors would still exist due to an overestimation of power as the reference cell could only be placed on the side of the model so the irradiance it saw was lower than the centre of the model.

- For mini module characterization, facilities at TU Delft such as the LASS and cell measurement unit were both deemed unsuitable since the LASS is meant for full module measurements and has poor accuracy at low voltages, especially when the net power of the setup is below 10 W. For the cell measurement setups, the size of the mini module is too big to allow for measurements. Eternal Sun flash simulators were used for assessing power output. However, due to lack of bifacial PERC reference cell, a second approach entering one of the full cells as a reference cell was attempted, resulting in a deformed IV curve. Although the exact reasons for this are still unknown and being investigated, a second attempt at manually tracing the IV curve of the reference full cell using the flash, also did not give fruitful results due to high internal resistance of cables used for connecting the cell to the measurement equipment. Finally, the neonsee solar simulator at Solliance in Eindhoven was used to obtain most accurate measurements for cell and mini modules.To confirm these, a second set of measurements for the base cell were taken at the bifacial research group of ECN Petten where an actual bifacial c-Si standard reference cell was used for calibration. The nearly 190 mA difference between the measured cell used as reference in Solliance and the cell measured in ECN proved that the measured results recorded in Solliance were fairly accurate.
- A last minute bug was spotted in the LightTools simulation where if the same model is modified for a sensitivity check such as a different optical property than what was assumed in the base case, and the macro is run again, it results in an absorbed irradiance that is half compared to the original result. It must be noted here, that once the macro is run for the first time, the sun source gets circulated all across the sky resulting in an end position for the source that is different from its start position. Although this was manually shifted back to the original position (at the zenith of the room), slight errors in alignment of the source (at 10^{-11} instead of 0) could not be corrected. To solve this bug, any slightly modified model was instead made in a whole new model or the source and receiver were completely deleted and remade before running a new macro.